INVESTIGATION OF TRANSIENT TEMPERATURE OF PHARMACEUTICAL TABLETS DURING COMPACTION WITH INFRARED THERMOGRAPHY AND COMPUTATIONAL MODELING

by

HWA HSIUNG LEE

A dissertation submitted to the

School of Graduate Studies

Rutgers, The State University of New Jersey

In partial fulfillment of the requirements

For the degree of

Doctor of Philosophy

Graduate Program in Chemical and Biochemical Engineering

Written under the direction of

Alberto M. Cuitiño

And approved by

_____

_____

_____

_____

New Brunswick, New Jersey

May, 2019

ABSTRACT OF THE DISSERTATION

Investigation of Transient Temperature of Pharmaceutical Tablets during Compaction with Infrared Thermography and Computational Modeling

By HWA HSIUNG LEE

Dissertation Director:

Alberto M. Cuitiño

Manufacturing of a pharmaceutical tablet from powder is always accompanied by the conversion of irreversible mechanical work of compaction into heat. The heat is generated due to friction between powder particles, particles and the die wall, plastic deformation of particles, bonding, and other irreversible processes. The resulting temperature increase potentially might have significant effects on a tablet's mechanical properties, disintegration time, and drug release.

The purpose of this research is to utilize infrared thermography (IRT) as a non-destructive, non-contact in-line process analytical technology (PAT) tool to measure pharmaceutical powders thermomechanical behavior during tablet compaction process. With instantaneous visual results from infrared measurement and in contrast to just monitoring

tablet's temperature evolution, the tablet's rate of cooling at *regular regime* can be a measurable critical quality attribute (CQA) for pharmaceutical tablet quality control. For this novel approach, results show there is an enormous potential to use infrared (IR) measurement as an in-line PAT tool to discriminate tablets between same formulation but experienced different total process shear of a continuous powder flow stream in continuous pharmaceutical tablet manufacturing operations.

For the first time, a novel correlation model with respect to different total process shear of model granulation is developed toward predicting tablet tensile strength that only needs (i) the tablet's rate of cooling at *regular regime* obtained from IR measurement and (ii) relative density of tablet.

Temperature rise can also affect physiochemical properties of the medicinal substances, including chemical stability, crystallinity and polymorphous state. The temperature increase in the powder during compaction is detrimental to heat sensitive active pharmaceutical ingredients (APIs) with low heat conductivity, such as most organic materials used in pharmaceutical formulations. Therefore, it is important to understand the thermomechanical behavior of powders during compaction.

Infrared thermography (IRT) provides a useful tool to trace the temperature distribution evolution of the tablet surface after ejection from the tablet press in laboratory experiments but also during manufacturing, in particular as in-line PAT tool for quality control. We show that utilizing infrared thermography as a non-destructive and non-contact PAT tool

that allows accurate tablet surface temperature fields acquisition in real time to accuracy of $\pm$ 0.1 °C during tablet compaction.

Heat transfer of particulate systems in pharmaceutical tablet manufacturing is important element to be considered, yet is not fully understood. We utilize computational tools based on particle-mechanics to describe the formation of networks during the consolidation process. These heterogeneous networks are subsequently used to simulate the heat transfer process after ejection. We demonstrate the computational modeling match well with experimental results from infrared measurement, which have not been previously reported.

Acknowledgements

I would like to thank my thesis advisor, Professor Alberto Cuitiño, for his encouragement, mentoring, inspiring and trust. I would especially like to thank Professor Cuitiño for always giving me opportunities to make mistakes, to learn, and to challenge myself. Working toward PhD degree has been a life changing experience for me, and I have been fortunate to have the help and support from many individuals.

I also like to thank my dissertation committee members: Professor German Drazer for his suggestions and inputs; Professor Gerardo Callegari for his help of my tablet compaction experiments and suggestions in project scope; Dr. Bereket Yohannes has been extremely instrumental in computational simulations and also his help and support throughout the research project.

I would like to thank Professor Fernando Muzzio for his support and guidance throughout my PhD studies. Special thanks to Dr. Yuriy Gulak who has provided me with great help in analyzing infrared data and his constant help and support throughout many years at Rutgers. I would like to thank Professor David Lee of Rutgers New Jersey Agricultural Experiment Station for making it possible to use the infrared thermal camera for my studies. I am thankful for all their help and support from Carmen Elsabee, Shefali Patel, Cynthia Cartegna and John Petrowski from Mechanical and Aerospace Engineering.

It has been my privilege to be able to work with so many talented colleagues, who have made the course of my PhD studies filled with enjoyment and friendship. The interactions

with industrial and academic collaborators have been invaluable and insightful. It also helped me to have a better understand and address industry needs for my dissertation.

I thank God for my family in supporting me all the way: my wife, Dr. Yokechen Chang-Lee, my daughter, Dr. Esther EnShin Lee, and my son, Samuel EnYih Lee, without their steadfast love and support it won't be possible for me to finish my PhD studies.

Thank God for giving me my loving parents: my father ChungHsing Lee and my mother JingYuan Lee-Liu for their unwavering love and caring throughout my life; and my elder sisters and brothers: JongMiao Lee, DiMiao Lee, ChaoHsiung Lee, WanMiao Lee, TsengMiao Lee, LiehHsiung Lee, ChingHsiung Lee, JingMiao Lee, WeiHsiung Lee, and ChungHsiung Lee for their encouragement and financial support for me to come to the United States of America for my graduate studies at Rutgers University in New Brunswick, New Jersey. They have given their endless love and support for me.

Dedication

I dedicate this thesis to:

My loving parents:

My father ChungHsing Lee, 李仲信, and my mother JingYuan Lee-Liu, 李劉錦媚

And

My wife Dr. Yokechen Chang-Lee, my daughter Dr. Esther EnShin Lee, and my son Samuel EnYih Lee

Nothing would be possible without their unchanging love and support in God.

Table of Contents

List of Tables

List of Figures

Chapter 1

Introduction

About 80% of all pharmaceutical products for US consumption are in solid dosage forms [1]. Solid dosage manufacturing involves a range of processing technologies to take formulated API through to finished dose forms such as tablet and capsule. A thorough understanding of both the product and the process technology are required for optimization.

As Quality by Design (QbD) is gaining more awareness in pharmaceutical industry in both R&D and manufacturing process. The objectives of pharmaceutical quality by design include the following:

(1) a quality target product profile (QTPP) that identifies the critical quality attributes (CQAs) of the drug product;

(2) product design and understanding including identification of critical material attributes (CMAs);

(3) process design and understanding including identification of critical process parameters (CPPs), linking CMAs and CPPs to CQAs;

(4) a control strategy that includes specifications for the drug substance(s), excipient(s), and drug product as well as controls for each step of the manufacturing process; and

(5) process capability and continual improvement.

And QbD tools and studies include prior knowledge, risk assessment, mechanistic models, design of experiments (DoE) and data analysis, and process analytical technology (PAT) [2].

Process analytical technology (PAT) is an enabling technology for QbD initiative by the Food and Drug Administration that requires a scientific, risk-based, and proactive approach to pharmaceutical development. Critical quality attributes (CQAs) are defined as physical, chemical, biological properties or characteristics that must be controlled directly or indirectly to ensure the quality of the product. PAT tools enable in-line measurement of critical quality attributes (CQAs) and process parameters in real-time, allowing running processes to be adjusted on the fly. Product quality is verified in multiple steps during process execution rather than performing QC at the end of the line, helping to shorten batch release times.

Manufacturing of a pharmaceutical tablet from powder is always accompanied by the conversion of irreversible mechanical work of compaction into heat. The heat is generated due to friction between powder particles, particles and the die wall, plastic deformation of particles, bonding, and other irreversible processes [3]. The resulting temperature increase potentially might have significant effects on a tablet's mechanical properties, disintegration time, and drug release [4, 5]. Temperature increase during compaction of pharmaceutical powders has been of interest to pharmaceutical scientists. Studies such as using thermocouples imbedded in the compressed tablet to measure the temperature changes [6-9], utilizing infrared thermal camera to monitor tablet surface temperature [3, 10-12], and finite element analysis for modeling temperature and density distribution within the pharmaceutical tablet [3, 13, 14]. Influence of temperature on mechanical properties of tablet has been investigated by some studies [15, 16]. The surface characteristics changes

during sheared mixing of heterogeneous systems can affect powder and tablet properties [17, 18].

Temperature rise also affects physiochemical properties of the medicinal substances, including chemical stability, crystallinity and polymorphous state [19]. The temperature increase in the powder during compaction is detrimental to heat sensitive APIs with low heat conductivity, such as most organic materials used in pharmaceutical formulations. Therefore, it is important to understand the thermomechanical behavior of powders during compaction.

Among several techniques of tablet temperature measurement directly after tablet's ejection from tablet press, infrared thermography has the unique advantages [3, 10] to be utilized as a potential in-line PAT tool for quality control. This technique, being non-destructive [20] and non-contact, allows accurate tablet's surface temperature fields acquisition in real time. The primary source of infrared radiation is heat. Infrared camera can capture heat signature of pharmaceutical tablets and convert the information for further data analysis.

Heat transfer of particulate systems in pharmaceutical tablet manufacturing is important element to be considered yet is not fully understood. We utilize computational tools based on particle-mechanics to describe the formation of networks during the consolidation process. These heterogeneous networks are subsequently used to simulate the heat transfer

process after ejection. We demonstrate the computational modeling match well with experimental results from infrared measurement, which have not been previously reported.

Chapter 2

Background and Significance

2.1 Introduction

The knowledge of compaction induced thermal energy is needed for a better understanding of the mechanism involved in the bond formation of pharmaceutical solid dosage forms.

Infrared thermography (IRT) is a unique technique that allows instantaneous real-time temperature measurements without physical contact with the heat emitting object. With its non-contact and non-destructive advantages, infrared (IR) measurement has a great potential to be utilized as an in-line PAT tool to monitor the pharmaceutical tablet manufacturing operations.

Some of the main areas where infrared thermography is being used successfully in medical field are neurology, vascular disorders, rheumatic diseases, tissue viability, oncology (especially breast cancer), dermatological disorders, neonatal, ophthalmology, and surgery [21-28] and veterinary [29-34] as diagnostic tool, as it provides accurate readings without invasive procedures. The advantage that infrared thermal imaging as a non-contact technique is very important in this field, because this means that it is a non-invasive procedure. Moreover, as the instrument is non-contact, it does not affect the result of the measurement and can be carried out remotely. Body temperature is a very good indicator of health condition, as changes of a few degrees on skin temperature can be used as an indicator of possible bodily dysfunction.

Medical applications can use infrared thermal imaging as an alternative diagnostic tool. For example, it is used to detect superficial body tumors, such as breast cancer [35-39]. Tumors generally have an increased blood supply that increases the skin temperature over them. Therefore, infrared thermal imaging can be used as an effective early indicator of breast cancer, which results in a much higher chance of survival [40, 41]. Infrared thermal imaging in this application is a diagnostic tool with high efficiency that enables the medical professional in the detection of early warning signals. Early detection is the main advantage of infrared thermal imaging compared with other methods in medical applications. Infrared thermal imaging is also used in many other medical applications, such as the diagnosing of vascular disorders, imaging during heart surgery, fever screening, and dermatology [42-45].

The infrared thermal imaging technique is also used in electrical, mechanical and insulation industry. Such as it is used in electrical and mechanical maintenance to detect early signs of malfunction, so costly breakdowns can be avoided [46]. In the electrical power system, abnormal temperature patterns can indicate faulty connections [47, 48]. Infrared thermal imaging can measure the heat signature to indicate excessive friction due to material fatigue or improper lubrication of mechanical parts [49, 50]. For insulation industry, it is used to detect hidden losses of heat that can drain performance and increase costs [51-53]. In construction industry, non-invasive infrared technique can detect anomalies for early detection and prediction of possible faults, or to check the quality of the object [52, 54-58]. Infrared is also utilized in other areas, such as evaluation of fatigue damage in materials and monitoring of plastic deformations [59, 60].

Building inspection is another area where infrared thermal imaging is successfully applied. Temperature distribution on the face of a building provides very useful information to discover many hidden conditions related to the building performance and maintenance. It can be used to detect where and how the heat or air conditioning is leaking from a building envelope [61-64]. In addition to the detection of heat loss, it also can discover other anomalies, such as water infiltration and moisture. Wet mass inside a wall has a differentiated thermal inertia that can be discovered using infrared thermal imaging for sub-surface moisture detection and moisture mapping in ancient buildings [65].

The problem of moisture accumulation in airplane honeycomb panels is a serious issue for flight safety. Moisture detection using infrared technique can also be applied to aircraft structures, the presence of water inside aircraft structures may lead to ice formation with a volume variation and consequent mechanical stresses [66-69].

This non-invasive infrared temperature measuring technique is also used in agriculture industry [70, 71], pharmaceutical industry [3, 10-12]. Defense and space industry also use high resolution infrared imaging system for precision guided missiles [72, 73] and scientific discovery of the state-of-the-art James Webb Space Telescope [74].

Two different approaches are employed in infrared thermography: passive and active [75]. For passive infrared thermography, the infrared radiation coming from the sample object is measured without any external heat stimulation. On the other hand, in active infrared

thermography [76, 77], the sample is subjected to external thermal stimulation. The active infrared thermography is measuring the infrared radiation comes from the thermal response of the sample to the external thermal excitation. The thermal response depends on both the thermal properties and the subsurface anomalies of the material, which will result in temperature differences on the surface of the sample.

Passive infrared thermography is used in quality control and process monitoring applications. Active infrared thermography is applied for inspection of surface and sub-surface defects in materials, where an external stimulus is applied to the sample object in order to induce relevant thermal contrasts between regions of interest.

Infrared (IR) detectors are categorized as either thermal detectors or photon detectors [35, 78] as shown in Figure 2.1 (a). Thermal detectors (e.g., a microbolometer) rely on changes in electrical resistivity upon incident infrared radiation due to heat emitted from the sample object; they are uncooled and typically made of vanadium oxide or amorphous silicon. An example of cross-sectional view of a microbolometer is shown in Figure 2.1(b). Photon detectors are photoconductive or photovoltaic in nature; they require cryogenic cooling and are made of a semiconductor compound (e.g., InGaAs, InSb, or HgCdTe, depending on IR spectral band). The IR spectrum ranges in wavelengths between approximately 0.78~1000 μm, and usable spectrum can be categorized into four spectral bands: Near-infrared (NIR, 0.8~1.7 μm), short-wave infrared (SWIR, 1~2.5 μm), mid-wave infrared (MWIR, 2~5 μm), and long-wave infrared (LWIR, 8~14 μm). Thermal detectors are limited to LWIR, while

photon detector materials can be selected and fine-tuned for SWIR, MWIR, or LWIR detection.

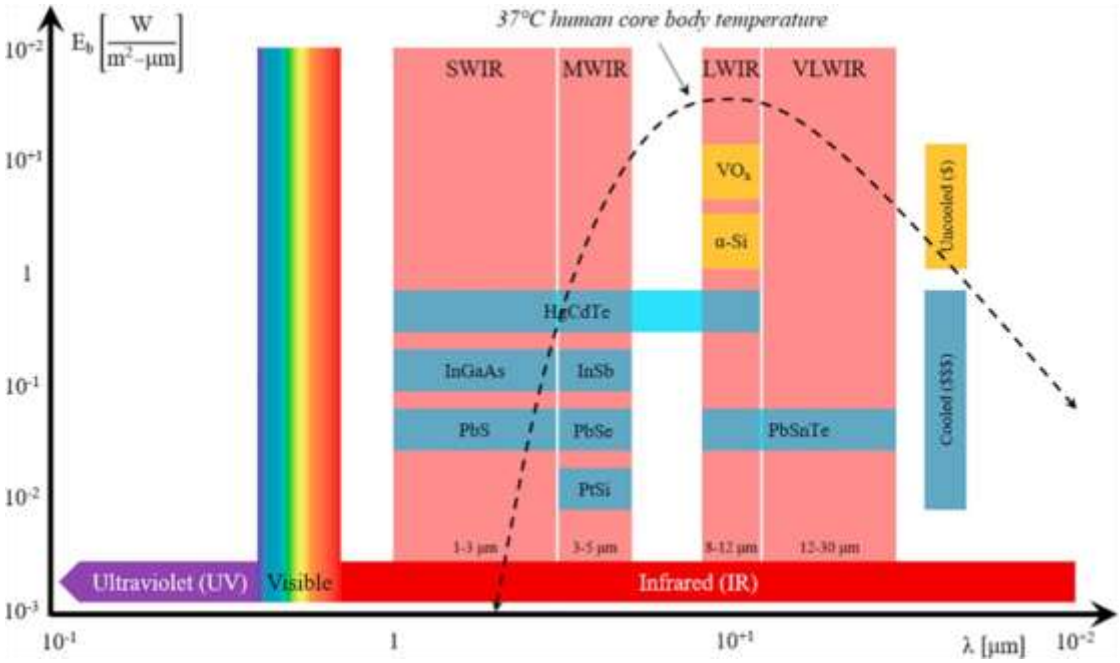

Figure 2.1 (a): Typical infrared (IR) detector materials used across IR spectral bands, adopted from Lozano et al. [2019]

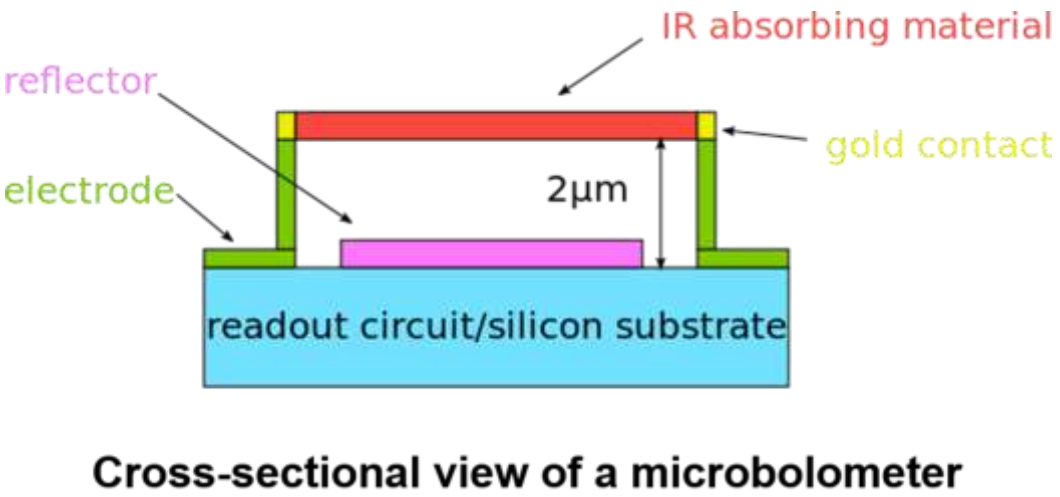

Figure 2.1 (b): Cross-sectional view of a microbolometer. (Vanadium Oxide detector) Adopted from https://en.wikipedia.org/wiki/Microbolometer and ICI 7320 Operation Manual

2.2 Literature Review

2.2.1 Tablet Temperature Measurement During Compaction

Pharmaceutical tablet temperature changes during compaction is an important subject but only a handful of studies conducted on the measurement of tablet temperature changes during tablet compaction in the past 40 to 50 years. Thermocouples was introduced in early 1970s and infrared thermal camera has been utilized starting in 1990s.

2.2.1.1 Temperature Measurement Using Thermocouples

Travers and Merriman started from using thermocouples imbedded in compressed tablet in 1970 [6] to measure the temperature rise during compression of acetyl-salicylic acid, sodium chloride, and boric acid.

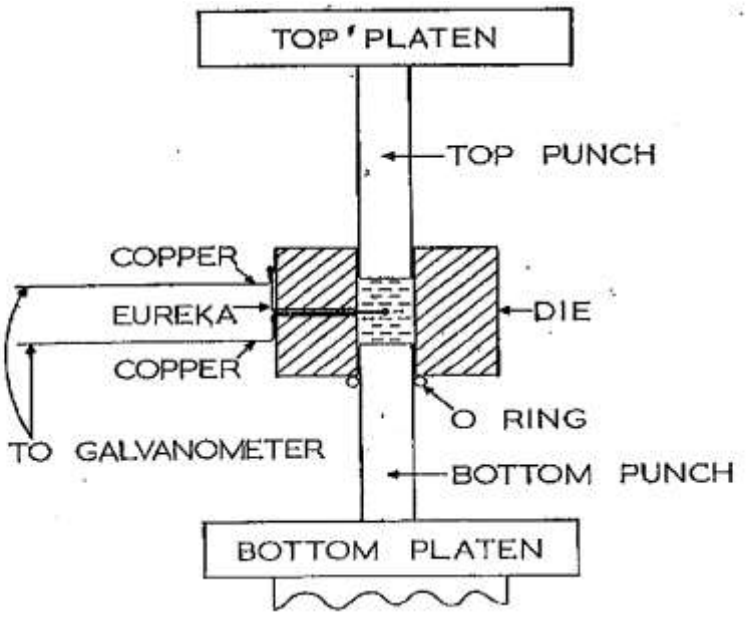

Figure 2.2: The punch, die, and thermocouple assembly, adopted from Travers and Merriman [1970].

Wurster and Creekmore [7] in 1986 and Wurster et al. [8] and Rowlings et al. [9] in 1995 used tungsten wire temperature sensor as a probe in die to determine the temperature rise in pharmaceutical powders. Temperature rise of microcrystalline cellulose (MCC Avicel PH 101), anhydrous lactose, and Starch 1500 were measured during compaction. They reported, for Avicel PH 101, it was observed that the temperature rose 5.1 °C; for anhydrous lactose, it was 3.04 °C and for Starch 1500 was about 2.13 °C.

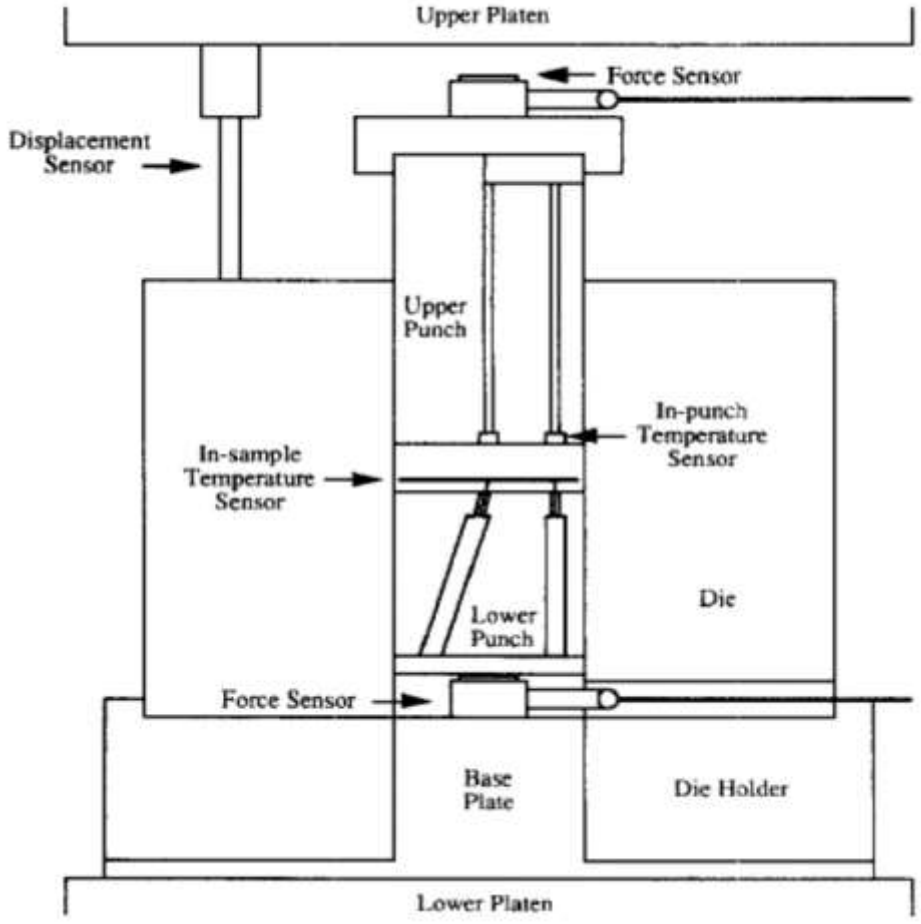

Figure 2.3: Cross-sectional view of the punches, die, and in-sample temperature sensor assembly, adopted from Wurster et al. [1995]

2.2.1.2 Temperature Measurement Using Infrared Thermal Camera

Principles of Infrared Thermography

Any object with temperature greater than absolute zero (i.e., T > -273.15 °C or 0 °K), radiates in the infrared from its surface. Even ice emits infrared radiation. The surface temperature of an object can be derived from the infrared radiation. Human eye can't see this type of radiation, so infrared thermal camera is required to acquire and process this information.

Infrared radiation is the energy radiated by the surface of an object whose temperature is above absolute zero. The radiation leaving the object is the sum of emission (ε_λ), reflection (ρ_λ), and transmission (τ_λ) [79]:

$$\varepsilon_\lambda + \rho_\lambda + \tau_\lambda = 1$$

Electromagnetic spectrum is divided into several regions or bands according to the wavelength. Infrared region is approximately defined from 0.78 μm to 1000 μm, which is from the end of visible light to microwaves as shown in Figure 2.4. The emitted radiation is a function of the temperature of the material; the higher the temperature, the greater the intensity of the infrared energy emitted [20] as shown in Figure 2.5. Much of the infrared range of the electromagnetic spectrum is not usable in infrared thermography (IRT), because it is blocked by the atmosphere.

The usable part of the infrared thermography is listed as follows:

- Near-infrared (NIR) from 0.8 μm to 1.7 μm.
- Short-wavelength infrared (SWIR) from 1 μm to 2.5 μm.
- Mid-wavelength infrared (MWIR) from 2 μm to 5 μm.
- Long-wavelength infrared (LWIR) from 8 μm to 14 μm.

Of all these regions, MWIR and LWIR are the most commonly used in IRT. There are two reasons due to the band of peak emissions and atmospheric transmittance:

The first is due to the relation between temperature and wavelength. So, the most effective measurement for a particular temperature should be carried out for the wavelength at which most intensity is emitted. The second is related to the atmospheric transmittance. Infrared radiation travels through air, being absorbed by various air particles, mostly by CO_2 and H_2O. The degree to which air absorbs infrared radiation depends on the wavelength. In the MWIR and LWIR bands, this absorption is low, which allows more infrared radiation to reach the sensor in the thermal camera.

Figure 2.6 shows the atmospheric transmittance for different wavelengths. As it can be seen, in the visible part of the spectrum, from 0.4 μm to 0.7 μm, only 60% of the emitted radiation is transmitted. Almost no radiation is transmitted between 5 μm and 7.5 μm, since the atmosphere absorbs all of this radiation. Therefore, infrared measuring devices use either MWIR or LWIR. MWIR devices are used for high-temperature readings, while LWIR is used for ambient temperature measurements.

Infrared thermal cameras acquire infrared radiation emitted by an object and transform it into electronic signal. The difference between a visible image and an infrared image is that the visible image is a representation of the reflected light on the object, whereas in the infrared image, the object is the source that emits its surface temperature through infrared radiation and can be measured by an infrared camera without light. Images acquired using infrared cameras are converted into visible images by assigning a color to each infrared energy level. The result is a false-color image called a thermogram.[20]

The main advantages of infrared thermography (IRT) are the following [80]:

- IRT is a non-contact technique: the thermal cameras used are not in contact with the source of heat, i.e., they are non-contact temperature probes. The temperature of extremely hot objects or dangerous products, such as processing of sulfuric acid, can be measured safely and keep the user out of danger.
- IRT provides two-dimensional thermal images, which make a comparison between areas of the target possible.
- IRT is in real time, which enables not only high-speed scanning of stationary targets, but also acquisition from fast-moving targets and from fast-changing thermal patterns.
- IRT has none of the harmful radiation effects of technologies, such as X-ray imaging. Thus, it is suitable for prolonged and repeated use.
- IRT is a non-invasive technique. So, it does not intrude upon or affect the target object.

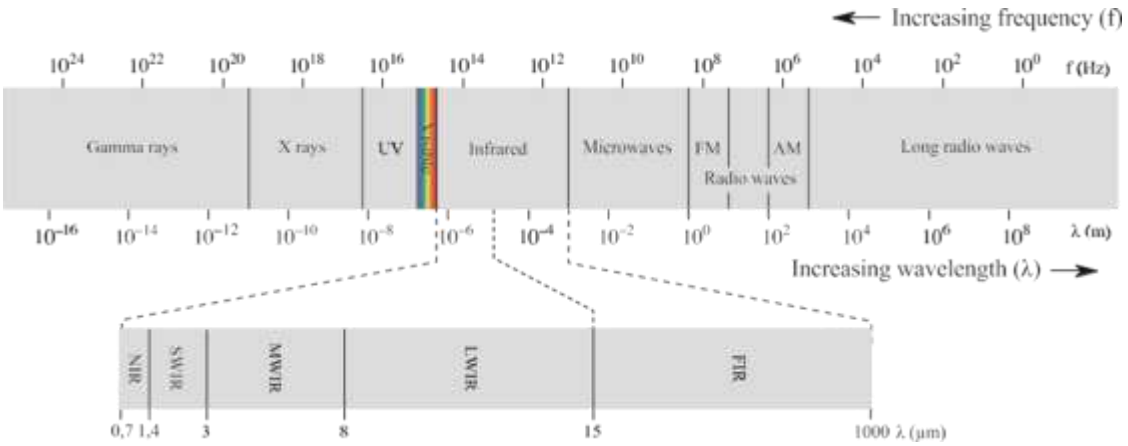

Figure 2.4: Electromagnetic spectrum with sub-divided infrared spectrum, adopted from Gade et al. [2014]

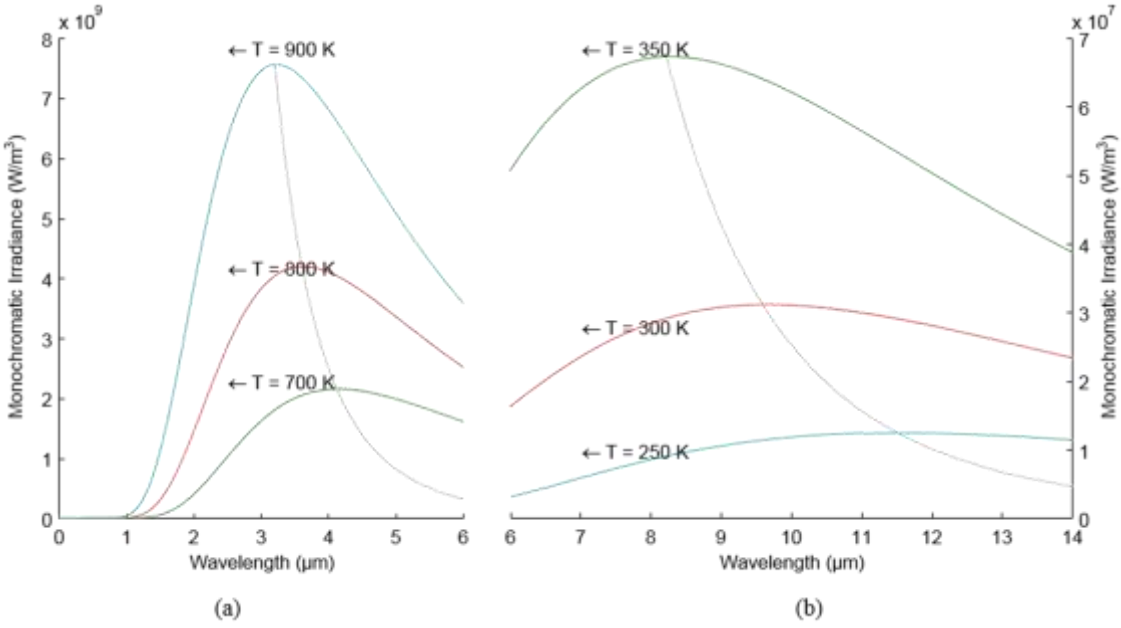

Figure 2.5: Electromagnetic radiation emitted by a blackbody in thermal equilibrium at a definite temperature. (a) Objects with a high temperature emit most of the radiation in the middle wave infrared (MWIR); (b) Objects with a low temperature emit most of the radiation in the long wave infrared (LWIR). Adopted from Usamentiaga et al. [2014]

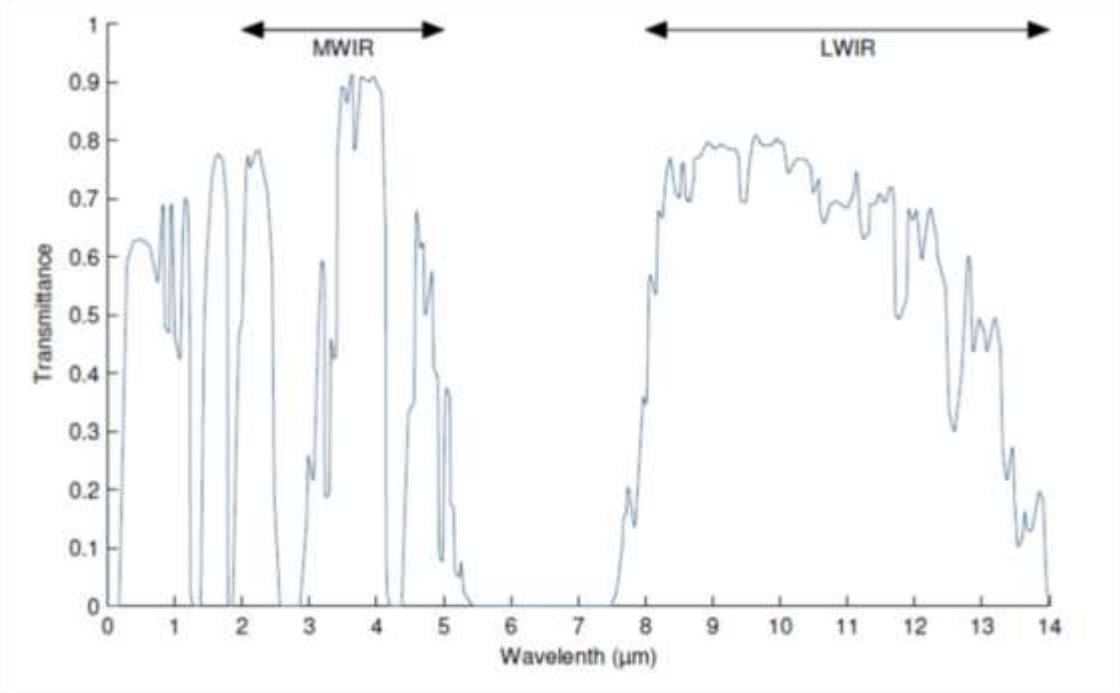

Figure 2.6: Atmospheric transmittance at one nautical mile, 15.5 °C, 70% relative humidity and at sea level, adopted from Usamentiaga et al. [2014]

Research on Temperature Measurement Using Infrared Thermography

Bechard and Down were the first group in utilizing infrared thermal camera to monitor pharmaceutical tablet surface temperature in 1992 [10]. They reported compaction-induced thermal energy released during compaction captured by infrared thermal imaging as semi-quantitative evaluation of a binary mixture of microcrystalline cellulose (MCC, Avicel PH102) and spray-dried lactose (35/65) powder blend compressed at various compaction pressure. They reported tablets lubricated with 1% magnesium stearate had surface temperature of 39~40 °C after a 20-min run time, as opposed to 50~51 °C of tablets lubricated with 0.5% magnesium stearate. Tablet cross-sectional thermal profile revealed a 3~4 °C temperature gradient across the tablet.

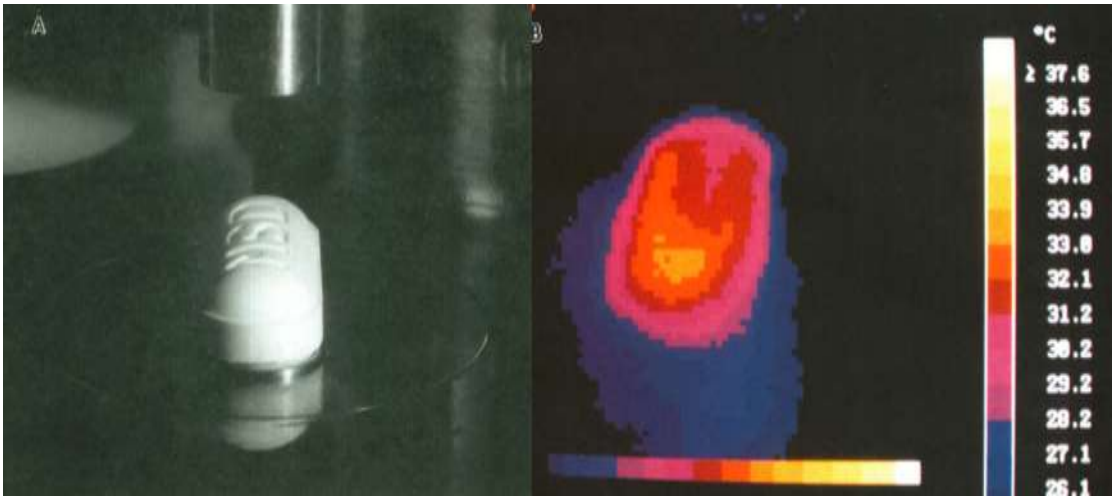

Figure 2.7 (a): (A) Photograph of the actual tablet after ejection, (B) Infrared image of tablet after ejection, adopted from Bechard and Down [1992].

Ketolainen et al. in 1993 [11] observed the rise in temperature during tablet compression using an infrared thermal camera together with an instrumented eccentric tablet press. They evaluated the tablet compression process, temperatures measured from surfaces of recently ejected tablets were used together with energy parameters. They compressed two direct compression excipients, plastically deforming microcrystalline cellulose (MCC) and fragmenting dicalcium phosphate dihydrate. With the differences in specific heat values, the temperature rise of the tablets was higher with microcrystalline cellulose than with dicalcium phosphate dihydrate. They reported more non-homogeneous particle shape and plastic deformation instead of fragmentation may have led to higher temperature of microcrystalline cellulose tablet. For both test materials, the temperature of the tablets rose with the compression force increased whereas lubrication diminished. Due to the non-homogeneous densification the highest temperature values were obtained at the center of the upper surfaces of the tablets. They stated that the mechanical energy was very extensively converted to thermal energy, from the energy parameter values, derived either from force and displacement data (mechanical energy), or from specific heat, temperature increase and tablet weight values (thermal energy). They found that the infrared thermal camera was a very useful tool to be an accurate and informative method for evaluating changes in the temperature, energy content, and characterizing the conversion of mechanical energy to thermal energy during the dynamic tablet compression process.

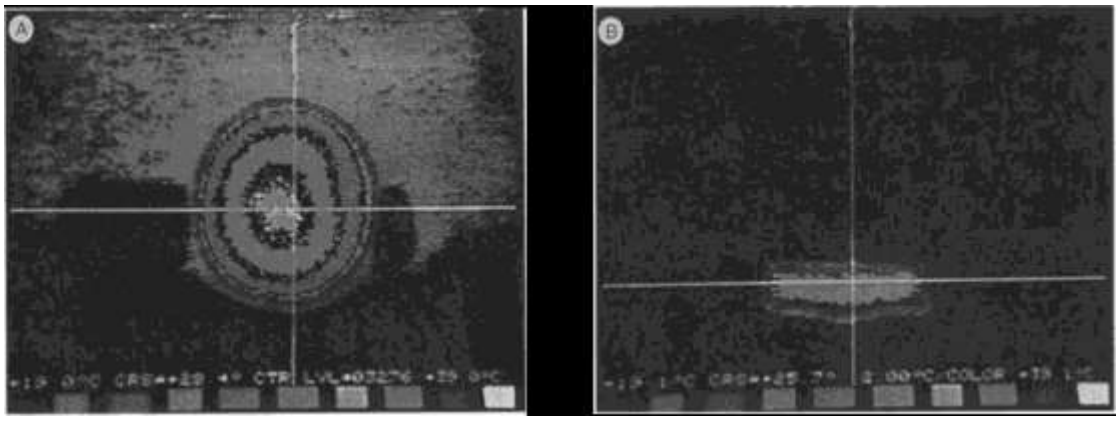

Figure 2.7 (b): Thermograms of upper (A) and side (B) surfaces of lubricated Avicel PH 102 tablets compressed at 20 kN. Temperature scale is from 19 to 39°C. Adopted from Ketolainen et al. [1993].

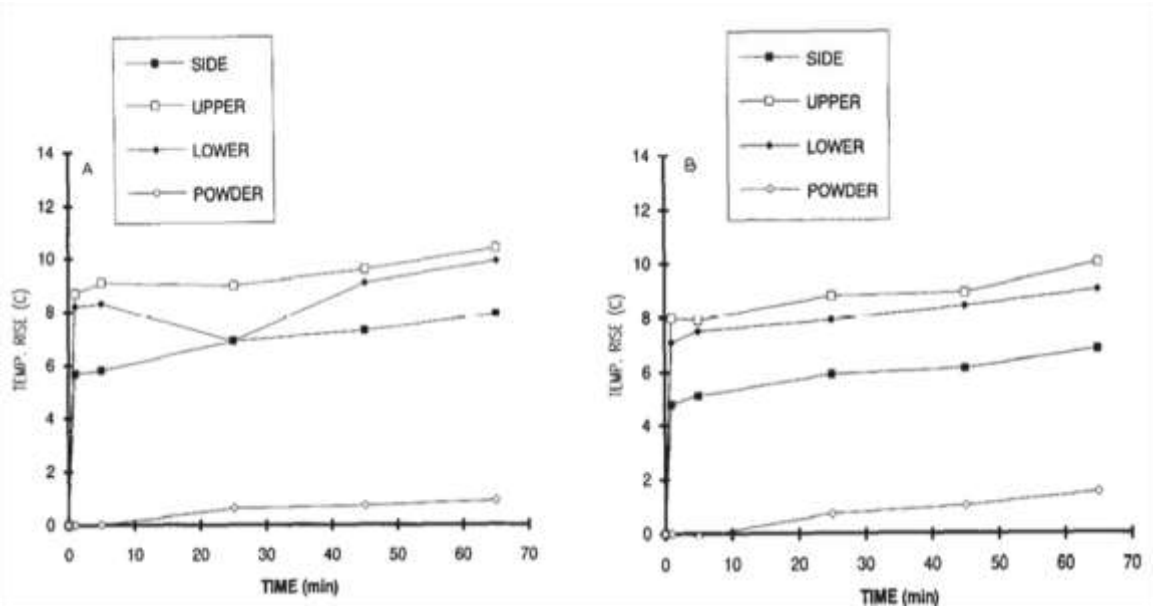

Figure 2.7 (c): Temperature rise (°C) of lubricant-free (A) and lubricated (B) Avicel PH 102 tablets compressed at 20 kN and powder in the hopper as a function of the run of tablet compression (min). Adopted from Ketolainen et al. [1993].

The study by Zavaliangos et al. [3] in 2008 presented a numerical approach to the prediction of temperature evolution in tablet compaction coupled thermomechanical finite element analysis and a calibrated Drucker–Prager Cap model. They used infrared camera for temperature measurement of microcrystalline cellulose (MCC, PH 102) tablet after tablet ejected on die table of tablet press to validate their model prediction of tablet temperature.

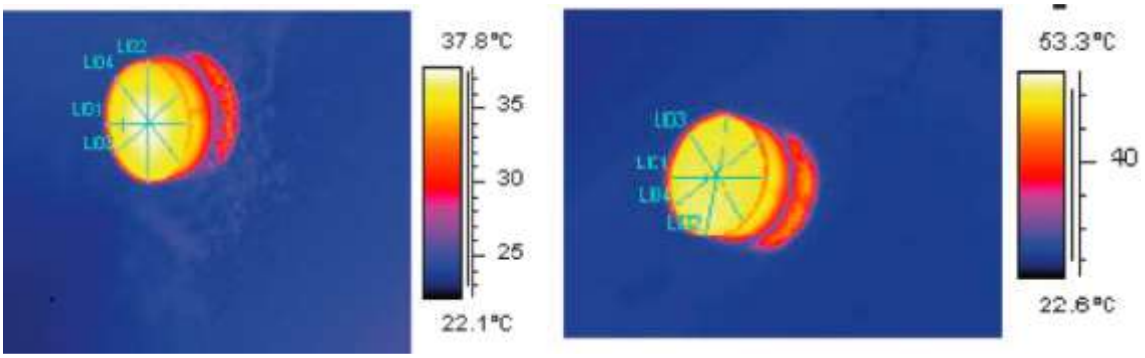

Figure 2.8: Infrared thermal image of two microcrystalline cellulose (MCC, Avicel PH 102) tablets after ejection, adopted from Zavaliangos et al. [2008].

Klinzing et al. [13] in 2010 utilized thermomechanical finite element analysis (FEA) to analyze the full three-dimensional nature of density and temperature distributions within a capsule shaped pharmaceutical tablet. The results of their analysis were validated against X-ray microcomputed tomography (X-ray $\boldsymbol{\mu}$CT) density measurements and infrared (IR) thermal camera measurements of tablet surface temperatures upon tablet ejection from the die. Figure 2.9 showed the IR image of the tablet with three separate lines. Line 1, L1, indicated the temperature gradient from the outer edge of the tablet to the center, Line 2, L2, was from the center of the tablet to the top side edge, and Line 3, L3, proceeded from the top edge of the tablet to the bottom of the tablet.

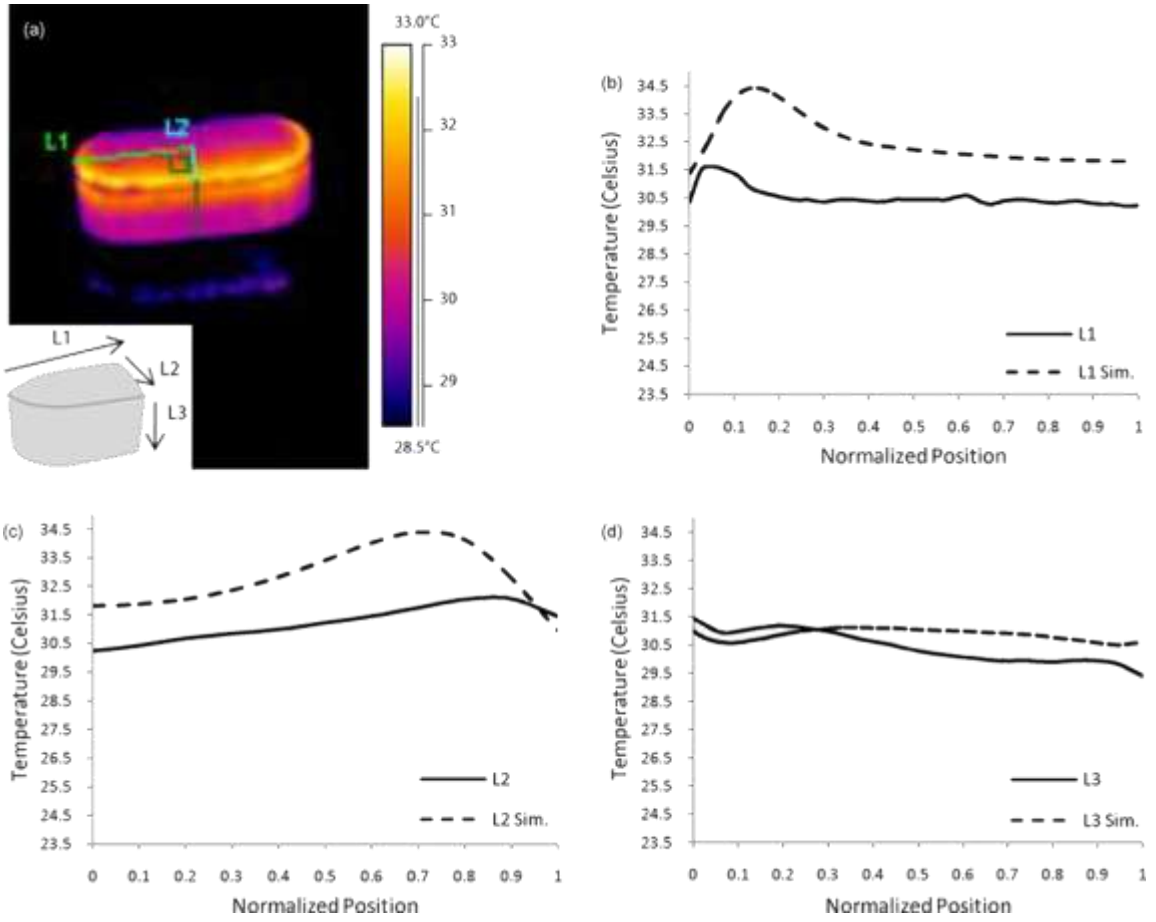

Figure 2.9: Temperature results: (a) IR snapshot of tablet immediately upon ejection, inlay represents one quarter of the tablet with direction of IR lines analyzed, (b) L1 IR and simulation, (c) L2 IR and simulation, and (d) L3 IR and simulation, adopted from Klinzing et al. [2010]

Omar et al. [81] reported in 2015 of the effect of morphology and amorphous content, of three types of lactose: anhydrous SuperTab21AN, *a*-lactose monohydrate 200 M, and spray dried lactose SuperTab11SD on the properties of ribbon produced using roller compaction. They used thermal imaging technique to monitor the surface temperature of the ribbon during roller compaction.

The agglomerated types of lactose produced ribbon with higher surface temperature and tensile strength, larger fragment size, lower porosity and lesser fines percentages than the non-agglomerated type of lactose. The lactose powder with the highest amorphous content showed to result in a better binding ability between the primary particles. This type of lactose produced ribbons with the highest temperature and tensile strength, and the lowest porosity and amount of fines in the product.

They observed that there is a relationship between ribbon's surface temperature and the tensile strength of the ribbon during roller compaction process; the higher the ribbon's temperature during roller compaction the higher the tensile strength of the ribbon.

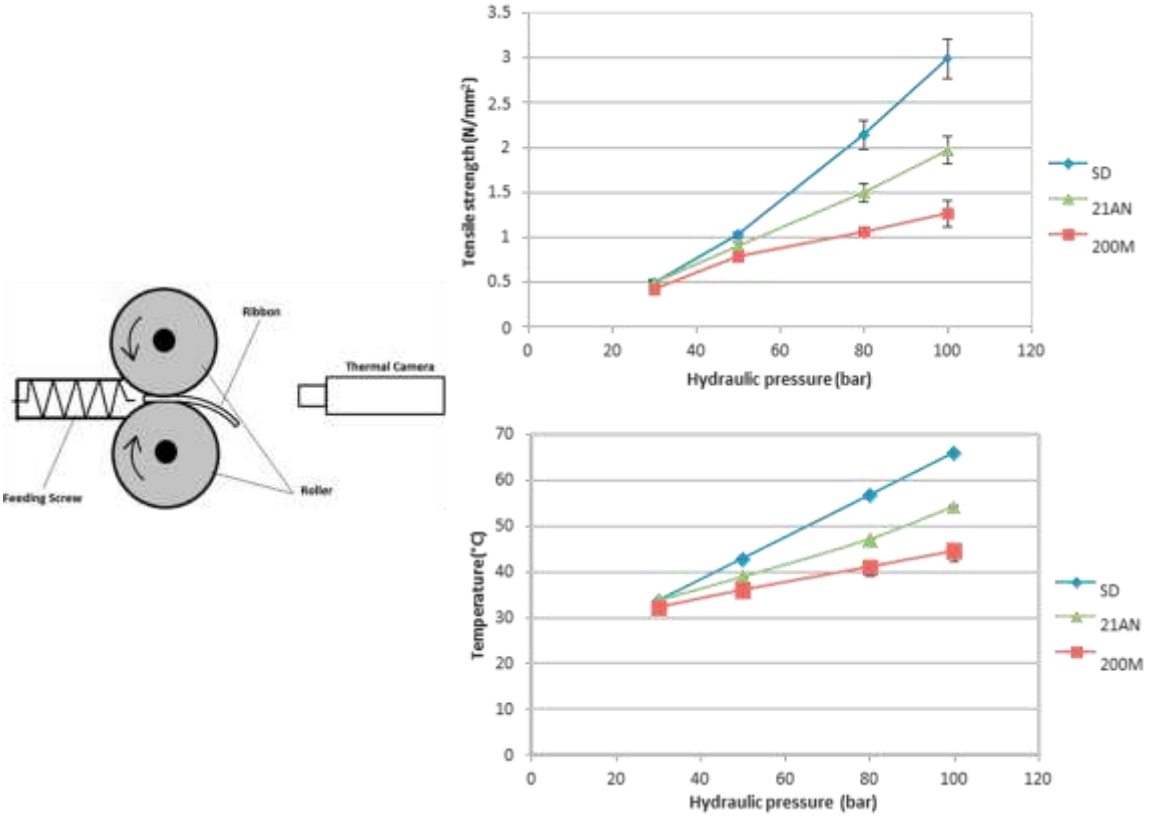

Figure 2.10: Tensile strength of ribbons produced from different types of lactose and surface temperature of ribbons at different hydraulic pressures. Adopted from Omar et el. [2015]

In recent study in 2016 by Krok et al. [12] considered compaction of three grades of microcrystalline cellulose: MCC Avicel PH 101, MCC Avicel PH 102, and MCC DG. Tablets were produced and temperature distributions on the surface of these tablets after ejection were measured using infrared thermal camera. They reported that an increase in the compaction speed led to an increase in the average surface temperature as shown in Figure 2.11.

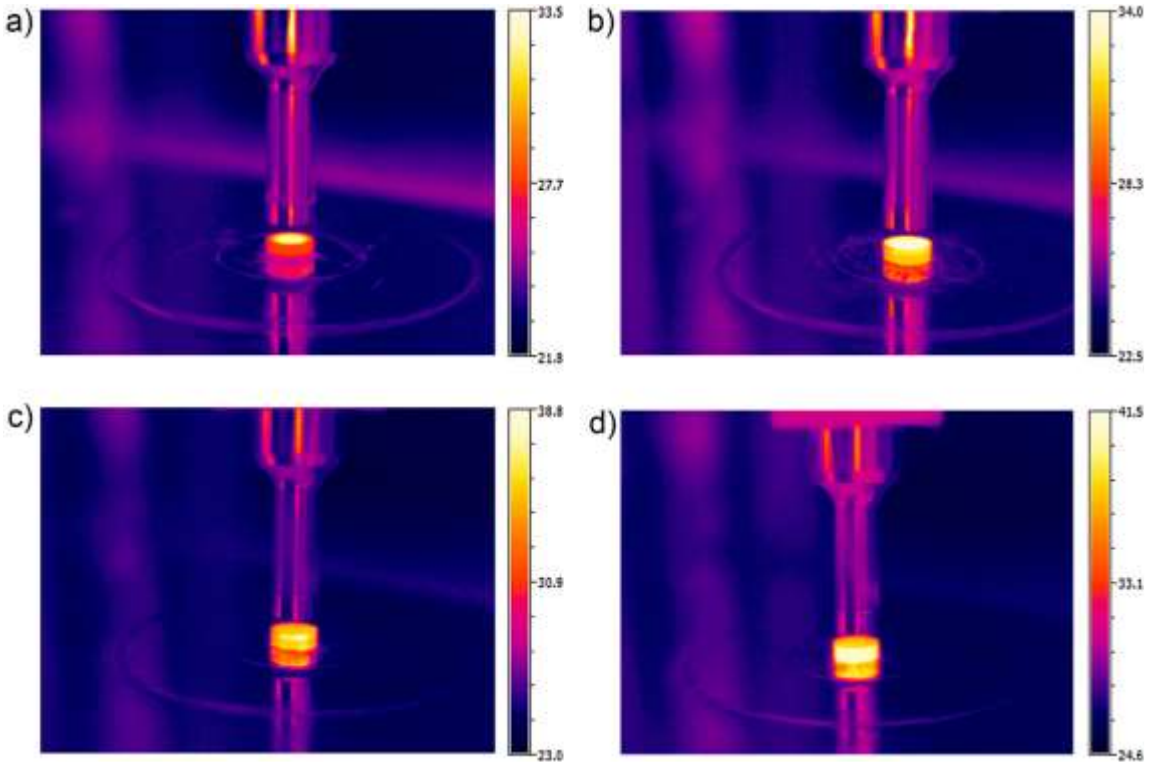

Figure 2.11: The temperature distributions (measured using the IR camera) on the surfaces of the flat-face (FF) tablets made of MCC Avicel PH 102 at various compression speeds: a) 10 mm/s; b) 100 mm/s; c) 300 mm/s; d) 500 mm/s, adopted from Krok et al. [2016].

Freeze-drying is an excellent method of drying thermally sensitive materials and preserving thermally labile compounds. Infrared (IR) thermography is considered a non-invasive technique that can also be applied in the freeze-drying process [82, 83] to evaluate heat transfer and obtain temperature histories over the whole surface of the material that is being processed.

A study by Goncalves et al. [83] in 2017 reported using infrared thermal camera to evaluate the heat transfer processes during the freeze-drying of gelatin model solutions (GMS) with ethanol and carrier agents, and to understand the relation of the temperature profiles with gel thermorheological behaviors and microstructural properties of the freeze-dried systems as shown in Figure 2.12.

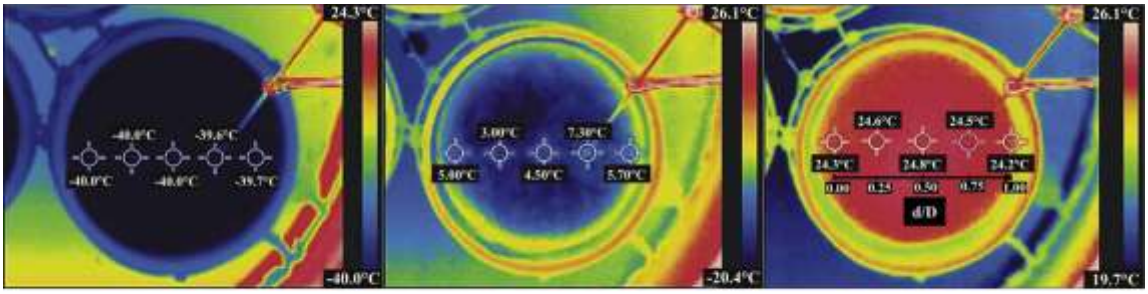

Figure 2.12: Infrared thermograms of the solution model (gelatin with ethanol) at: a) 0 hr.; b) 24 hrs.; and c) 48 hrs. during freeze drying process and dimensionless scale - d/D from 0 to 1, adopted from Goncalves et al. [2017].

The studies in 2017 and 2018 by Wiedey and Kleinebudde [84, 85] utilized infrared thermal camera to record temperature distributions of freshly produced roller compacted ribbons as they left the roll gap of roller compactor during dry granulation process. They presented infrared thermographic images of temperature distributions within the ribbon that could be matched with density distributions measured off-line by X-ray micro-computed tomography (X-ray$\boldsymbol{\mu}$CT). Microcrystalline cellulose (MCC PH 102) was roller compacted on a Gerteis Minipactor with smooth rolls. They reported experiment conducted with cheek plates installed with smooth rolls: the temperature of 33.9 °C in center of the ribbon and below 27 °C near the edges of ribbon from infrared thermal camera in-line measurement; the relative density of 0.84 in the center of ribbon and below 0.60 near edges of ribbon from off-line X-ray$\boldsymbol{\mu}$CT measurement as shown in Figure 2.13.

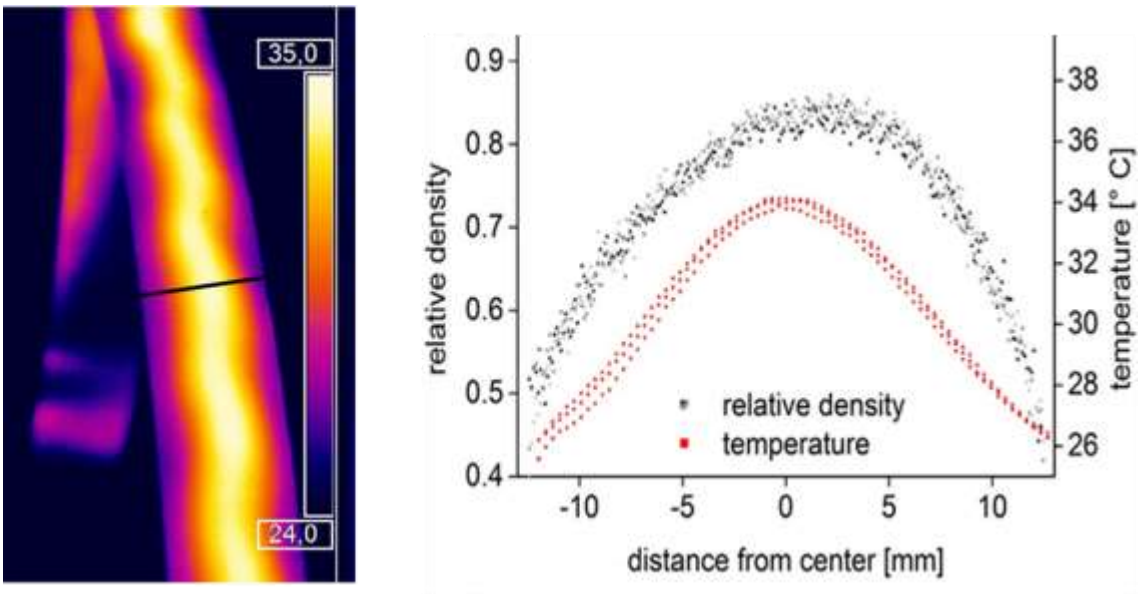

Figure 2.13: Infrared thermographic images of temperature distributions within the roller compacted ribbon of microcrystalline cellulose (MCC PH 102) and density distributions measured off-line by X-ray micro-computed tomography (X-ray$\boldsymbol{\mu}$CT) adopted from Wiedey and Kleinebudde [2017].

These handful of studies utilized infrared thermal camera were reported merely only on compaction-induced temperature rise or verification of their temperature prediction model.

In our study here, we are not only capturing tablet infrared thermal imaging but also going further beyond these infrared temperature histories to analyze the heat transfer and detail temperature evolution mapping within the whole tablet.

The significance and infrared thermal data analysis coupling with the tablet mechanical property prediction model is discussed in detail in chapter 4.

A discrete particle-mechanics simulation model for tablet temperature during compaction is developed in conjunction with the infrared thermal imaging information and presented in chapter 5.

2.3 Effect of Total Process Shear on Powder Blend

Pharmaceutical tablet manufacturing includes several processes, such as powder blending, powder densification, die filling, inter-particle bonding during powder compaction, tablet ejection from die, and tablet relaxation. These processing steps can have a significant effect on tablet properties, such as tensile strength, and dissolution profiles. Lubricant is added to tablet and capsule formulations in a very small quantity (usually 0.25%–2.0%, w/w) to improve the powder processing properties of formulations. Magnesium stearate (MgSt) is one of most common lubricant used in pharmaceutical formulations, and studies have shown the effect of MgSt concentration and total shear applied on powder blend subsequently affect tablet properties.

Studies by Llusa et al. showed that the hydrophobicity of lubricated blends increases as a function of process shear, shear rate, and lubricant concentration. In addition, they reported that the effect of total process shear on the hydrophobicity of lubricated blends is larger than the effect of shear rate [86, 87]. Studies showed that increasing total process shear improves the powder flowability and decreases tablet hardness. Wang et al. observed that hydrophobicity increased as total process shear on powder blend increased [88]. Process shear also influenced drug release rate [89] as shown in Figure 2.14 by Hernandez et al. They reported that as process shear increased the drug release rate decreased. This might be due to over lubrication of extra process shear that formed

a magnesium stearate hydrophobic film covering the active ingredient in the formulation.

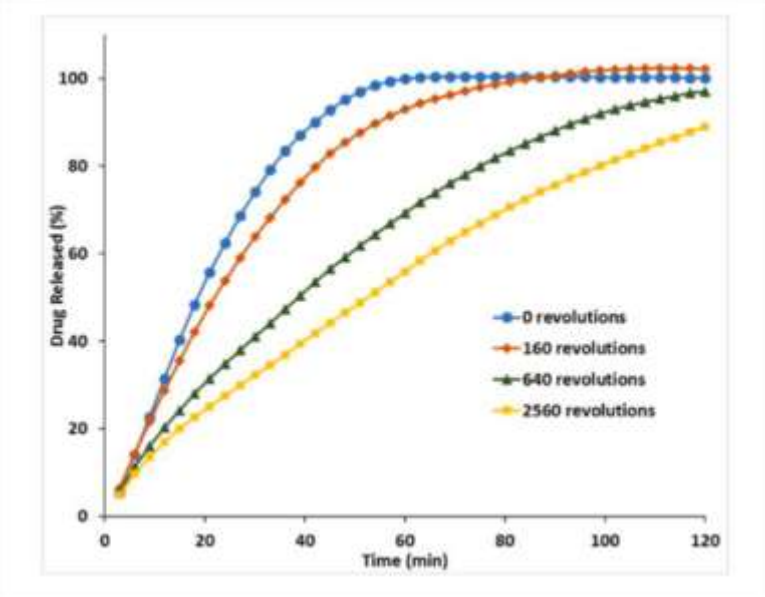

Figure 2.14: The effect of total process shear on the average dissolution profiles of each shear condition, adopted from Hernandez [2016]

Chapter 3

Pharmaceutical Tablet Manufacturing

In oral solid dosage manufacturing for pharmaceutical industry, active pharmaceutical ingredients are mixed with excipient materials and processed through a series of unit operations such as: powder blending, dry/wet granulation, drying, milling, tablet compaction, and tablet coating in order to produce the final drug product [18, 90]. In this chapter we will discuss formulation of materials, blending and process shear, tablet compaction, and tablet surface temperature measurement using non-contact infrared thermal imaging device for this study.

3.1 Formulation of Materials

Lactose (monohydrate N.F., crystalline, 310, regular, Foremost Farms, Rothschild, WI, USA), acetaminophen (APAP; semi-fine crystalline powder, USP/paracetamol PhEur, Mallinckrodt, Raleigh, NC, USA) and magnesium stearate N.F. (MgSt; non-Bovine, Tyco Healthcare/Mallinckrodt, St. Louis, MO, USA) were employed as the test and lubricant materials. Magnesium stearate (MgSt) is commonly used during pharmaceutical formulation development. The model blend with MgSt added as lubricant was blended in V-blender and sheared further in the Couette shearing device to reach the total process shear required.

3.2 Blending and Process Shear

To investigate the effect of different process shear that the powder blend might have experienced during continuous tablet manufacturing operation [91], three cases of batch production were considered. In case 1 (hereafter referred to as No Additional Shear, NAS), lactose (90%, w/w) and APAP (9%, w/w) were blended for 15 minutes at 15 rpm in Twin Shell V-blender (Patterson-Kelley, East Stroudsburg, PA) and then mixed for additional 2 minutes at 15 rpm after MgSt was added. In case 2 (hereafter referred to as 160 Rev sheared), the blended powder from case 1 was unloaded from V-blender and subjected to a controlled shear environment in a modified Couette cell (MCC, Metropolitan Computing Corporation, East Hanover, NJ, USA) at a shear rate of 80 rpm for 2 minutes. In case 3 (hereafter referred to as 640 Rev sheared), the blended powder from case 1 was unloaded from V-blender and subjected to a shear rate of 80 rpm for 8 minutes in the modified Couette cell. Total blend time of NAS, 160 Rev sheared, and 640 Rev sheared cases were 17 minutes, 19 minutes, and 25 minutes respectively. All measurements were conducted at ambient conditions of 22 $\pm$ 3 °C and 30 $\pm$ 5% RH.

Because of the lack of means to access shear rates in a V-blender and therefore estimate the exposure to total shear, mixing time has been the only variable correlated in the literature with blend and tablet properties.

The modified Couette shear device consists of two concentric aluminum cylinders 4.3 in tall and internal cylinder has a diameter of 6.5 in. and the gap between concentric cylinders

is 0.75 in. The internal cylinder can rotate at any speed in the range of 1~245 rpm whereas the external cylinder is stationary. Both cylinders are made of aluminum. The shear device is designed to expose the entire powder blend to a uniform flow and shear environment [86].

Figure 3.1: Twin Shell V-blender (Patterson-Kelley, East Strusburg, PA)

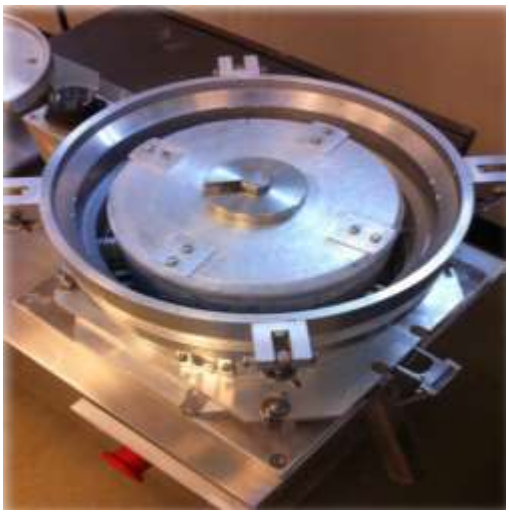

Figure 3.2: The modified Couette shear device

The advantage of modified Couette cell designed with equidistant interlocking pins is that it provides a nearly uniform shear environment in the whole cell [17, 92, 93]. The choice of lactose-APAP formulation is for proof of concept to suggest feasibility of using infrared camera as a characterization tool of manufacturing steps. We have initially selected lactose since it is a more revealing case as the thermal signature is weak due to low plastic deformation resulting in heat.

3.3 Tablet Compaction

Pharmaceutical tablets are normally compressed with tablet press in high speed. The blends prepared in this study are compressed using a tablet press (Figure 3.3, Presster, Metropolitan Computing Corporation, East Hanover, NJ) to simulate a Fette PT 2090 IC, 36 stations press with a press speed of 20 rpm. A dwell time of 22.1 ms (i.e. the time when the flat portion of the punch head is in contact with the compaction roll), is corresponding to a production speed of 43,200 tablets per hour. The ejection angle is set at 5.3°. No pre-compression was used. A set of flat-faced punches, 10-mm diameter, is used to produce 350 mg tablets.

Figure 3.4 shows the evolution of in-die porosity during tablet compaction of tablets with same formulation but subjected to different process shear (No Additional Shear (NAS), 160 Rev sheared, and 640 Rev sheared) compressed at 12 kN. This result is consistent with observations by Mehrotra et al [92], where the particles exposed to higher process shear packed better during die filling.

Figure 3.3: Tablet press, Presster (Metropolitan Computing Corporation, East Hanover, NJ)

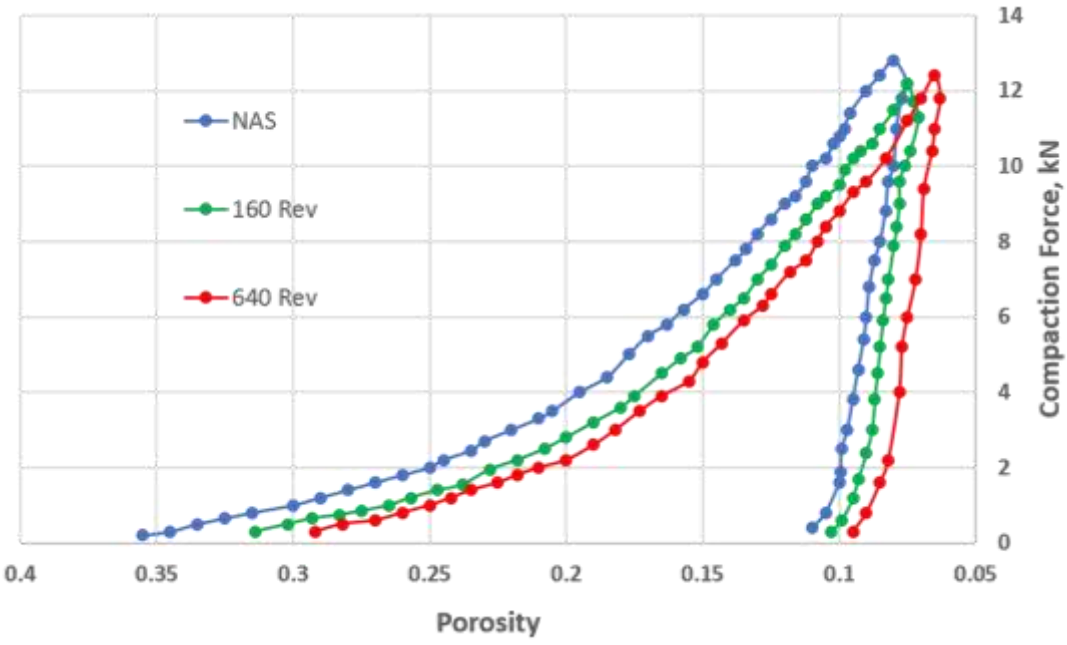

Figure 3.4: The evolution of in-die porosity during tablet compaction of tablets with same formulation but subjected to different process shear (No Additional Shear (NAS), 160 Rev sheared, and 640 Rev sheared) compressed at 12 kN.

3.4 Infrared Thermal Imaging on Tablet

The primary source of infrared radiation is heat. Infrared camera can capture heat signature of pharmaceutical tablets and convert the information for further data analysis.

A calibrated infrared camera (Figure 3.5, ICI Model 7320, Infrared Cameras Inc, Beaumont, TX) is utilized to evaluate the temperature evolution on the surface of the tablet after tablet's ejection from the tablet press. The camera is placed at a distance of 20 cm perpendicular right above the tablet to record infrared image of the tablet, shown in Figure 3.6. All measurements are conducted at ambient conditions of 22 ± 3 °C and $30 \pm 5\%$ RH.

Figure 3.5: Infrared thermal camera, ICI Model 7320

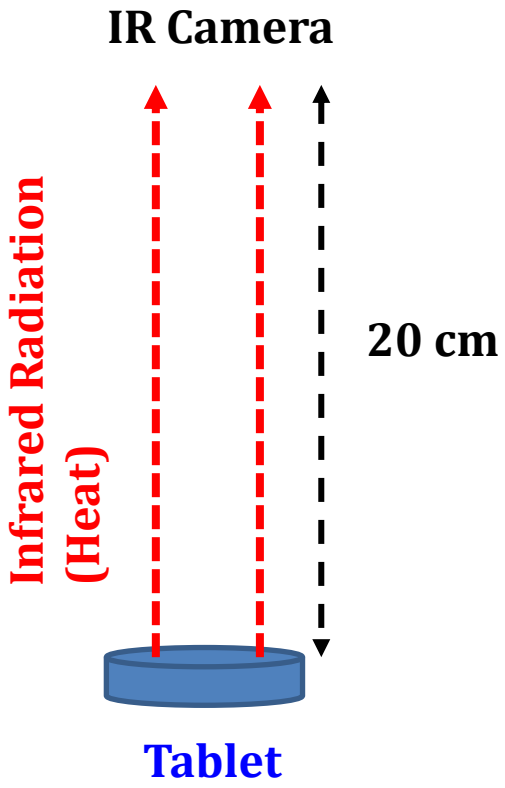

Figure 3.6: Schematic of tablet infrared signature captured by infrared camera

The massive amount of instantaneous IR images (Figures 4.2 (a), (b), (c)) of tablets after ejection from tablet press that are recorded with ICI 7320 IR Flash program and later converted to comma separated values (CSV) files for tablet surface temperature data analysis. In Figure 3.7 is the schematic of tablet IR image converted to CSV file of tablet surface temperature for data analysis. The temperature map of the whole top surface of the tablet is detail to the accuracy of 0.1 °C as shown in the figure.

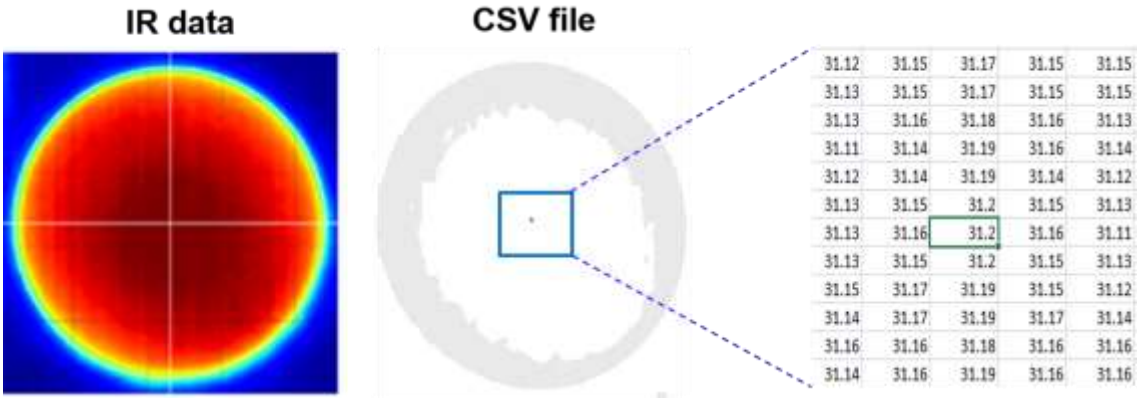

Figure 3.7: The schematic of tablet IR image converted to comma separated values (CSV) file of tablet surface temperature for data analysis, temperature in °C.

Chapter 4

Tablet Property Characterization

The FDA has been promoting process analytical technology (PAT) assessment of pharmaceutical product quality in the production environment. Several PAT techniques such as near-infrared (NIR) spectroscopy [94, 95], Raman spectroscopy [96-98], terahertz pulsed imaging [99, 100], ultrasound [91, 101, 102], and infrared thermal imaging [3, 10-13, 81, 82, 84, 85] have been utilized for characterization of pharmaceutical process and product.

In this chapter we are utilizing infrared (IR) thermal imaging for the first time as a novel real-time monitoring tool with the advantage of non-destructive, non-contact, and non-invasive nature for characterization of manufacturing process of pharmaceutical tablet compaction.

4.1 Thermal Property of Tablet

4.1.1 Non-destructive and Non-contact Infrared Thermography on Pharmaceutical Tablets

As described in chapter 3.3 and 3.4 that the different sheared powder blends (NAS (No Additional Shear), 160 Rev sheared, and 640 Rev sheared) are compacted with various compaction forces into tablets, and the infrared thermographs of the tablets are recorded with infrared thermal camera. The infrared thermal camera is programed to record the thermograph of the tablet at a rate of five frames per second for entire cooling process of the tablet once the tablet is compressed and ejected on the die table of the tablet press. A typical recording of infrared thermographs of a tablet cooling process is about 65 to 75 seconds for a tablet to cool down to room temperature. The recorded thermographs are then converted to comma separated values (CSV) for data analysis.

As shown in Figure 4.1 are infrared thermographs of two tablets compacted from NAS (No Additional Shear, as defined in chapter 3) powder blend with similar compaction forces (24 ± 0.5 kN) compared side by side as time progresses. Compared both tablet 1 and tablet 2 with the temperature results captured by infrared thermal camera as time progresses second by second in Figure 4.1, it is found that top surface temperature of both tablets displayed similar temperature distribution and similar cooling rate while they are compacted with similar compaction force using the same sheared condition powder blend. Similar behavior of tablet temperature distribution and cooling rate results are also

observed on compaction forces of 20 $\pm$ 0.5 kN, 16 $\pm$ 0.5 kN, and on all three cases of powder blends: NAS, 160 Rev sheared, and 640 Rev sheared.

Comparison of infrared thermographs with the progression of time of tablets of all three cases of powder blends: NAS, 160 Rev sheared, and 640 Rev sheared, compacted at 24 $\pm$ 0.5 kN, 20 $\pm$ 0.5 kN, and 16 $\pm$ 0.5 kN are compiled and displayed in Figure 4.2.

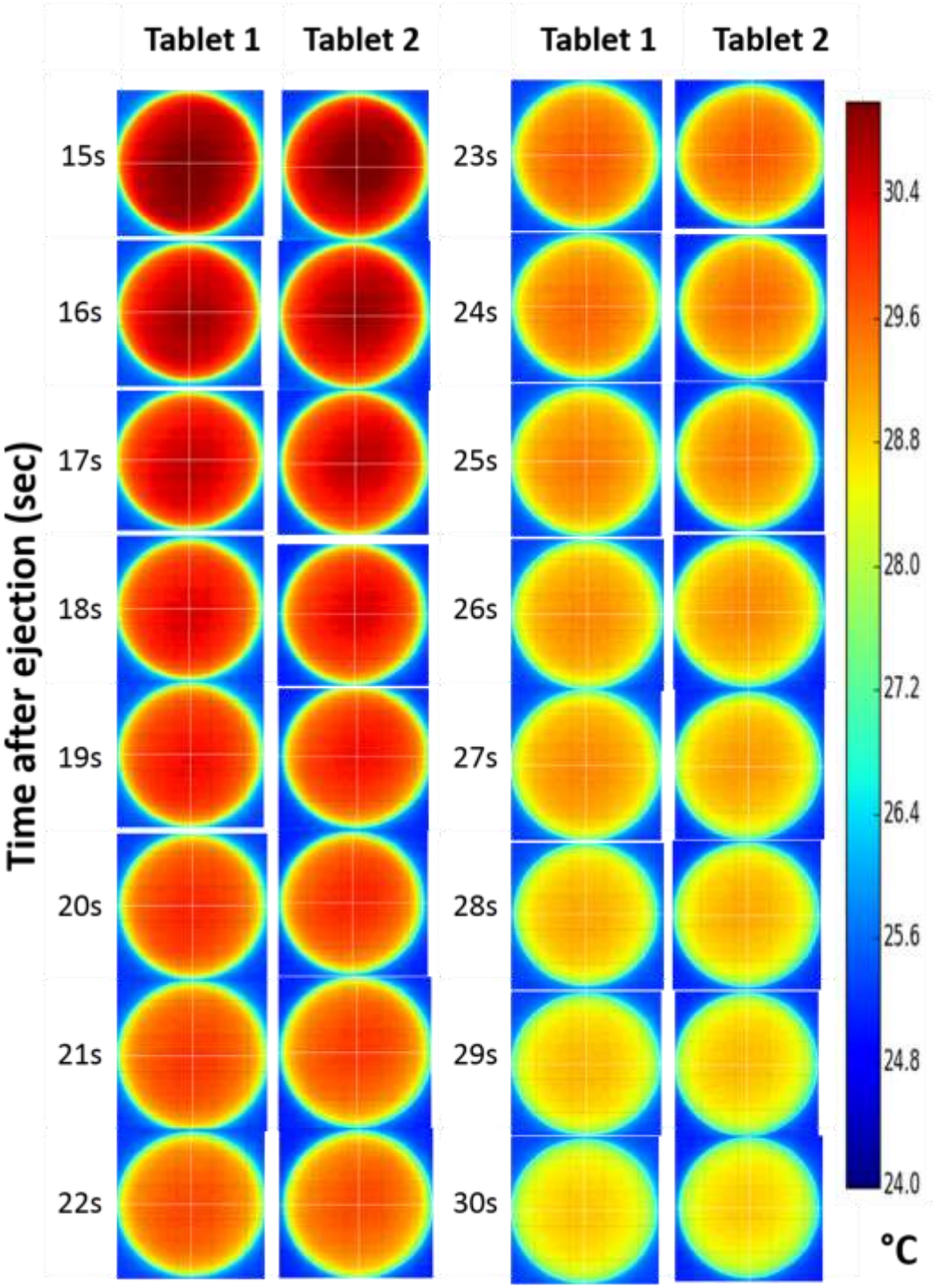

Figure 4.1: Infrared thermographs of two tablets compacted from NAS (No Additional Shear) powder blend with similar compaction forces (24 ± 0.5 kN) compared side by side as time progresses.

Figure 4.2 shows with the progression of time of the infrared thermographs of whole surface area of tablets that were manufactured with same formulation but subjected to different process shear conditions and compacted at similar compaction force of (a) 24 $\pm$ 0.5 kN, (b) 20 $\pm$ 0.5 kN, and (c) 16 $\pm$ 0.5 kN. There is instantaneous real-time visible difference in the infrared thermographs to differentiate tablets experienced different process shear.

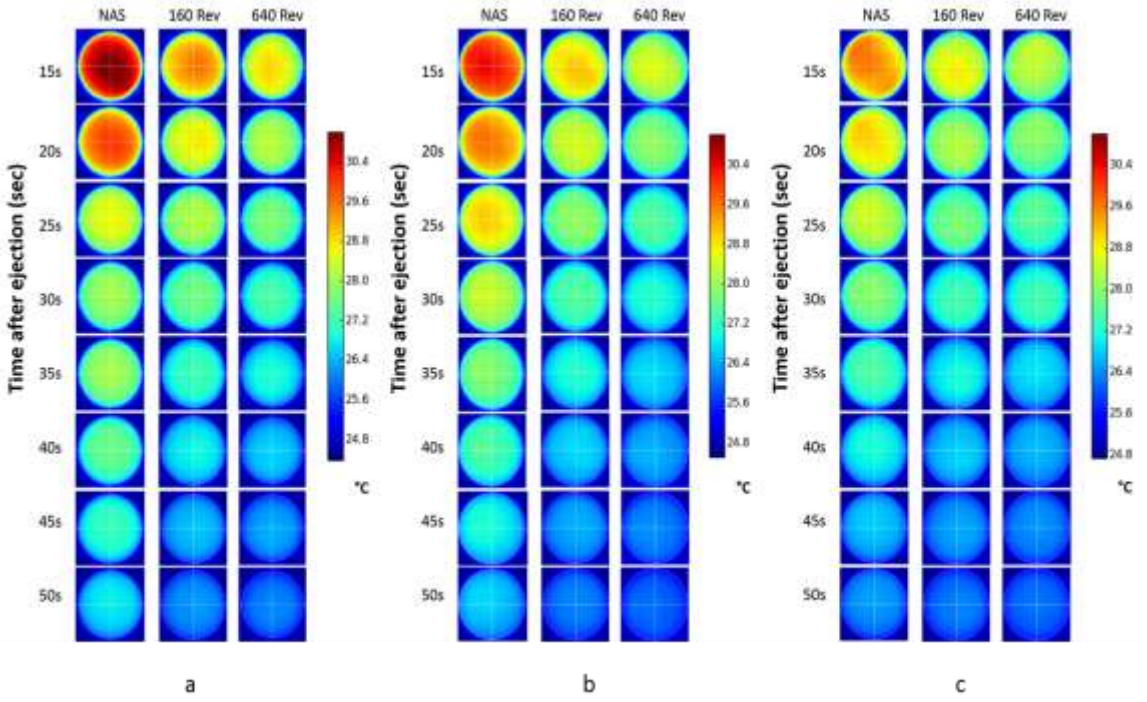

Figure 4.2: Infrared thermographs of tablets with the progression of time of the same formulation but subjected to different process shear (No Additional Shear (NAS), 160 Rev sheared, and 640 Rev sheared) compacted with similar compaction forces at (a) 24 $\pm$ 0.5 kN, (b) 20 $\pm$ 0.5 kN, and (c) 16 $\pm$ 0.5 kN.

4.1.2 Tablet Temperature vs Time Profiles

Figure 4.3 illustrates the time evolution of the maximal temperature on the top surface of tablets after being ejected from the die.

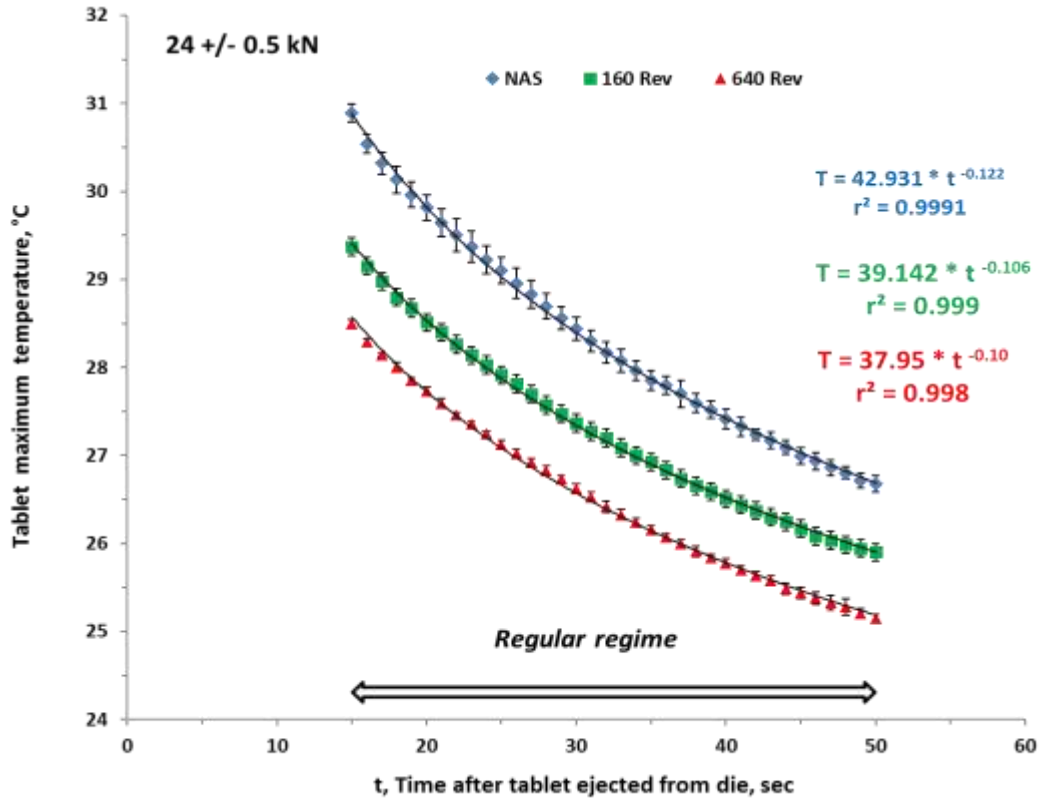

Figure 4.3: Tablets compacted at 24 ± 0.5 kN with No Additional Shear (NAS), 160 Rev sheared, and 640 Rev sheared powder blends.

These tablets are manufactured using similar compaction force, but the blends are subjected to three different process shear conditions. The result shown in Figure 4.3 demonstrates strong sensitivity of measured temperature profiles to the powder process shear conditions. Result shows that with similar compaction force during compaction of tablets the lesser

sheared powder blend exhibits distinguishably higher measured tablet surface temperatures. It is worth noting that the tablet temperature difference between sheared and non-sheared powders reflects the change in physicochemical behavior of the particle surface as a result of process shear. This significant difference in tablet temperature can be attributed to the deposition of thin layers of lubricant (MgSt) film on the surface of powder particles [17]. It is also possible that the change in surface energies of powder particles due to process shear and alter the contact mechanics between adjacent particle surfaces and the pattern when these powder particles rearrange under compaction thus changing the tablet temperature. Utilizing infrared camera to measure tablet temperature in real time, can provide a calibrated temperature profile for manufacturing quality control during continuous tablet manufacturing operation.

In addition, collected temperature distributions data can be used to determine the tablet thermal diffusivity among other parameters, which is related to a tablet's pore microstructure formed during compaction. The information of tablet surface temperature with progression of time also allows us to estimate the initial tablet temperature immediately after the compaction. The estimated initial tablet temperature immediately after the compaction with 24 ± 0.5 kN compaction force for NAS is ~ 42.9 °C, for 160 Rev sheared is ~ 39.1 °C, and for 640 Rev sheared is ~ 37.9 °C.

Figure 4.4 shows the tablet surface temperature profile from left edge to right edge of the tablet at 15 sec after the tablet's ejection from die with compaction force of 24 ± 0.5 kN, 20 ± 0.5 kN, and 16 ± 0.5 kN for all three different process shear conditions. There is a

clear distinction that less sheared formulation has higher tablet surface temperature. For example, in Figure 4.4 (a), tablets compacted with 24 $\pm$ 0.5 kN, at 15 sec after ejection from tablet press, the maximum temperature recorded near the center of tablet is ~ 31.2 °C for NAS case, ~ 29.6 °C for 160Rev sheared case, and ~ 29.1 °C for 640Rev sheared case. This is a significant indication of heat generated during compaction at the particle interface due to frictional interactions between moving powder particles and within the particles due to irreversible deformation. More heat is generated with less sheared formulation like NAS case which has less evenly distributed MgSt as lubricant among excipient particle surface. On the contrast, less heat exhibit with more uniformly distributed of lubricant on 160 Rev sheared and 640 Rev sheared cases.

Figure 4.5 shows the cooling process of tablet surface temperature with the progression of time from left edge to right edge of tablet of NAS, 160 Rev sheared, and 640 Rev sheared cases compacted at 24 $\pm$ 0.5 kN.

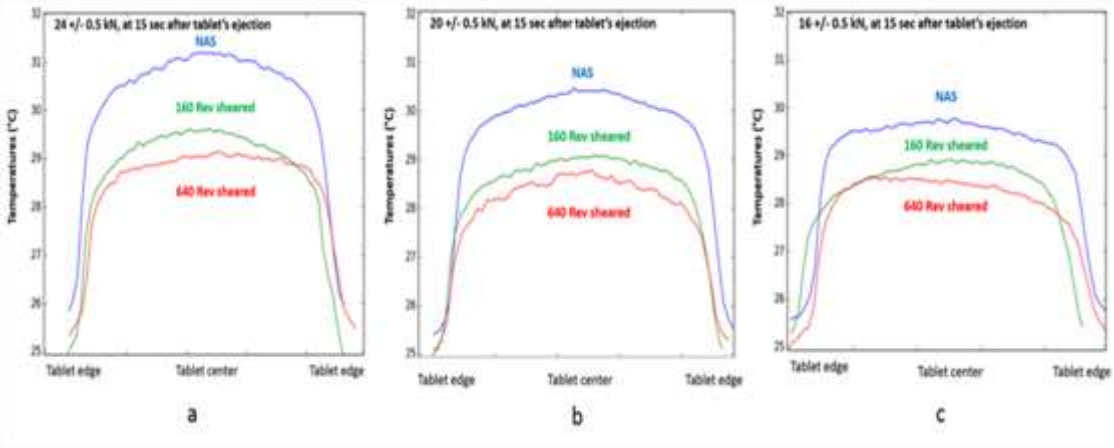

Figure 4.4: Temperature profile of tablets (view from above the tablet) from edge to edge at 15 sec after ejection from die with same formulation but subjected to different process shear (No Additional Shear, NAS (Blue), 160 Rev sheared (Green), and 640 Rev sheared (Red)) compressed at (a) 24 $\pm$ 0.5 kN, (b) 20 $\pm$ 0.5 kN, and (c) 16 $\pm$ 0.5 kN.

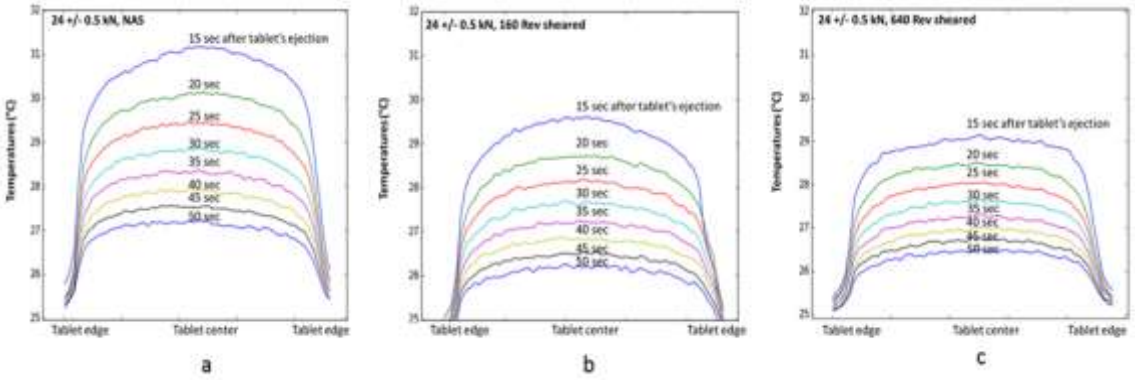

Figure 4.5: Temperature profile as time progress (15 ~ 50 sec, view from above the tablet) from edge to edge of tablet compressed at 24 $\pm$ 0.5 kN of (a) No Additional Shear (NAS), (b) 160 Rev sheared, and (c) 640 Rev sheared.

4.2 Regular Regime of Tablet Cooling

Consider cooling of a homogeneous body having initial temperature $T_i(x, y, z, t)$, which is put in surroundings of constant temperature T_{env} , with a constant surface heat transfer coefficient. The solution of the corresponding heat conduction problem is:

$$T_i(x, y, z, t) - T_{env} = \sum_{n=1}^{\infty} \mathrm{c_n}\varphi_\mathrm{n}(x, y, z)e^{-m_n t} \qquad \text{Eq. 1}$$

where c_n are constant coefficients, the factors $\varphi_\mathrm{n}(x, y, z)$ are functions of coordinates only. Note that the eigenvalues m_n are positive and satisfy the inequality $m_1 < m_2 < \ldots < m_n < \ldots$ Thus, higher order terms of the series in Eq. 1 rapidly decrease with time, *t*, and at a certain moment of time can be neglected. The temperature field is then described by the first dominant term in Eq. 2:

$$T_i(x, y, z, t) - T_{env} \approx \mathrm{c_1}\varphi_1(x, y, z)e^{-m_1 t} \qquad \text{Eq. 2}$$

which indicates that regular cooling is established. The function $\varphi_1(x, y, z)$ does not depend on initial conditions, therefore the regular cooling process is fully determined only by the boundary conditions and the physical properties of the body. Taking the logarithm of the Eq. 2 yield Eq. 3:

$$\log(T_i(x, y, z, t) - T_{env}) = -m_1 t + \log(\mathrm{c_1}\varphi_1(x, y, z)) \qquad \text{Eq. 3}$$

shows that the logarithm of excess temperature changes linearly in time at all points of the body [103]. Moreover, the slope of such linear functions m_1 is the same for all points, and is called the *rate of cooling*.

Summarizing, the entire cooling process can be divided into two stages, before reaching the steady state. The first *transient* stage is characterized by the strong dependence of the initial temperature distribution, and the temperature evolution is described by Eq. 1. The second stage is called the *regular regime* [104, 105], described by Eq. 2.

It should be noted that the pharmaceutical tablets are in general heterogeneous, thus the spatial variability of the cooling rate in the regular regime might be expected. Experimental results, however indicate close values for the fitted slopes evaluated at different points on the tablet's surface as shown in Figure 4.6 (a), (b) and (c) for NAS, 160 Rev sheared, and 640 Rev sheared blends compacted at 24 ± 0.5 kN.

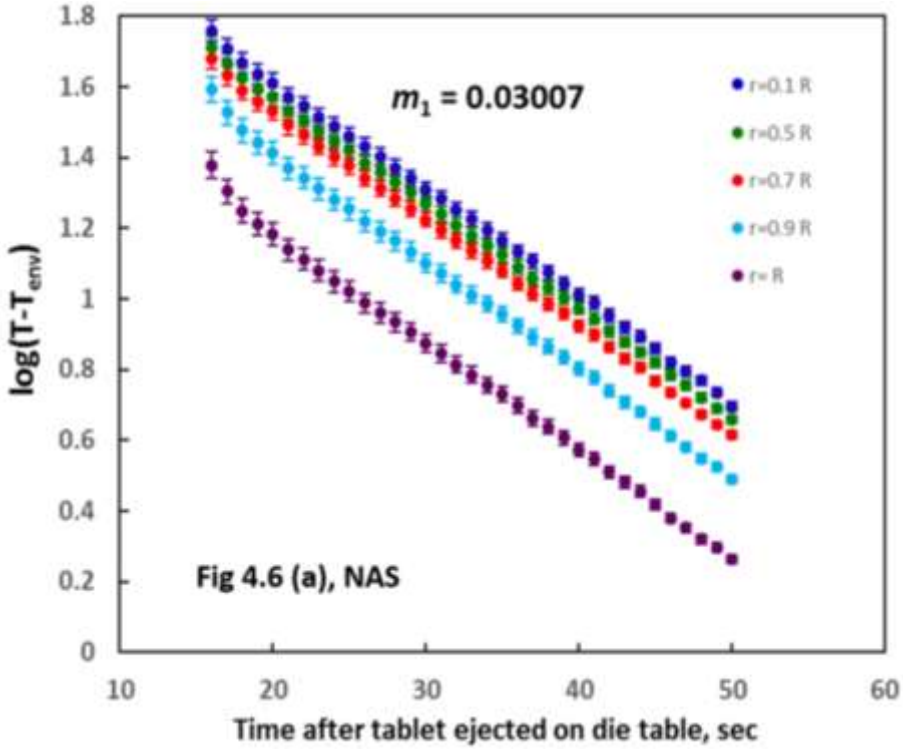
m_1 = 0.03007
r=0.1 R
r=0.5 R
r=0.7 R
r=0.9 R
r= R
Fig 4.6 (a), NAS
log(T-T$_{env}$)
Time after tablet ejected on die table, sec

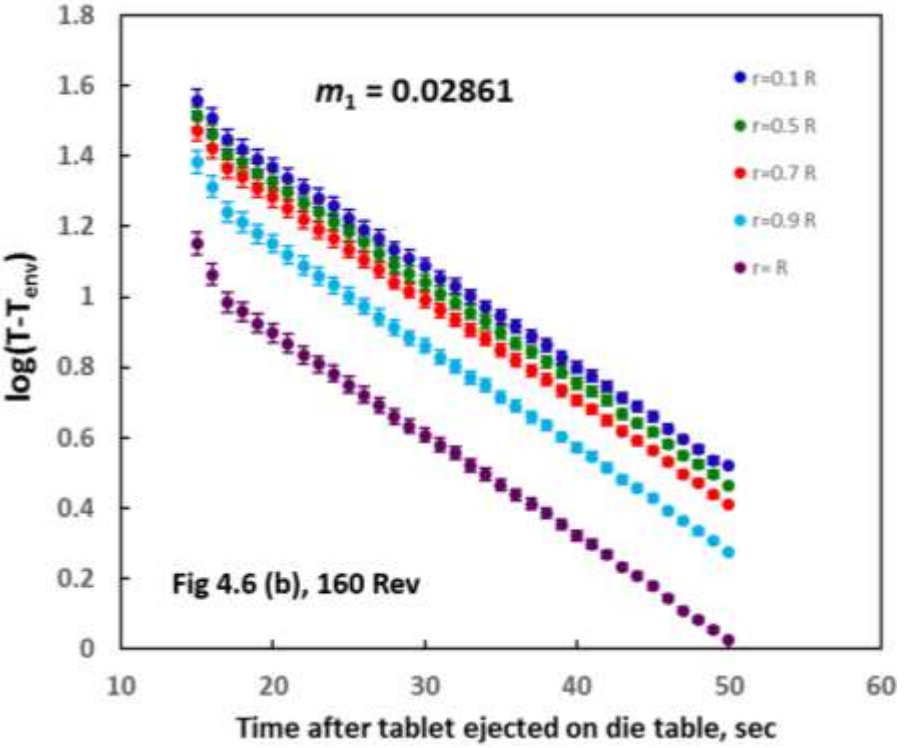
m_1 = 0.02861
r=0.1 R
r=0.5 R
r=0.7 R
r=0.9 R
r= R
Fig 4.6 (b), 160 Rev
log(T-T$_{env}$)
Time after tablet ejected on die table, sec

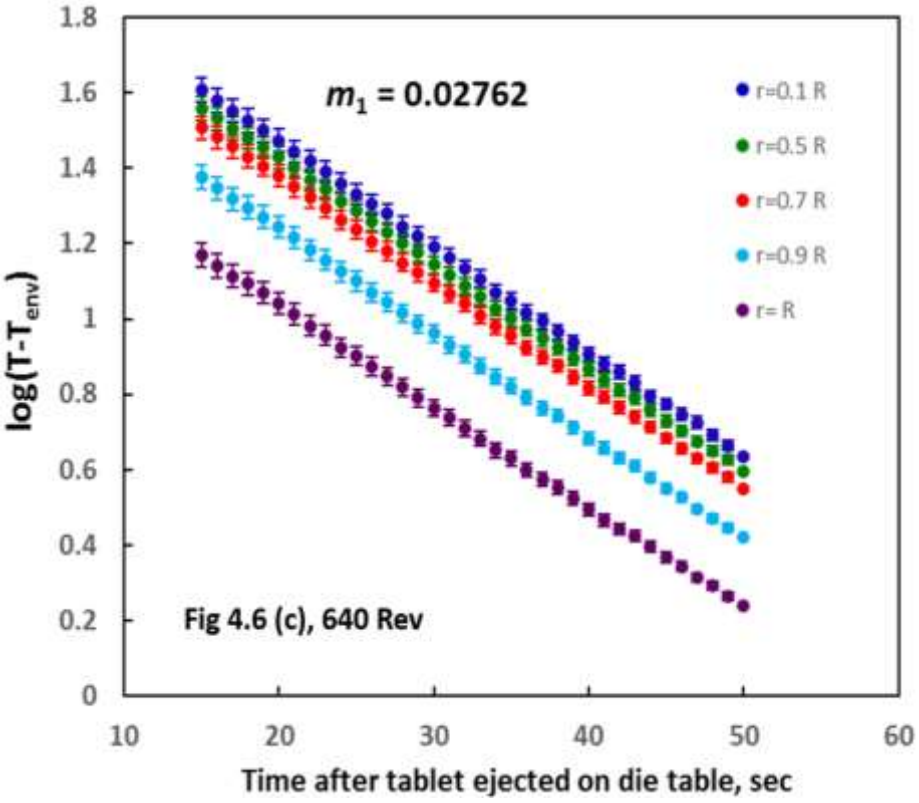

Figure 4.6: log (T- T_{env}) vs time (i.e. slope, m_1) after tablet ejected from die at location of r = 0.1R, 0.5R, 0.7R, 0.9R, and R of tablet compressed at 24 $\pm$ 0.5 kN of (a) No Additional Shear (NAS), (b) 160 Rev sheared, and (c) 640 Rev sheared.

In Figure 4.7, we present the relationship between the average slope of log (T- T_{env}) vs time, m_1, and relative density, $\bar{\rho}$, of compacted tablets from three cases of powder blends.

Table 4.1 lists the estimated slope of log (T- T_{env}) vs time at zero porosity, $m_{1,0}$, of all three cases. $m_{1,0}$ values are calculated by substituting $\bar{\rho} = 1$ (i.e. $m_{1,0}$ = rate of cooling of tablet at zero porosity) into the linear fit equation in each case shown in Figure 4.6.

Figure 4.8 shows that the rate of cooling of tablet at zero porosity, $m_{1,0}$, decreases as the level of process shear increases during formulation process.

A novel correlation model toward predicting tablet tensile strength is presented in section 4.3.2. This novel model only needs (i) the relative density of tablet and (ii) the tablet's rate of cooling at *regular regime,* m_1, from IR measurements as a non-destructive method of measurable critical quality attribute (CQA) for pharmaceutical tablet quality control.

Cases	$m_{1,0}$	r^2
NAS	0.0399	0.935
160 Rev sheared	0.0366	0.966
640 Rev sheared	0.0330	0.958

Table 4.1: Estimated slope of log (T- T_{env}) vs time at zero porosity, $m_{1,0}$, of all three cases.

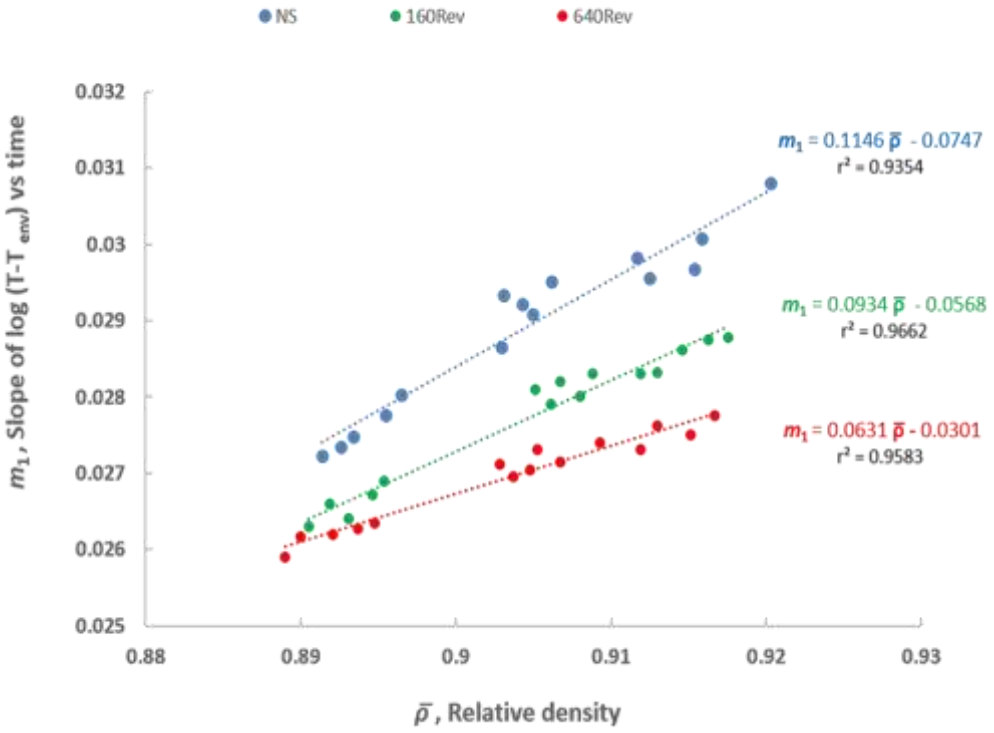

Figure 4.7: The relationship between the average slope of log (*T*- T_{env}) vs time, m_1, and relative density, $\bar{\rho}$, of compacted tablets of three different total process shear (NAS, 160 Rev sheared, and 640 Rev sheared) powder blends.

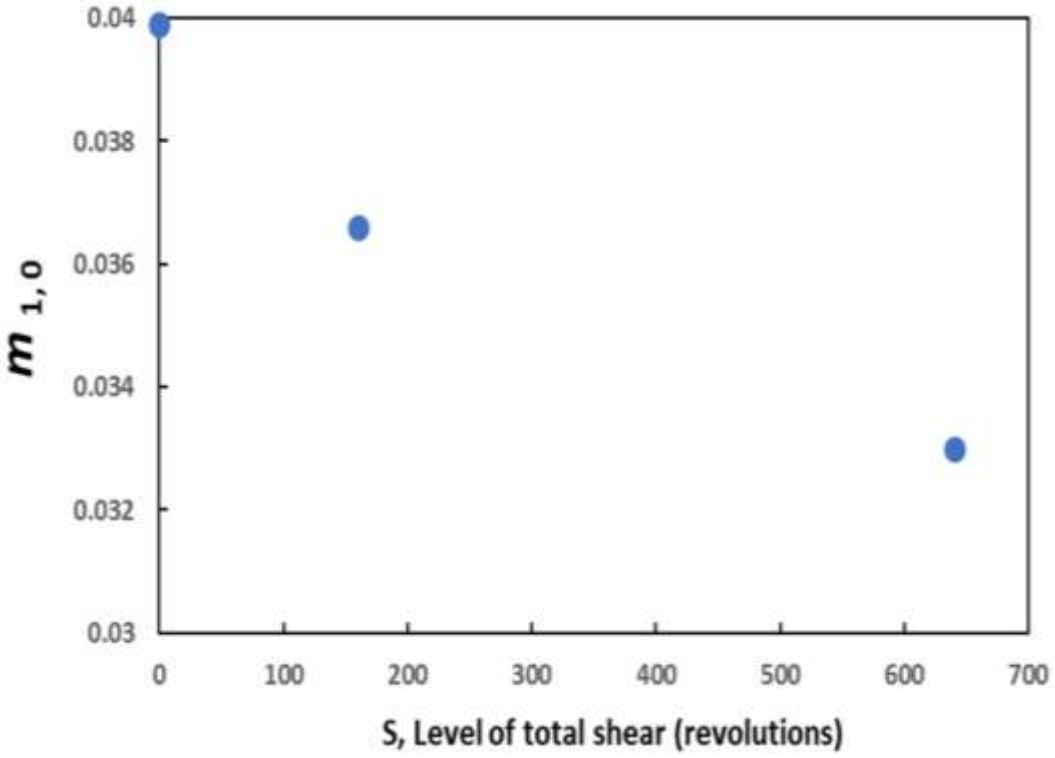

Figure 4.8: The relationship between the rate of cooling of tablet at zero porosity, $m_{1,0}$, and the level of total process shear of powder blend experienced during formulation process

4.3 Strategy Toward Predicting Tablet Tensile Strength

Higher tablet temperature observed during tablet compaction indicates that there is more heat generated from irreversible deformation on powder particles during the compaction process into tablet.

4.3.1 Mechanical Property Measurement of Tablet with Destructive Method

To further investigate the mechanical properties of the tablets compressed from different process shear conditions, the diametrical compression test is performed using a standard mechanical hardness tester (Dr. Schleuniger Pharmatron, Model 6D, Manchester, NH). The tensile strength of tablets, σ_t is calculated by [106]

$$\sigma_t = \frac{2F}{\pi D t} \qquad \text{Eq. 4}$$

where F is breaking force and D is the diameter of the tablet, which is assumed to be constant and equal to 10 mm as radial relaxation was minimal, *t* is the thickness of the tablet.

In Figure 4.9, we show the relationship between tablet tensile strength and relative density of compacted tablets of all three cases of powder blends. As expected, the process shear reduces tablet tensile strength due to the smearing effect of MgSt. Blends with the same

formulation but experiencing different level of process shear result in different mechanical properties. This has been reported in the literature, for example in Razavi et al.[91] and Pawar et al. [107].

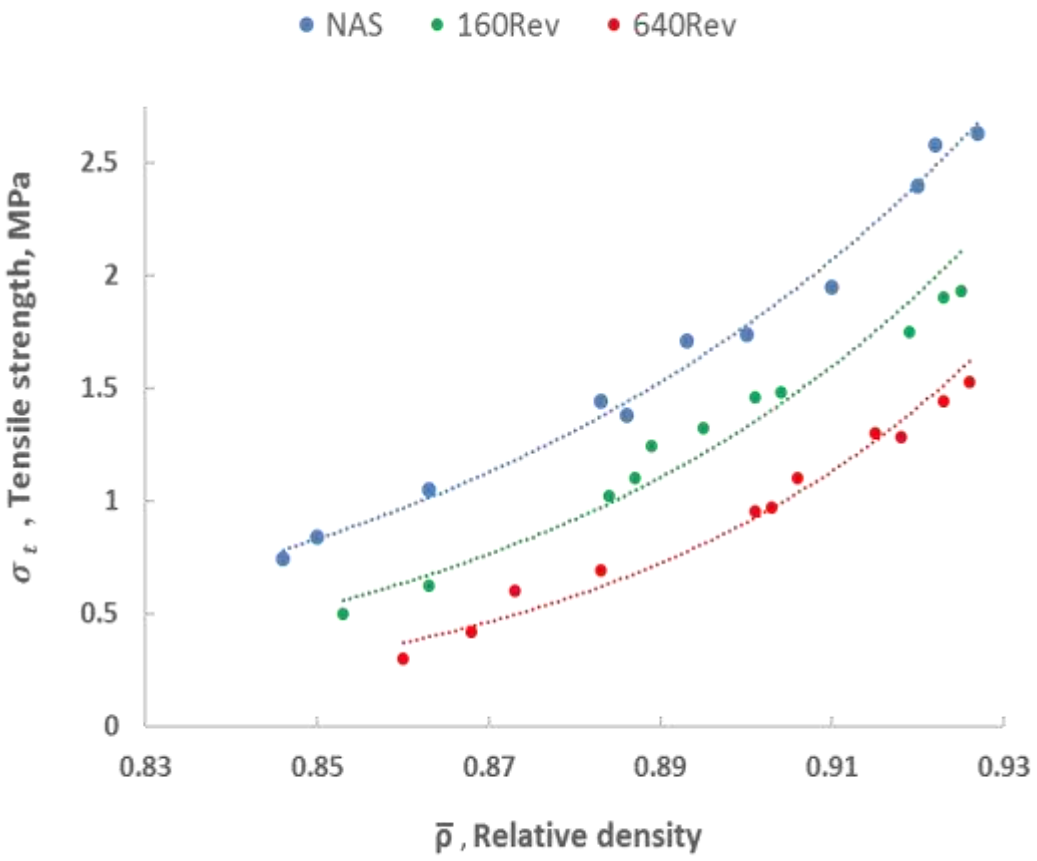

Figure 4.9: The relationship between tablet tensile strength, σ_t , and relative density, $\bar{\rho}$, of compacted tablets of three different total process shear (NAS, 160 Rev sheared, and 640 Rev sheared) powder blends.

Consider a theoretical model based on percolation theory proposed by Kuentz and Leuenberger [108] to relate tensile strength, σ_t , and relative density, $\bar{\rho}$:

$$\sigma_t = \sigma_0[1 - \left(\frac{1-\bar{\rho}}{1-\rho_{c,\sigma_t}}\right) exp^{(\bar{\rho}-\rho_{c,\sigma_t})}] \quad \text{Eq. 5}$$

where σ_0 is the tensile strength at zero porosity and ρ_{c,σ_t} is the critical relative density at which σ_t goes to zero.

Relationship between σ_t and $\bar{\rho}$ is normally presented by an exponential form [109-111]. This relationship is empirical and does not provide the limiting values of σ_0 and ρ_{c,σ_t} which is needed to implement the model in Eq. 5.

From the data in Figure 4.9, the diametrical compression test results were fitted into Eq. 5 using the non-linear regression method based on the Trusted-Region algorithm [112]. Table 4.2 listed the tensile strength at zero porosity (σ_0) and critical relative density (ρ_{c,σ_t}) found from Eq. 5 for all three different produced tablets. The results of our finding are consistent with data in Razavi et al. [91].

Cases	σ_0(MPa)	ρ_{c,σ_t} (%)	r^2
NAS	4.81	81.4	0.948
160 Rev sheared	3.45	82.2	0.926
640 Rev sheared	2.89	83.0	0.912

Table 4.2: Tensile strength at zero porosity (σ_0) and critical relative density (ρ_{c,σ_t}) found from Eq. 5 for all three different produced tablets.

4.3.2 Non-destructive Tablet Mechanical Property Prediction Model

Based on the results from Table 4.1 and 4.2, we present in Figure 4.10 a one-to-one relationship between tensile strength at zero porosity (σ_0), slope of log (T- T_{env}) vs time at zero porosity ($m_{1,0}$) , and critical relative density (ρ_{c,σ_t}), of blends with the same formulation but experienced three different level of process shear. The one-to-one relationship between σ_0 , $m_{1,0}$, and ρ_{c,σ_t} of compacted tablets is displayed in Equations 6.1 and 6.2.

$$\sigma_0 = 276.41\left(m_{1,0}\right) - 6.37 \qquad \text{Eq. 6.1}$$

$$\rho_{c,\sigma_t} = -2.317\left(m_{1,0}\right) + 0.907 \qquad \text{Eq. 6.2}$$

Substituting Eqs. 6.1 and 6.2 from experimental data into Eq. 5 yield Eq. 7. We develop the following model toward predicting tablet tensile strength if provided with $m_{1,0}$ and $\bar{\rho}$ information.

$$\sigma_t = [276.41\left(m_{1,0}\right) - 6.37][1 - \left(\frac{1-\bar{\rho}}{0.083+2.317(m_{1,0})}\right) exp^{(\bar{\rho}+2.317(m_{1,0})-0.907)}] \qquad \text{Eq. 7}$$

where $m_{1,0}$ is the slope of log (T- T_{env}) vs time at zero porosity and $\bar{\rho}$ is the relative density of tablet. ($\bar{\rho} = \frac{\rho_b}{\rho_t}$, ρ_b is bulk density of tablet, ρ_t is true density of blend)

Base on Kuentz and Leuenberger's model, for the first time, we developed a novel correlation model (see Eq. 7) toward predicting tablet tensile strength as a non-destructive method that only needs (i) the tablet's rate of cooling at *regular regime* obtained from IR measurement and (ii) relative density of tablet. [113] (For the model blend of Lactose/APAP/MgSt = 90%/9%/1%)

Figure 4.11 shows the prediction of relationship between tablet tensile strength, $\sigma_{t,\,E_q\,7}$, and relative density by applying various rate of cooling of tablet at zero porosity, $m_{1,0}$, of the range from 0.040 to 0.030 to the model developed in Eq. 7. The range of prediction for unknown sample's tablet tensile strength is presented in Figure 4.11 for relative densities between 0.89 to 0.93 with this non-destructive/non-contact method. As expected, the tensile strength of tablet decreases as the level of process shear increases.

Results in this prediction model are consistent with data in Figure 4.9 using destructive method. The advantage of utilizing infrared thermal imaging as a potential PAT tool for a tablet tensile strength prediction model is that it is a non-destructive and non-contact method with real-time instant result of tablet tensile strength without breaking the tablet.

Here we present a strategy, for the first time, a non-destructive and non-contact infrared thermal imaging is utilized to determine the variation of total process shear on powder blend and to systematically study the effect of these process shear variations on tablet tensile strength. With a simple transient temperature measurement by infrared thermal

camera on the whole surface of tablet after its ejection from tablet press, the thermal signature of the powder blend with respect to the process shear variations in terms of just one parameter that we defined as "tablet's rate of cooling in regular regime, m_1", is calculated with infrared thermal imaging experimental result.

A model toward predicting tensile strength is developed that only needs the rate of cooling of tablet at zero porosity, $m_{1,0}$, from the infrared thermal imaging to account for tablet mechanical property variations. Thus, $m_{1,0}$, is defined as a function of the level of total process shear that the powder blend experienced during formulation process and $m_{1,0}$ decreases as total shear strain increases. (i.e. $m_{1,0} \approx f$ *(Shear),* as shown in Figure 4.11) Then, tablet mechanical property is determined by the powder blend's formulation process and compaction process as described in Eq. 7 (i.e. $\sigma_t \approx f$ *(Shear, Compaction force)* $\approx f($ $m_{1,0}$ *, Relative density)* $\approx f($ $m_{1,0}$, $\bar{\rho}$)) and shown in Figure 4.11.

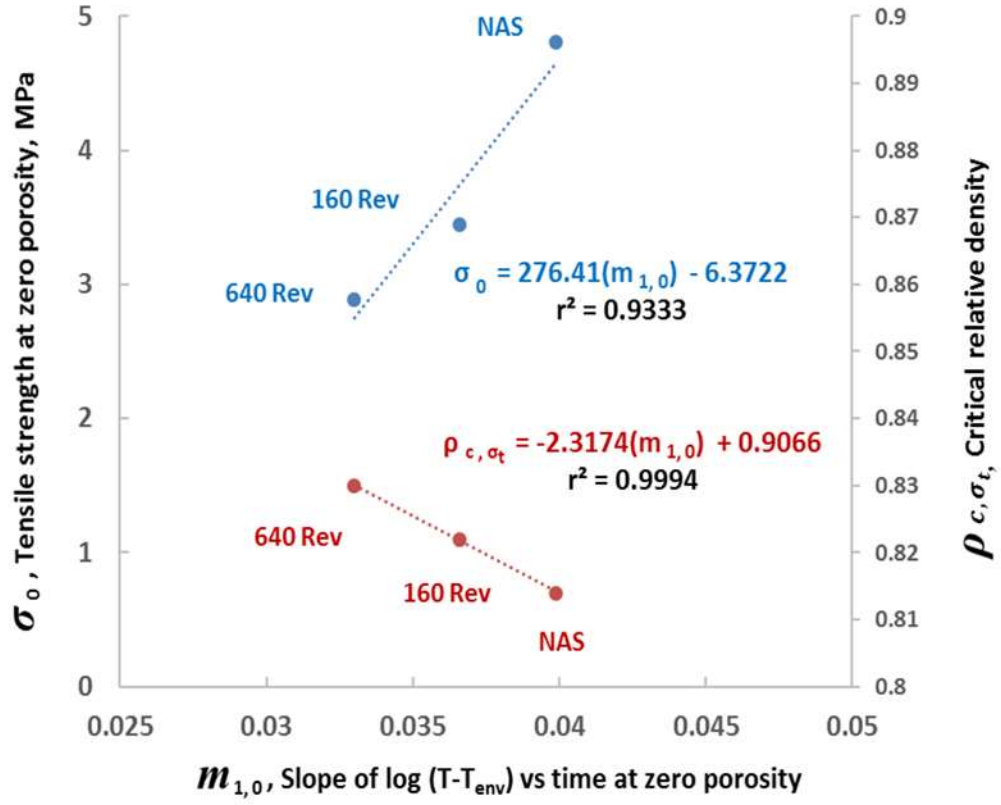

Figure 4.10: One-to-one relationship between σ_0 , $m_{1,0}$, and ρ_{c,σ_t} of compacted tablets of three different total process shear (NAS, 160 Rev sheared, and 640 Rev sheared) on powder blends.

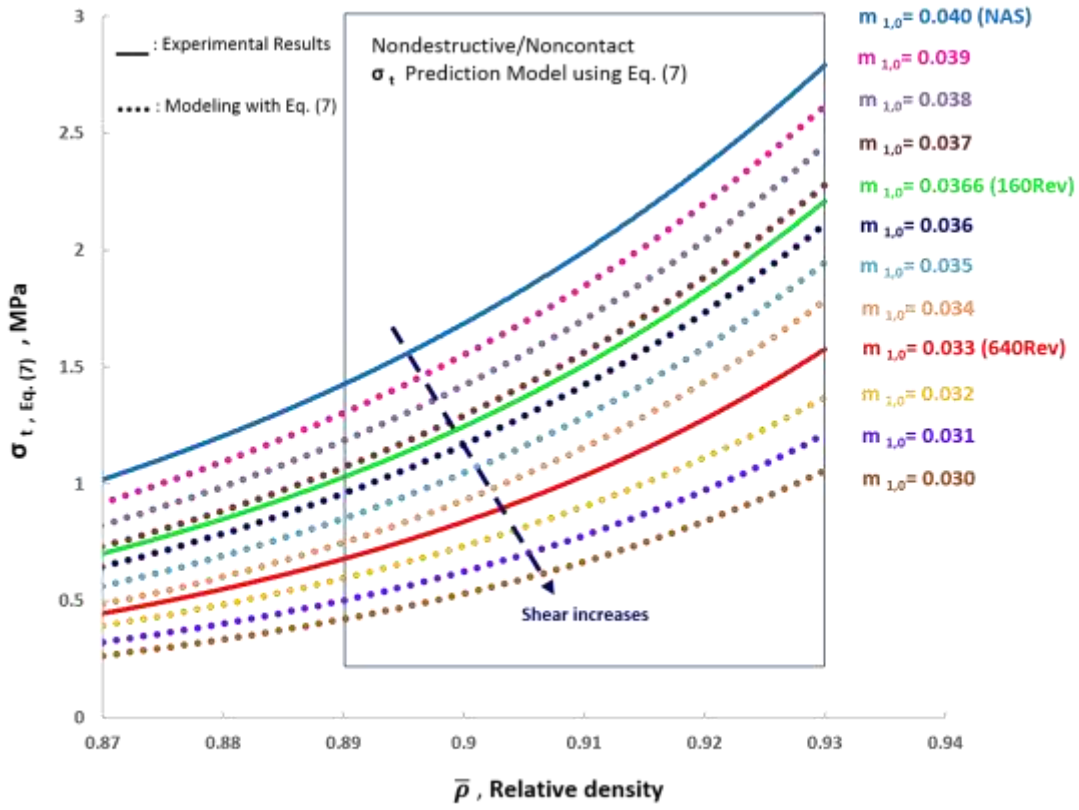

Figure 4.11: The relationship between tablet tensile strength, $\sigma_{t,\ Eq.\ 7}$, and relative density, $\bar{\rho}$, by applying tensile strength prediction model using Eq. 7.

4.4 Conclusion

There is great potential of using infrared thermal imaging as a non-destructive and non-contact PAT technique for quick screening of the tablet production with pharmaceutical powder subjected to different process shear conditions. We successfully used infrared (IR) measurement system on monitoring tablet's detail thermal signature during compaction process. The effect of two processing parameters: compaction force and level of total shear were examined. IR measurement of tablet's rate of cooling, m_1, at *regular regime* was found to be sensitive to the relative density and the level of total process shear.

With IR measurement, a correlation between tablet's rate of cooling at *regular regime* and tablet's tensile strength is presented. The transient temperature peak exhibits at the center of the tablet. The tablet temperature profile collected by IR after tablet's ejection from tablet press provides a unique insight of transient temperature changes. This information can also provide guidance of temperature operating ranges when processing temperature sensitive formulations. The advantage of using the infrared thermal imaging is that this technique is easy to use and provides a unique thermal signature, $m_{1,0}$, of powder blend's total process shear during formulation process toward developing a model to predict tablet tensile strength and it is also a good candidate to be placed on/at-line as a non-destructive and non-contact PAT tool with instant real-time results.

Chapter 5

Computational Modeling of Tablet Temperature Distribution During Compaction

5.1 Introduction

During the process of consolidation, particles come into contact to form numerous arrangements which ultimately determine their macroscopic mechanical and thermal properties.

Heat transfer of particulate systems in pharmaceutical tablet manufacturing [114] is important element to be considered, yet is not fully understood. In this study, we utilize computational tools based on discrete particle-mechanics to describe the formation of networks during the consolidation process. These heterogeneous networks are subsequently used to simulate the heat transfer process after tablet ejection from die. We demonstrate the computational modeling match well with experimental results from infrared measurement, which have not been previously reported.

Utilizing computational modeling of the pharmaceutical powder compaction process to understand and investigate the compaction process in detail, particularly the interactions between individual particles and the heterogeneity in the bulk is essential for the advancement of pharmaceutical research and development.

5.2 Computational Modeling: Discrete Particle-Mechanics Approach

Various methods have been used for the numerical simulation of tablet compaction, we utilize discrete particle-mechanics approach to study the nature of thermo-mechanical interaction which determines the microstructure of the confined granular materials [115-117].

The discrete particle-mechanics approach which is similar to the concept of Vargas and McCarthy [118, 119] of their introduction of a mathematical model as an extension to the discrete element model of granular materials [120]. However, discrete particle-mechanics approach is based on defining particle's final state, such as position and temperature, rather than tracing particles during the compaction process.

Discrete particle-mechanics simulation captures the macroscopic behavior of a particulate system by calculation of the trajectories of each of the individual particles within the mass and the time evolution of these trajectories then determines the global flow of the granular material [118]. These particle trajectories are obtained by explicit solution of Newton's equations of motion for every particle [120]. The forces on the particles are determined from contact mechanics considerations [121], these forces include normal, Hertzian, repulsion and some approximation of tangential friction [122].

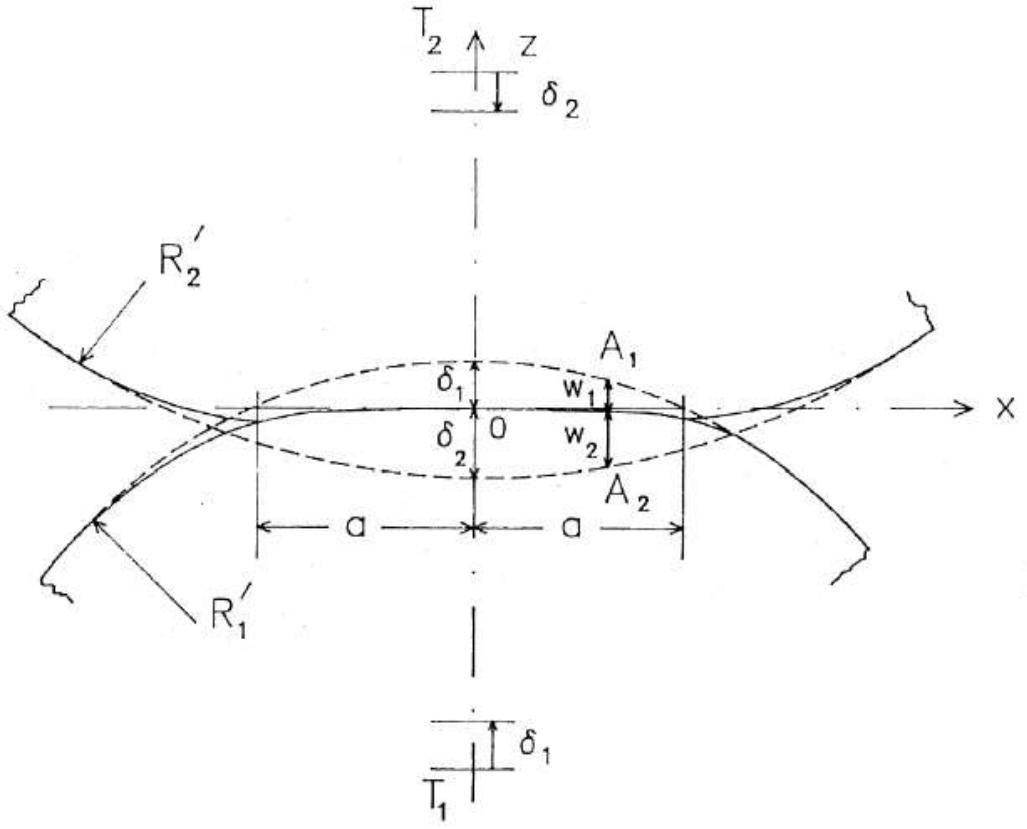

Figure 5.1: Contact Mechanics, adopted from Johnson [1987]

The specific key feature of discrete particle-mechanics simulation is that many simultaneous two-body interactions may be used to model a many-body system. This methodology works by choosing sufficiently small time-step such that any disturbance does not propagate further than that particle's immediate neighbors within one time-step. This criterion is met by choosing a time-step which is smaller than $r/\boldsymbol{\lambda}$, where r is the particle radius and $\boldsymbol{\lambda}$ represents the relevant disturbance wave speed [123].

Contact mechanics [121] of a two-body interaction is well understood that allows particle-mechanics simulations to accurately reflect particle mechanical properties and contact

conductance model is also well established [124-126], so the approach in our study is utilizing contact mechanics with discrete particle-mechanics simulation in the context of heat transfer.

By integrating the well-known theory of Hertzian deformation [127] for quasi-static mechanics and conductive heat transfer for spherical conforming contacts of granular media. The total heat, Q_m, transferred to individual particle *m* from neighboring particles *n* and the total forces, F_m, acting on particle *m* are equated to zero.

$$Q_m = \sum_{n \epsilon N_m} \mathrm{Q}_{mn} = 0 \qquad \text{Eq. 8.1}$$

$$F_m = \sum_{n \epsilon N_m} F_{mn}\, \boldsymbol{n}_{mn} = 0 \qquad \text{Eq. 8.2}$$

where $\boldsymbol{n}_{mn}$, is the unit normal vector defined from centers of particle *n* to particle *m*

$$\boldsymbol{n}_{mn} = \frac{X_m - X_n}{\| X_m - X_n \|} \qquad \text{Eq. 8.3}$$

Adopting Batchelor and O'Brien's model [128] for predicting the heat conductance, which is the ability of two touching surfaces to transmit heat through their mutual interface.

$$Q_{mn} = H_{mn} \left(T_m - T_n \right) \qquad \text{Eq. 8.4}$$

$$H_{mn} = 2\, a_{mn}\, k_{mn} \qquad \text{Eq. 8.5}$$

$$a_{mn} = \sqrt{\gamma_{mn} R_{mn}} \quad \text{Eq. 8.6}$$

$$k_{mn} = \frac{1}{2} \left[\frac{1}{k_m} + \frac{1}{k_n} \right]^{-1} \quad \text{Eq. 8.7}$$

$$\gamma_{mn} = R_m + R_n - \|X_m - X_n\| \quad \text{Eq. 8.8}$$

$$R_{mn} = \left[\frac{1}{R_m} + \frac{1}{R_n} \right]^{-1} \quad \text{Eq. 8.9}$$

where H_{mn} is contact conductance, which defines the ability of two conforming particles to transmit heat across their mutual interface. a_{mn} is the Hertzian contact area, k_{mn} is the arithmetic mean of the thermal conductivities of two particles in contact, R_m and R_n are particle radii and overlap γ_{mn} that occurs along the contact line.

There are six mechanisms to describe heat transfer between particles:

(1) thermal conduction through the solid;

(2) thermal conduction through the contact area between two particles;

(3) thermal conduction to/from the interstitial fluid;

(4) heat transfer by fluid convection;

(5) radiant heat transfer between the surfaces of particles; and

(6) radiant heat transfer between neighboring voids.

Our work is focused on the first two mechanisms which are expected to dominate when the interstitial medium is stagnant and composed of a material whose thermal conductivity is small compared to that of the particles.[118]

Thermal contact and Hertzian deformation models are integrated to understand the thermomechanical behavior of consolidated granular systems. The model assumes quasi-static equilibrium and quasi-steady heat conduction conditions that are appropriate for many thermally-assisted compaction processes.

For discrete particle-mechanics modeling, first step is forming a packing of particles with the target particle size distribution. Since discrete particle modeling methods require the representation of individual particles in the material, the computational efficiency is constrained by the number of particles in the system [116].

In the recent study by Yohannes et al. indicated of removing the fine particles does not affect the compaction profile and tensile strength of the compacts [129]. Figure 5.2 shows the compaction profiles of lactose samples with different particle size distribution, these four samples (all particles, d > 75 μm, d > 106 μm, and d > 150 μm) have very similar compaction profiles indicating that the fine particles have little or no effect on the compaction of the samples. Based on their results, we adopt to use particle sizes greater than 100 μm to model the powder compaction, which will significantly reduce the number of particles used in the simulations. The sizes of particles in this simulation study range between 100 and 240 μm for lactose and the total number of particles is about 100,000.

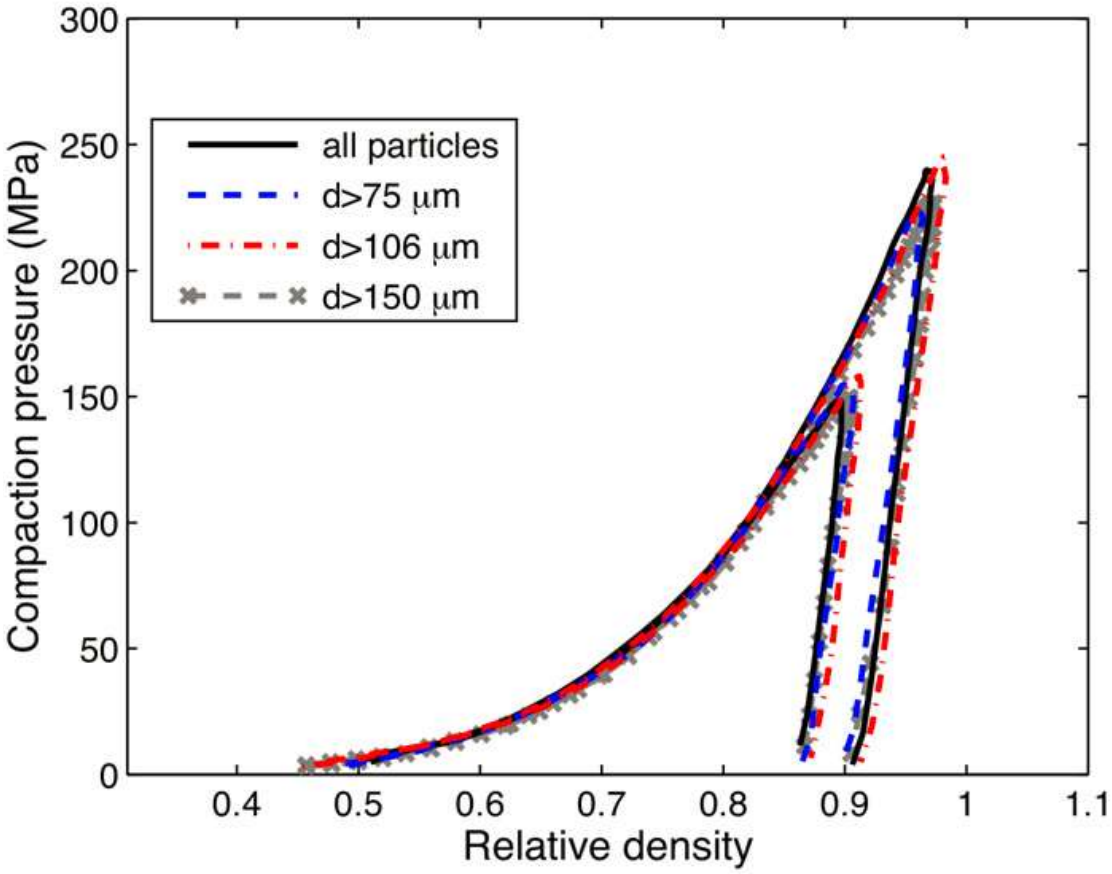

Figure 5.2: Compaction pressure vs. relative density for lactose samples with different particle size distribution, adopted from Yohannes et al. [2016]

These particles are deposited in a cylindrical die using a ballistic gravitational deposition method [130-132]. Only the static equilibrium of individual particles is used as a criteria in the ballistic deposition method [116], while the other factors that may affect packing of granular materials, such as the dynamic forces, friction, and cohesion are ignored. Each particle is allowed to roll down on other particles freely until it locks into a stable configuration. To be in stable static equilibrium in three dimensional systems, each frictionless particle should be in contact with at least three other particles/walls such that motion or rolling in any direction is prohibited due to the contacts with the neighboring

particles. Each particle can also be in equilibrium if it lies on a horizontal plane wall. This ballistic deposition method is much faster than other gravitation deposition methods that consider the dynamic contact forces and integration time steps.

In the simulations, only spherical particles are used, and the inter-particle attractive force is ignored. After the particles are deposited, a compaction pressure is gradually applied through upper and lower punches. The compaction simulation is a strain-controlled simulation, where a small displacement is applied to the two punches. The pressure on the punches is then measured based on the contact forces from the particles. The lactose particles are deposited in a 10 mm-diameter cylindrical die.

Simulation during compaction, unloading, and ejection of tablet, the contact force between the particles is computed based on the deformation and mechanical properties of the particles. The deformation is computed as the overlap between pair of contacting particles. The plastic properties, elastic properties, and bonding parameters of the particles are also used to compute the force (elastic contact mechanics is defined in Appendix A). A pair of contacting particles can be in a loading mode (where the particles are in contact for the first time), or unloading mode (where the contact force on a pair of contacting particles is decreasing), or reloading mode (where a previously contacting particles are overlapping again). During loading mode, the particles are restricted to follow a power-law plasticity model.

$$\sigma = k\epsilon^{1/\mathrm{m}} \qquad \text{Eq. 8.10}$$

where σ and ϵ are stress and strain of the particles, k and m are particle plastic parameters, respectively.

The contact force (P) between two particles is computed as:

$$P = k_{plastic}\, a^{2+1/\mathrm{m}} \qquad \text{Eq. 8.11}$$

where a is the radius of the contact area between the pair of contacting particles,

$$a = \sqrt{2\, c_2 \frac{\gamma}{\frac{1}{R_1}+\frac{1}{R_2}}} \qquad \text{Eq. 8.12}$$

where γ is the overlap between two contacting particles, and m is the average plastic parameter, $\mathrm{m} = (\mathrm{m}_1 + \mathrm{m}_2)/2$, ($\mathrm{m}_1$ and m_2 refer to the pair of contacting particles). The parameter $k_{plastic}$ is given as

$$k_{plastic} = K\pi\left(\frac{1}{{k_1}^{\mathrm{m}}} + \frac{1}{{k_2}^{\mathrm{m}}}\right)^{-\frac{1}{\mathrm{m}}} \left(\frac{1}{R_1} + \frac{1}{R_2}\right)^{\frac{1}{2\mathrm{m}}-1} (2c_2)^{1+\frac{1}{2\mathrm{m}}} \qquad \text{Eq. 8.13}$$

where R is the radius of the particles, $K = 3 \times 6^{-\frac{1}{\mathrm{m}}}$, $c_2 = 1.43 \exp\left(-\frac{0.97}{\mathrm{m}}\right)$.

During the unloading of the contact force, P is computed as,

$$P = \frac{2k_{plastic}}{\pi} {a_p}^{2+\frac{1}{\mathrm{m}}} [\arcsin(\frac{a}{a_p} - (\frac{a}{a_p})\sqrt{1-(\frac{a}{a_p})^2}\ ] - \sqrt{8\pi\omega E_m}\ {a_p}^{\frac{3}{2}} (\frac{a}{a_p})^{\frac{3}{2}} \qquad \text{Eq. 8.14}$$

where a_p is the radius of the contact area at the maximum P during the loading phase, ω is the bonding energy per area, and E_m is the effective Young's modulus,

$$E_m = (\frac{1-{\nu_1}^2}{E_1} + \frac{1-{\nu_2}^2}{E_2})^{-1} \qquad \text{Eq 8.15}$$

where E is the Young's modulus, ν is the Poisson's ratio.

Adopting from Yohannes's [116] study, the material properties of the particles in the simulation were calibrated by comparing the compressibility of the powders of the simulations to that of experiments (compaction pressure vs. relative density curve). In the tablet compaction experiments as described in chapter 3.3, a tablet press (Presster, Metropolitan Computing Corporation of East Hanover, NJ) installed with a 10 mm-diameter flat face round tooling was used to compact the powders. The plastic parameters play a significant role compared to the elastic and bonding parameters during the application of the compaction pressure. Therefore, the plastic parameters k and m are calibrated using the compaction pressure vs. relative density curve during the application of the compaction pressure. Figure 5.3 shows the comparison of several simulation results with an experimental result. Several combinations of the plastic parameters k and m were

tested in order to select the appropriate values of the plastic parameters. The tested values range from 0.15 to 3.75 GPa for k and from 1.0 to 4.0 for m. As shown in Figure 5.3, when increasing k and m, will increase the compaction pressure for a given relative density. The best fitting plastic parameters are $k = 3.75\ GPa$ and m = 1.0 for lactose based on the lowest least mean square values. After the parameters k and m were selected, the effective Young's modulus (E_m) and the bonding energy (ω) can be calibrated using the compaction vs. relative density curve during the unloading of the compaction pressure. Several combinations of E_m and ω were tested. The best fitting values are E_m = 10 GPa and ω= 1100 J/m^2 for lactose as shown in Figure 5.4.

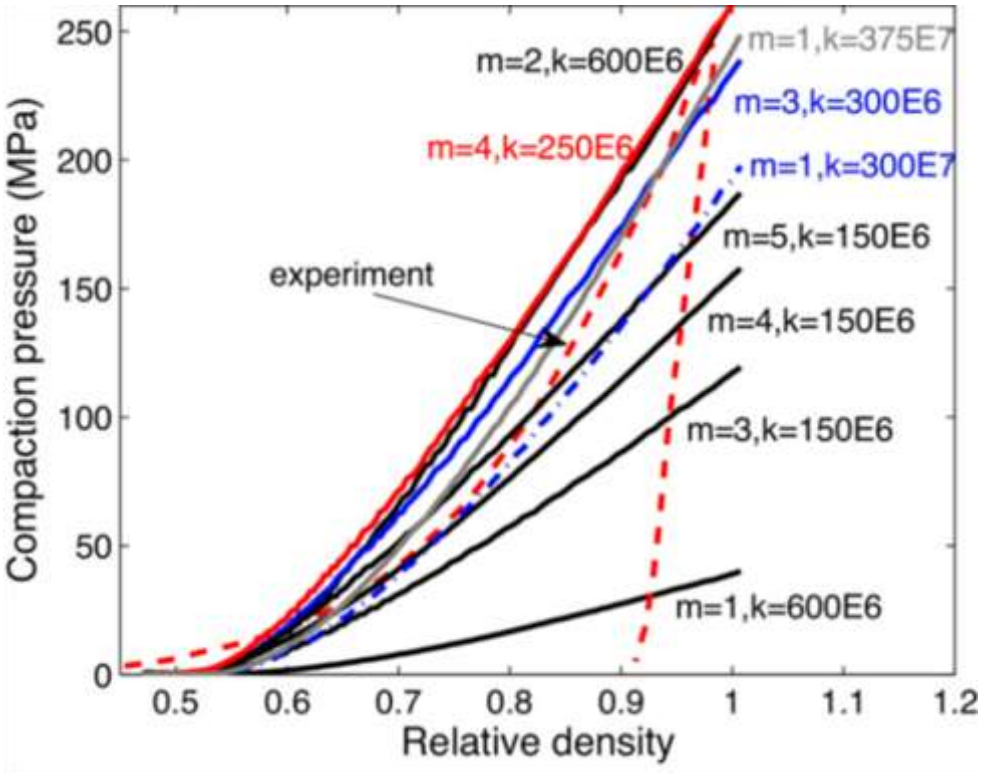

Figure 5.3: Calibration of plastic parameter for lactose. The best fitting values are k = 3.75 GPa and m = 1.0, adopted from Yohannes et al. [2016]

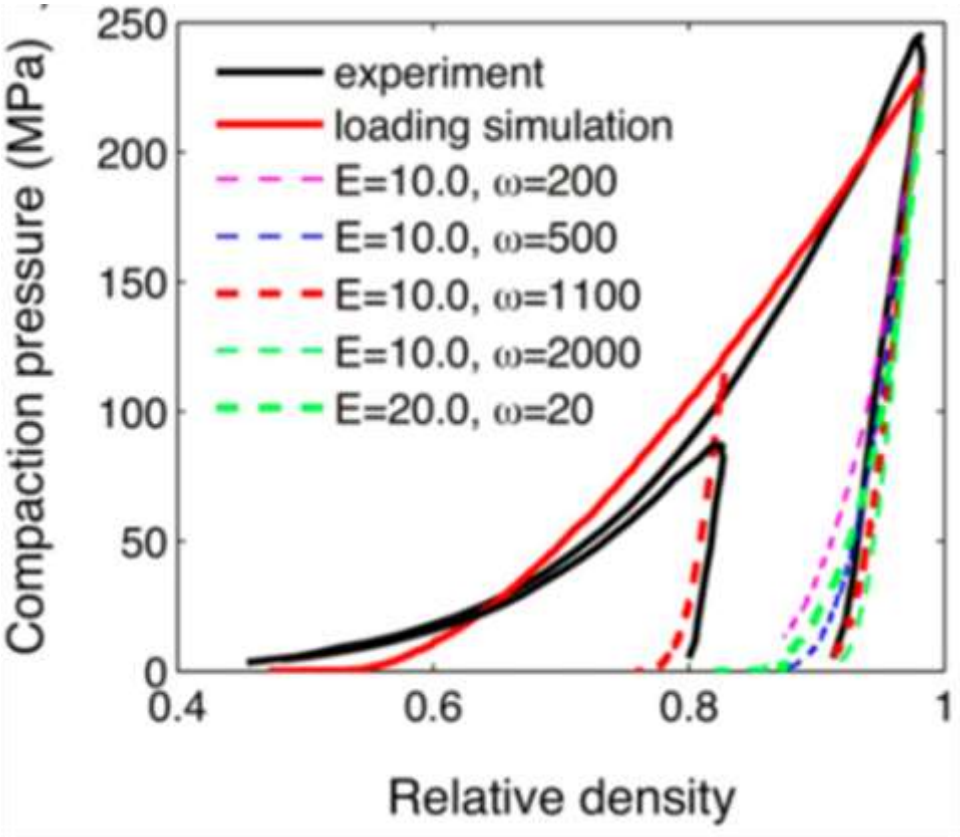

Figure 5.4: The best fitting values are E_m = 10 GPa and ω= 1100 J/m^2 for lactose, adopted from Yohannes et al. [2016]

5.3 Compare Discrete Particle-Mechanics Simulation Results and Infrared Thermal Imaging Experimental Results

5.3.1 Three-dimensional Discrete Particle-Mechanics Simulation Result of Tablet Temperature

The discrete particle-mechanics simulations are run on Xeon(R) X5650 @ 2.67GHz processor with 12 cores using the 3D numerical compaction of granular materials developed by Yohannes et al.[116]

The simulations are tested in combination of different kp/ka ratios (kp is particle thermal conductivity, ka is air thermal conductivity) and several different values of particle thermal conductivity, $k_{p,}$ are applied in the simulations.

Figure 5.5 is an example of simulation of a 30° pie shape three-dimensional lactose 10 mm diameter tablet temperature. In order to compare with the infrared experimental results presented in chapter 4, the temperature information of each individual particle in the simulation is extracted according to their location as indicated in Figure 5.5. Where we determine particles located within a region as follows: particles located within r = 0.1 R region is defined as $\pm$ 0.025 R of 0.1 R (i.e. 0.075 R to 0.125 R), the similar as to r = 0.3 R region (i.e. 0.275 R to 0.325 R), r = 0.5 R region (i.e. 0.475 R to 0.525 R), r = 0.7 R region (i.e. 0.675 R to 0.725 R), r = 0.9 R region (i.e. 0.875 R to 0.925 R) and r = R region (i.e. 0.975 R to R).

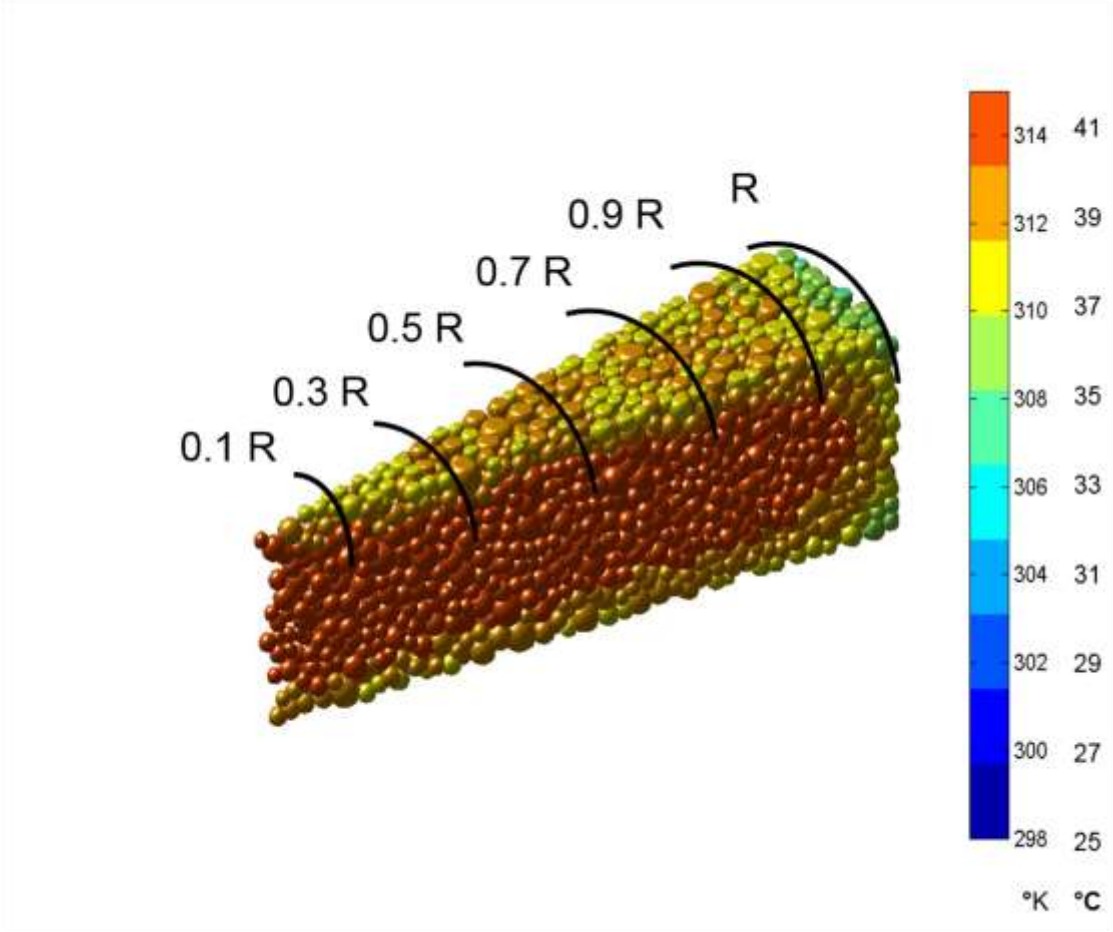

Figure 5.5: Example of temperature simulation results of a 30° pie shape three-dimensional 10 mm diameter lactose tablet.

The following is a general procedure of the temperature information extraction process after compaction simulation of the 30° pie shape three-dimensional 10 mm diameter lactose tablet:

First, we extract temperature information from simulation with selecting one particle located within each region of r = 0.1 R, 0.5 R, 0.7 R, 0.9 R, and R. And then use the extracted temperature to calculate tablet's rate of cooling in regular regime as described in

chapter 4.2, the result is shown in Figure 5.6 for tracking temperature of one particle in each region.

Second, by selecting multiple particles located within each region of r = 0.1 R, 0.3 R, 0.5 R, 0.7 R, 0.9 R, and R as described above. And then use the extracted average temperature of multiple particles in each region to calculate tablet's rate of cooling in regular regime as described in chapter 4.2, the result is shown in Figure 5.7 for tracking temperature of multiple particles in each region.

We found similarity both in tracking temperature of one particle in each region (Figure 5.6) and in tracking temperature of multiple particles in each region (Figure 5.7) of the calculated tablet rate of cooling from extracted temperature by simulations as shown.

But in the 30° pie shape three-dimensional 10 mm diameter lactose tablet simulations, while compiling the data we observe that in regions such as r = 0.1 R and r = 0.3 R regions, the neighboring/adjacent particles in these two regions are considerably less than the other regions at r ≥ 0.5 R as shown in Figure 5.5 due to the simulation is only run on the 30° three-dimensional pie. And the calculated tablet rate of cooling (m_1) from extracted temperature by simulation in these two regions (i.e. r = 0.1 R and r = 0.3 R) might be slightly different from r ≥ 0.5 R as shown in Figure 5.7.

So, it is determined that we consider using the calculated tablet rate of cooling from simulations of particles located at regions at r ≥ 0.5 R for more consistent results of tablet

rate of cooling, m_1 , in the 30° pie shape three-dimensional 10 mm diameter lactose tablet simulations as displayed in Figure 5.7.

The simulation results shown in Figure 5.8 is an example of a 30 ° pie shape three-dimensional 10 mm diameter lactose tablet temperature changes with the progression of time step after tablet's ejection on die table on the tablet press after compaction. The simulation data shows that we are able to track each particle's temperature for each time step. For example, we can track an individual particle located around r = 0.5 R, during the simulation as time step progress from time step A to D, its temperature changes from 34.9 °C to 32.7 °C (at time step B), to 31.4 °C (at time step C), to 30.3 °C (at time step D). Similar observations for tracking individual particle located at r = 0.7 R, r= 0.9 R, and r = R respectively as shown in Figure 5.8.

It is also observed that at time step A there is a temperature gradient of 4.6 °C between the particle at r = 0.5 R and the particle at r = R. And similar at time step B, the temperature gradient is 4.2 °C between the particle at r = 0.5 R and the particle at r = R. At time step C, the temperature gradient is 3.7 °C between the particle at r = 0.5 R and the particle at r = R. At time step D, the temperature gradient is 3.3 °C between the particle at r = 0.5 R and the particle at r = R.

As shown in Figure 5.9 is simulation results of a 30° pie shape three-dimensional 10 mm diameter lactose tablet temperature changes with the progression of time step. The advantage of discrete particle-mechanics simulation is that we are capable of tracking each

particle's temperature at any location from center to edge of tablet at each time step. The evolution of each particle's temperature can be tracked is the key feature of discrete particle-mechanics simulation that will enable us to understand the interactions between individual particles and the heterogeneity in the bulk during tablet compaction process.

Simulation results of temperature evolution of compacting a three-dimensional 3 mm diameter size lactose tablet, the temperature changes with the progression of time step is presented in Figures 5.10 and 5.11. Similarly, as we described in Figure 5.8 of the 30° pie shape three-dimensional 10 mm diameter lactose tablet temperature changes with the progression of time step, we can track each individual particle located from r = 0 (i.e. center of tablet) to r = R (i.e. edge of tablet) with the progression of time steps.

Comparison of discrete particle-mechanics heat transfer simulations and infrared thermal imaging experimental results in regular regime of tablet cooling is discussed in detail in chapter 5.3.2 and 5.3.3.

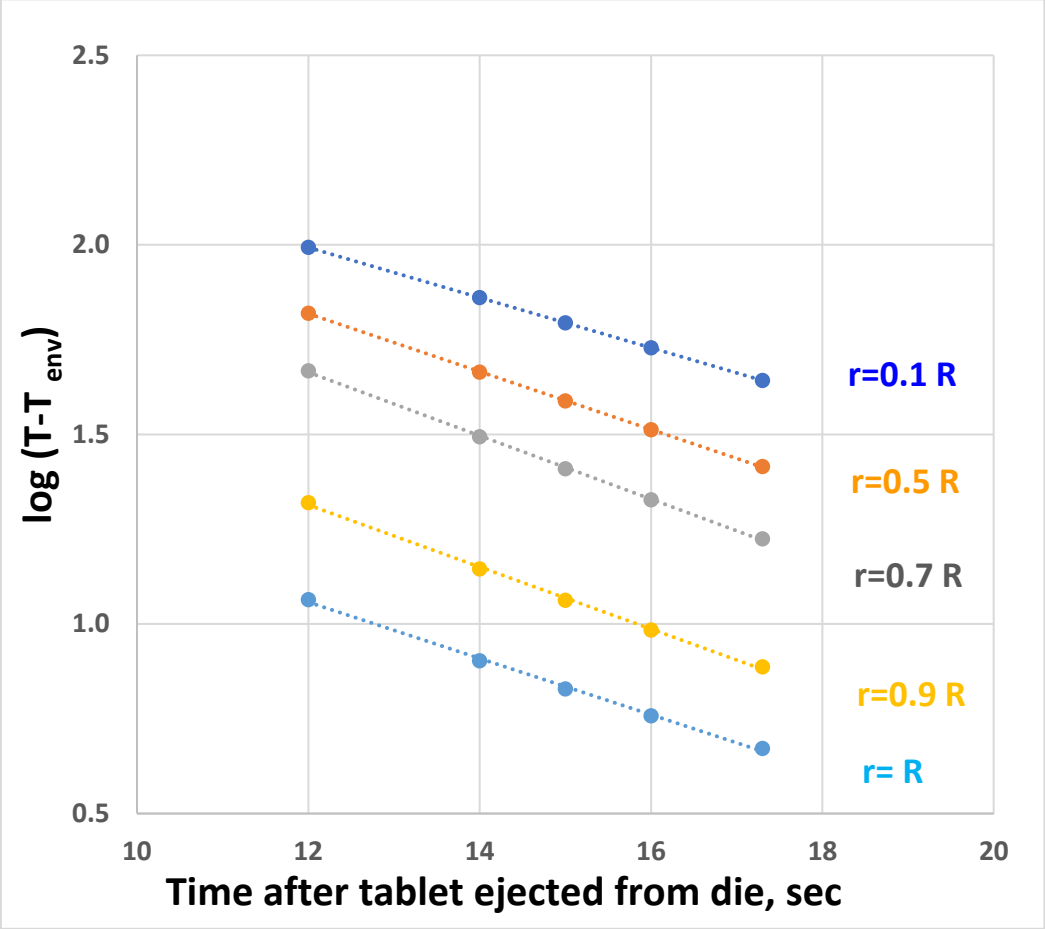

Figure 5.6: Example of simulation tested with kp = 0.03 W/m °K, temperature information of one particle in each region is extracted to calculate tablet's rate of cooling

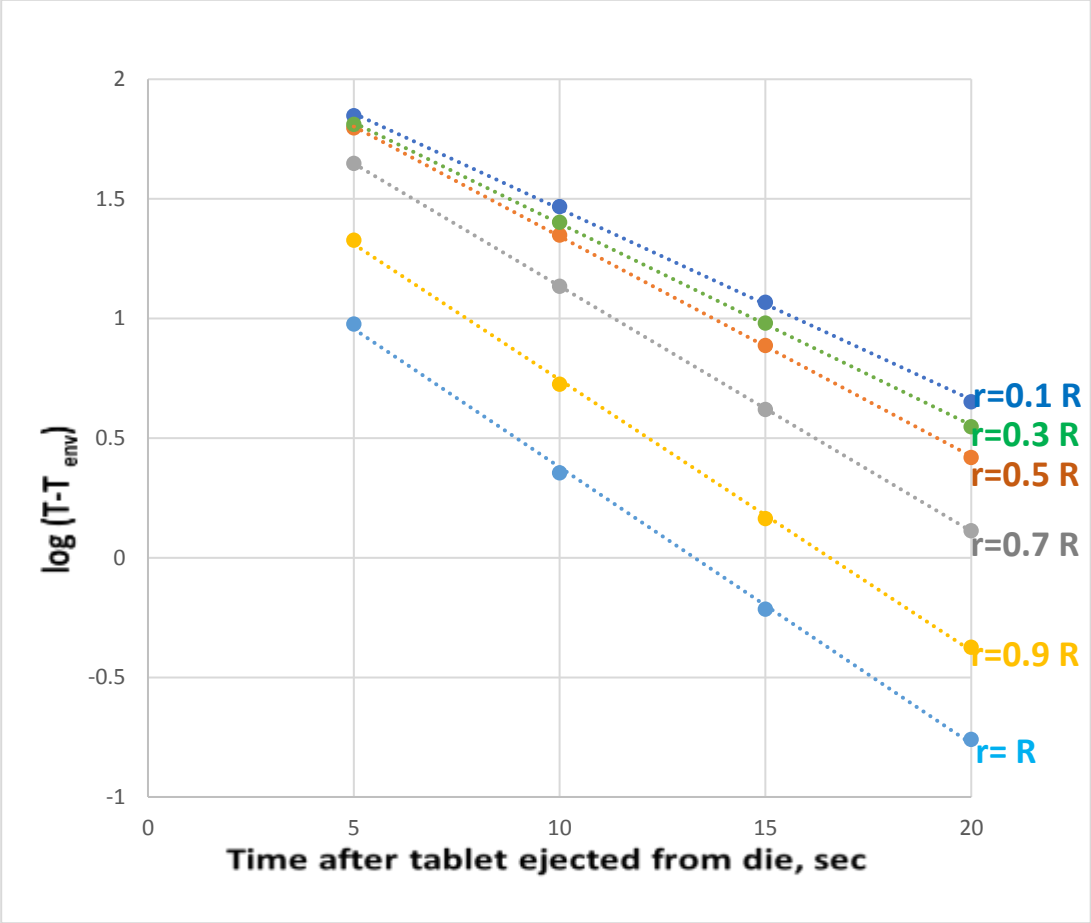

Figure 5.7: Example of simulation tested with kp = 0.03 W/m °K, temperature information of multiple particles in each region are extracted to calculate tablet's rate of cooling, number of particles in each region are as followed: r = 0.1 R (2 particles), r = 0.3 R (3 particles), r = 0.5 R (14 particles), r = 0.7 R (10 particles), r = 0.9 R (12 particles), and r = R (9 particles)

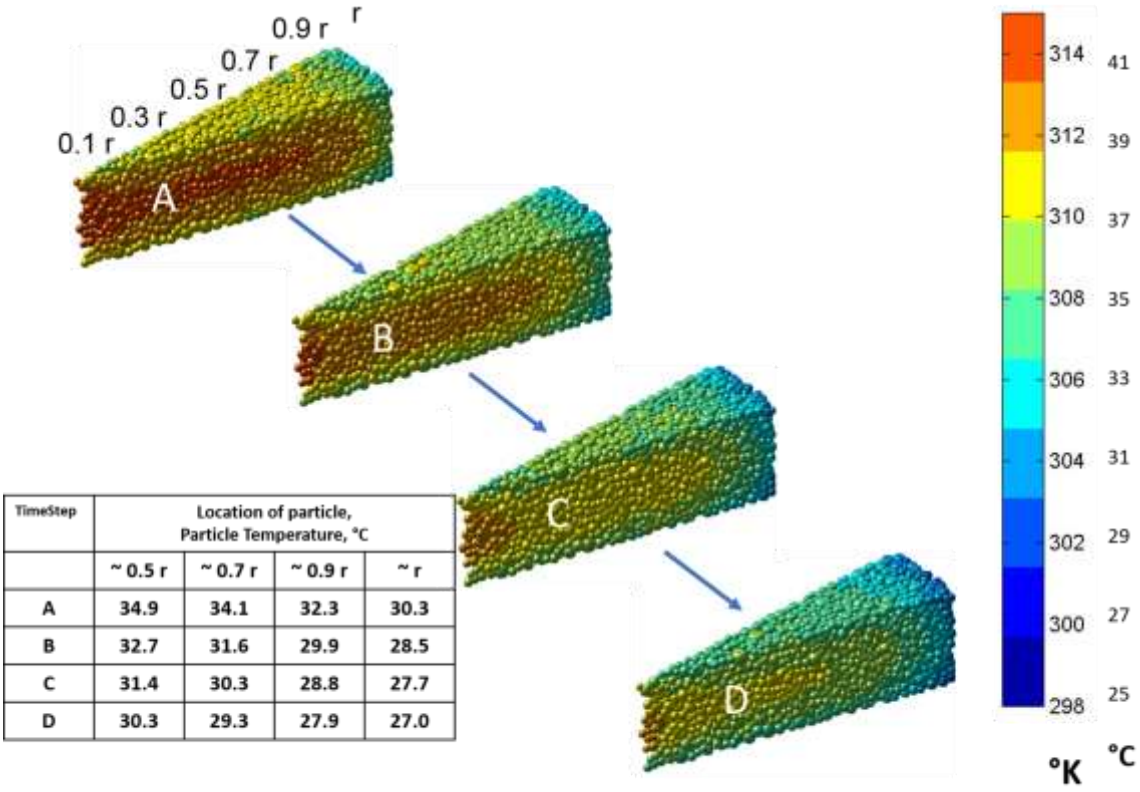

TimeStep	Location of particle, Particle Temperature, °C			
	~ 0.5 r	~ 0.7 r	~ 0.9 r	~ r
A	34.9	34.1	32.3	30.3
B	32.7	31.6	29.9	28.5
C	31.4	30.3	28.8	27.7
D	30.3	29.3	27.9	27.0

Figure 5.8: Example of temperature simulation results of a 30° pie shape three-dimensional 10 mm diameter lactose tablet, particle temperature evolution according to their location at r = 0.5 R, 0.7 R, 0.9 R, and R as time step progress from A to D.

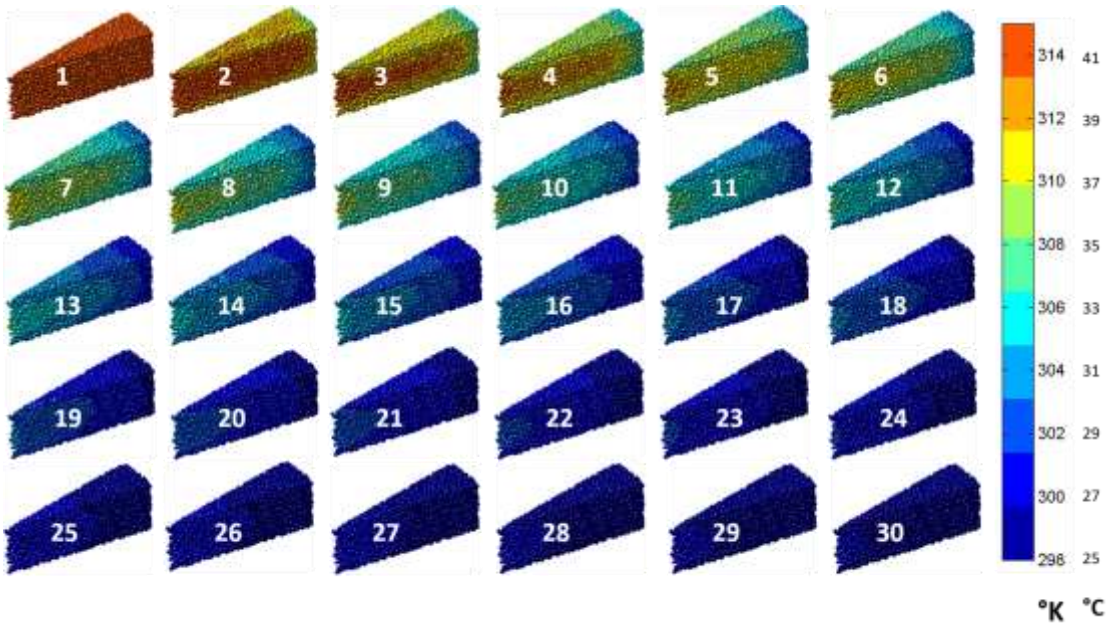

Figure 5.9: Example of simulation results of a 30° pie shape three-dimensional 10 mm diameter lactose tablet temperature changes with the progression of time step (from time step 1 to 30) after tablet's ejection on die table.

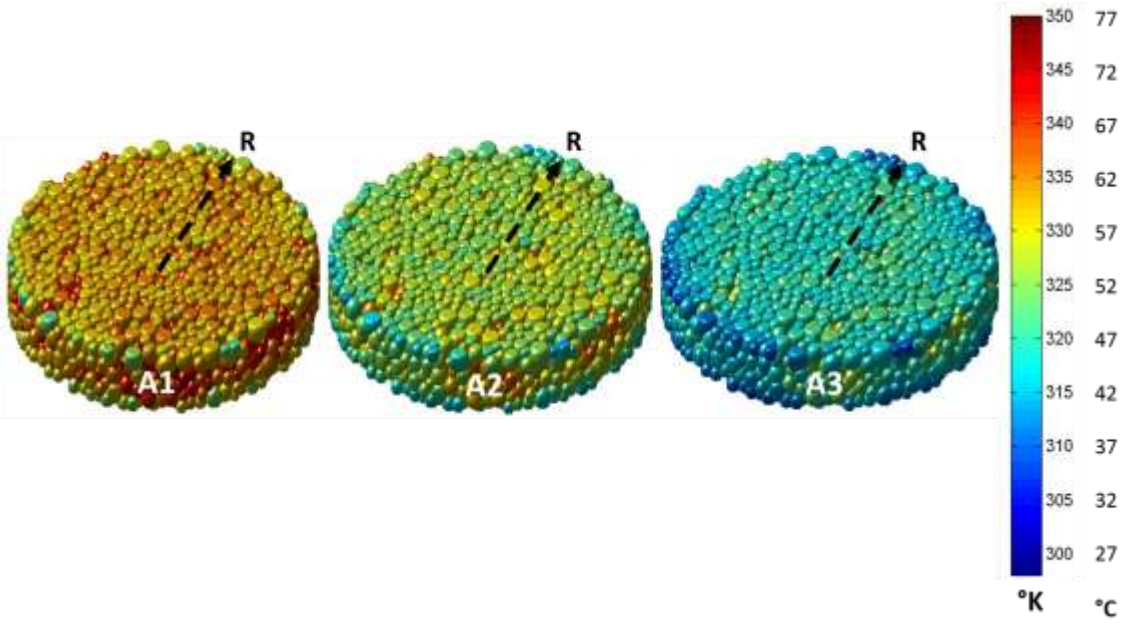

Figure 5.10: Example of simulation results of a three-dimensional 3 mm diameter lactose tablet temperature changes with the progression of time step from time step A1 to A2, then A2 to A3 after tablet's ejection on die table.

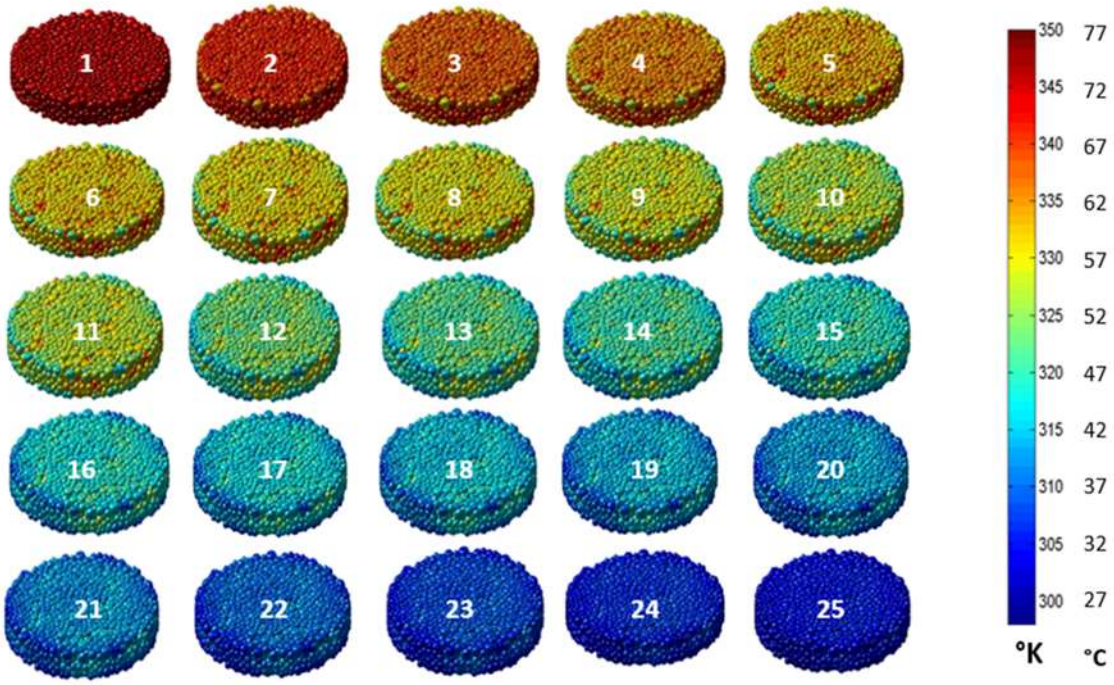

Figure 5.11: Example of simulation results of a three-dimensional 3 mm diameter lactose tablet temperature changes with the progression of time step (from time step 1 to 25) after tablet's ejection on die table.

5.3.2 Compare Tablet Temperature by Infrared Thermal Imaging Experimental Results and by Discrete Particle-Mechanics Simulation Results

Figure 5.12 (a) illustrates experimental results measured by infrared thermal camera of the cooling process of lactose tablet's upper surface temperature with the progression of time (15 sec to 50 sec) from left edge to right edge of tablet compacted at 24 ± 0.5 kN. It can be seen that the highest temperature exhibits at the center of the upper surface of the tablet. Figure 5.12 (b) shows the discrete particle-mechanics simulation results that indicated each particle's temperature profile as time step progresses. Compare Figures 5.12 (a) and 5.12 (b), it shows good agreement between infrared thermal imaging experimental results and discrete particle-mechanics simulation results.

The result from discrete particle-mechanics simulation indicates that this computational modeling is well capable of simulating heat transfer process of tablet compaction at individual particle level and ultimately can simulate the macroscopic mechanical [116] and thermal properties of the whole tablet.

It is clear that the highest upper surface temperature was observed at the center of the flat-face tablet, and the upper surface temperature monotonically decreases towards the edge, the temperature at the edge of tablet is generally lower than the temperature in the center of tablet.

The heat generated during compaction is the result of dissipation due to irreversible process. Tablet's thermal signature collected by infrared thermal camera can provide valuable information to study the contact mechanics between adjacent particle surfaces and the pattern when these powder particles rearrange under compaction.

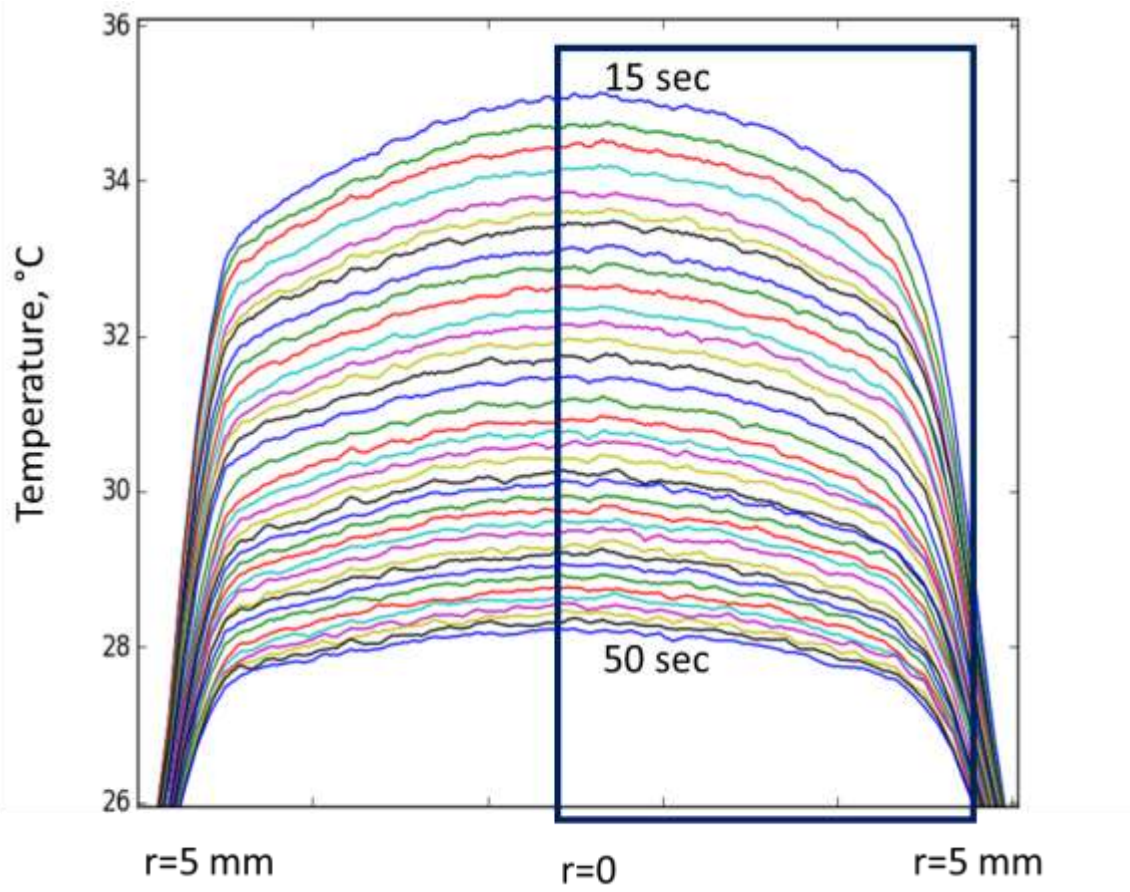

Figure 5.12 (a): Infrared experimental results of the cooling process of lactose tablet's upper surface temperature with the progression of time (15 sec to 50 sec) from left edge to right edge of tablet compacted at 24 $\pm$ 0.5 kN

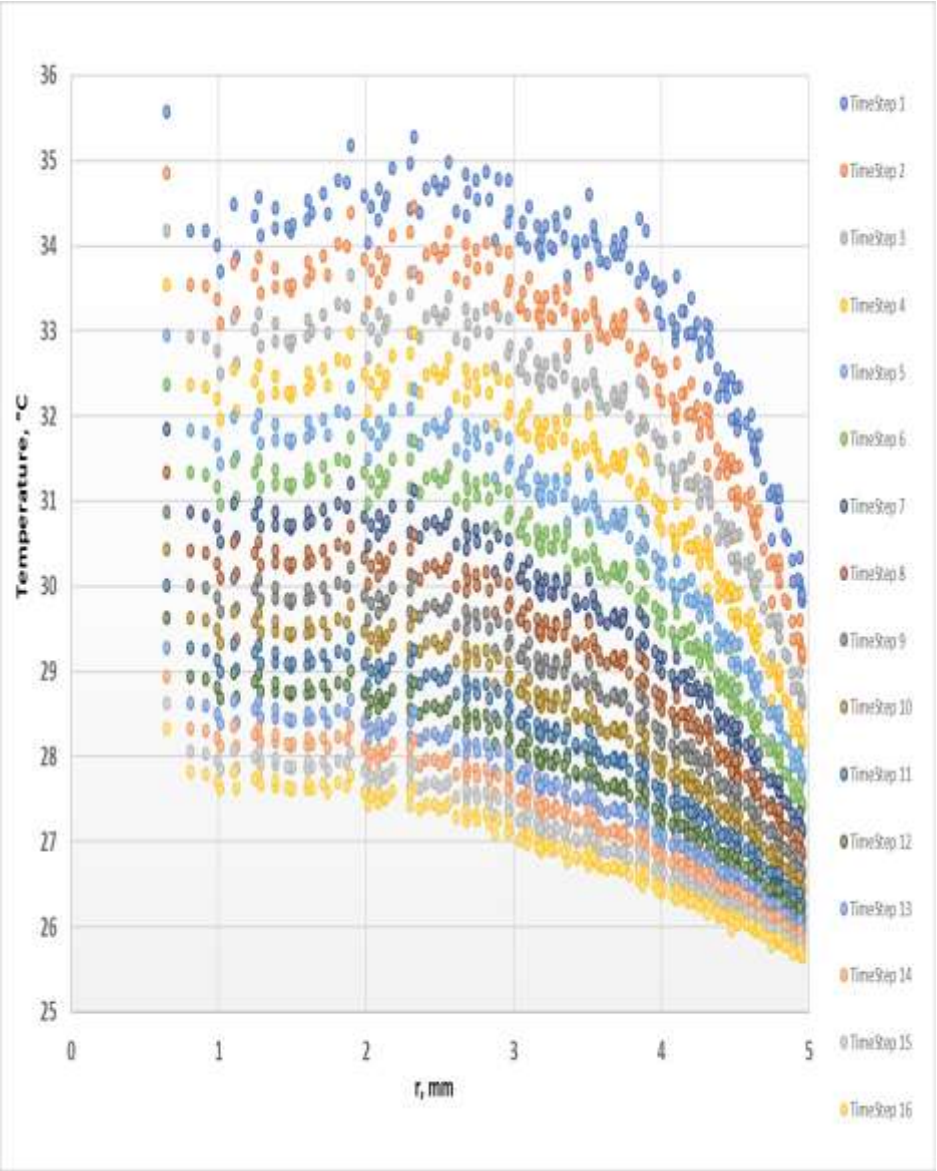

Figure 5.12 (b): Discrete particle-mechanics simulation results of the cooling process of lactose tablet's upper surface temperature from center of tablet to edge of tablet with the progression of time step.

5.3.3 Discrete Particle-Mechanics Simulation Results of Tablet Temperature at Regular Regime

Several different values of particle thermal conductivity, k_p, are applied in the discrete particle-mechanics simulations for heat transfer of lactose tablet. In Figure 5.13 (a) shows a series of curves for prediction of the tablet's rate of cooling when the location of the particle located from the tablet center towards the tablet edge (i.e. increases of r) in the simulations.

$T^*(r,t)$ is defined as following:

$$T^*(r,t) = \frac{T(r,t) - T_{env}}{T(r=0,t=0) - T_{env}}$$

Where $T(r=0,t=0)$ is the particle temperature at location r = 0, time t = 0, $T(r,t)$ is the particle temperature at location r and time t, and T_{env} is the environment temperature surrounding the tablet.

Figure 5.13 (b), 5.13 (c), 5.13 (d) and 5.13 (e) show the discrete particle-mechanics simulation results of tested heat transfer for different values of particle thermal conductivity, k_p, at 3, 0.3, 0.06, and 0.04 W/m °K respectively, and the calculated value of tablet's rate of cooling, m_1, in regular regime as described in chapter 4.2.

In Figure 5.13 (f) illustrates the infrared experimental results of tablet's rate of cooling, m_1, in regular regime of lactose tablet compressed at 24 ± 0.5 kN. Compare Figure 5.13 (e) and 5.13 (f), it indicates there is broad agreement of tablet's rate of cooling, m_1, between infrared experimental results and discrete particle-mechanics simulation results. This is another indication that we observed in similarity of results between infrared thermal imaging experimental results and discrete particle-mechanics simulations of tablet temperature evolution in chapter 5.3.2.

As we combine the similar m_1 value of the infrared experimental result ($m_1 = 0.0301$) from Figure 5.13 (f) and the simulation result ($m_1 = 0.0298$) of Figures 5.13 (e) into a same plot as shown in Figure 5.14.

Compare the temperature results in Figure 5.14 at r = 0.5 R, r =0.7 R, and r = 0.9 R that the simulation results come very close to match with infrared thermal imaging experimental results which indicate that the discrete particle-mechanics modeling is suitable to be a computational tool for simulating the heat transfer of particulate systems in pharmaceutical tablet manufacturing, particularly the interactions between individual particles and the heterogeneity in the bulk.

A relationship between m_1 and k_p as shown in Figure 5.15 is developed base on the simulation results from tested heat transfer of different values of particle thermal conductivity, k_p at 3, 0.3, 0.06, and 0.04 W/m °K in Figures 5.13 (b), (c), (d), and (e)

respectively and the infrared thermal imaging experimental results of tablet compaction from Figure 5.13 (f) as followed:

$$m_1 = 0.0213\left[\log(k_p)\right] + 0.0993 \qquad \text{Eq. 9}$$

The model in Eq. 9 is presented toward conducting computational modeling of particulate system for heat transfer simulation during consolidation process. For a given information of tablet's rate of cooling, m_1 , measured by a non-contact infrared thermal camera as an in-line PAT tool after tablet compaction, there is a corresponding particle thermal conductivity, k_p , for researcher to choose as a starting point for conducting computational simulation for particulate system on heat transfer during consolidation process.

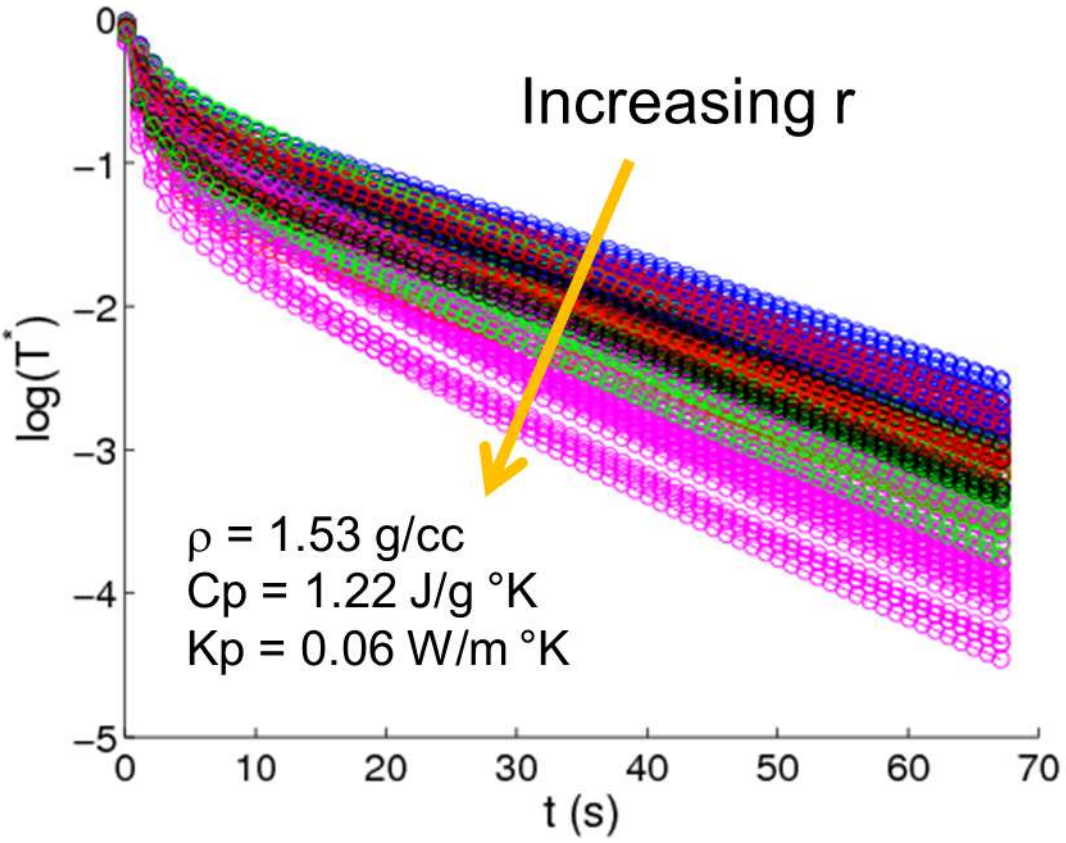

Figure 5.13 (a): Prediction curves by discrete particle-mechanics simulation of the tablet's rate of cooling when evaluating the extracted temperature of the particle as the location of the particle located from the tablet center towards the tablet edge (i.e. increases of r from r= 0 to r=R)

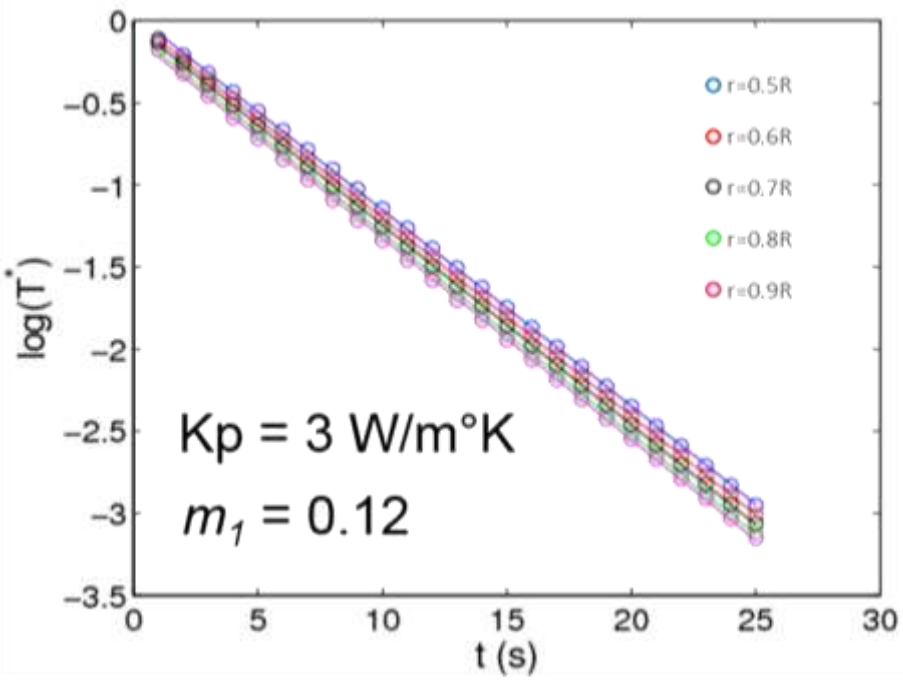

Figure 5.13 (b): Discrete simulation with k_p = 3 W/m °K applied, log (T*) vs time (i.e. slope, m_1) after tablet ejected from die, particle temperature at location of r = 0.5 R, 0.6 R, 0.7 R, 0.8 R, and 0.9 R of tablet

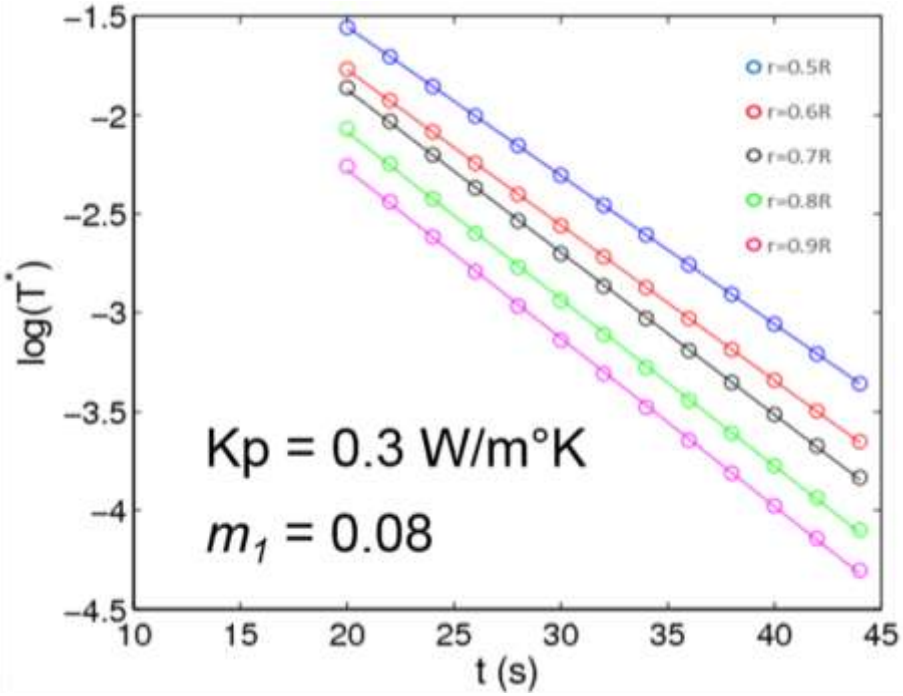

Figure 5.13 (c): Discrete simulation with k_p = 0.3 W/m °K applied, log (T*) vs time (i.e. slope, m_1) after tablet ejected from die, particle temperature at location of r = 0.5 R, 0.6 R, 0.7 R, 0.8 R, and 0.9 R of tablet

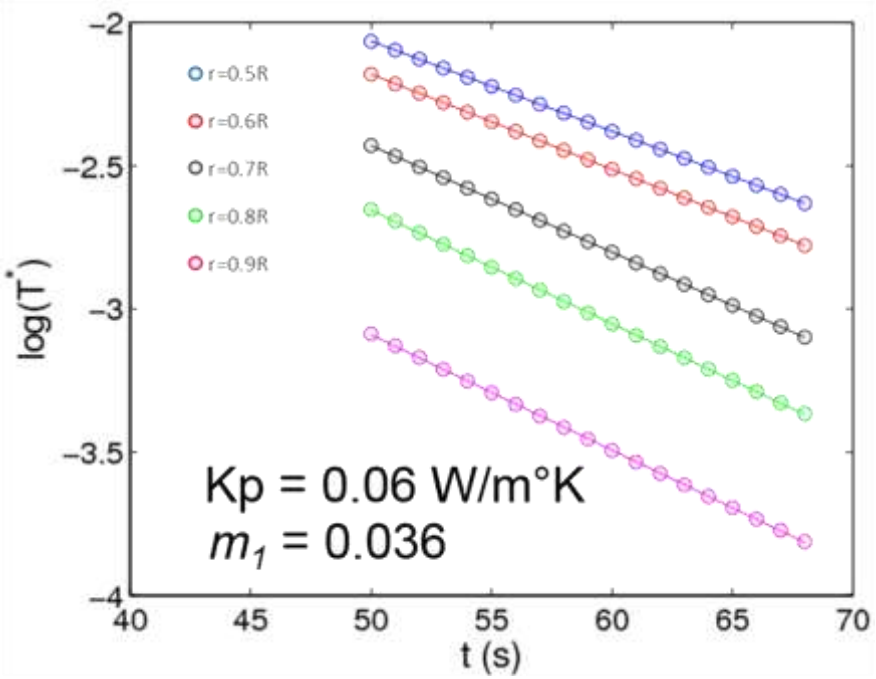

Figure 5.13 (d): Discrete simulation with k_p = 0.06 W/m °K applied, log (T*) vs time (i.e. slope, m_1) after tablet ejected from die, particle temperature at location of r = 0.5 R, 0.6 R, 0.7 R, 0.8 R, and 0.9 R of tablet

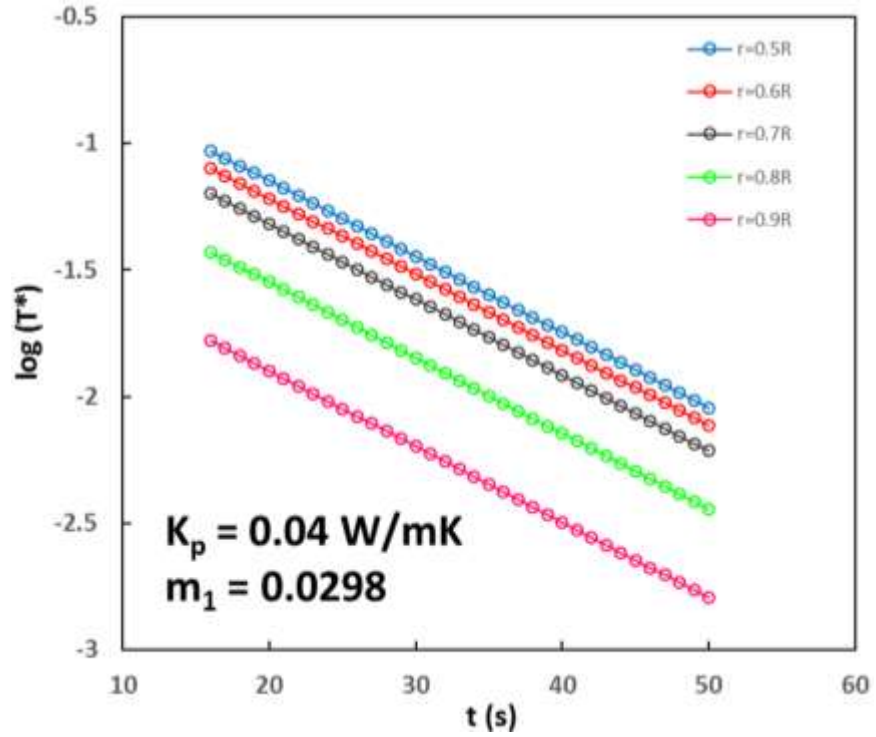

Figure 5.13 (e): Discrete simulation with k_p = 0.04 W/m °K applied, log (T*) vs time (i.e. slope, m_1) after tablet ejected from die, particle temperature at location of r = 0.5 R, 0.6 R, 0.7 R, 0.8 R, and 0.9 R of tablet

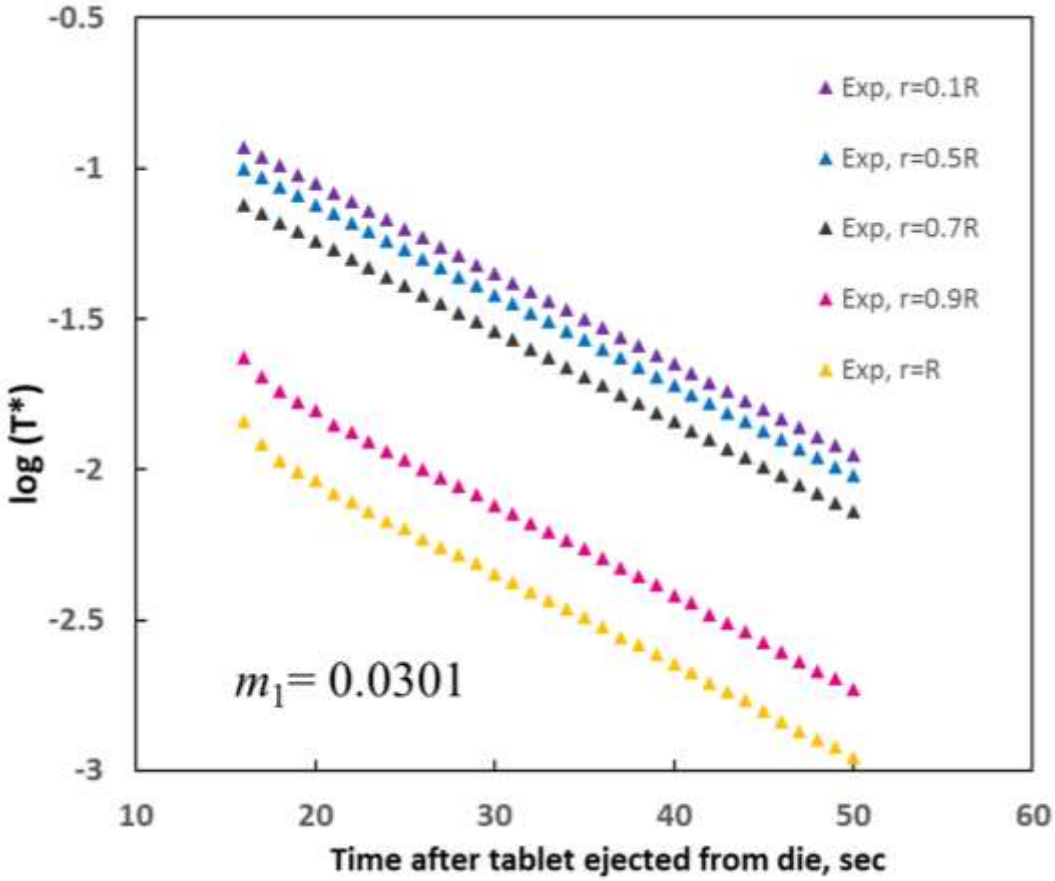

Figure 5.13 (f): log (T*) vs time (i.e. slope, m_1) after tablet ejected from die at location of r = 0.1 R, 0.5 R, 0.7 R, 0.9 R, and R of lactose tablet compressed at 24 ± 0.5 kN

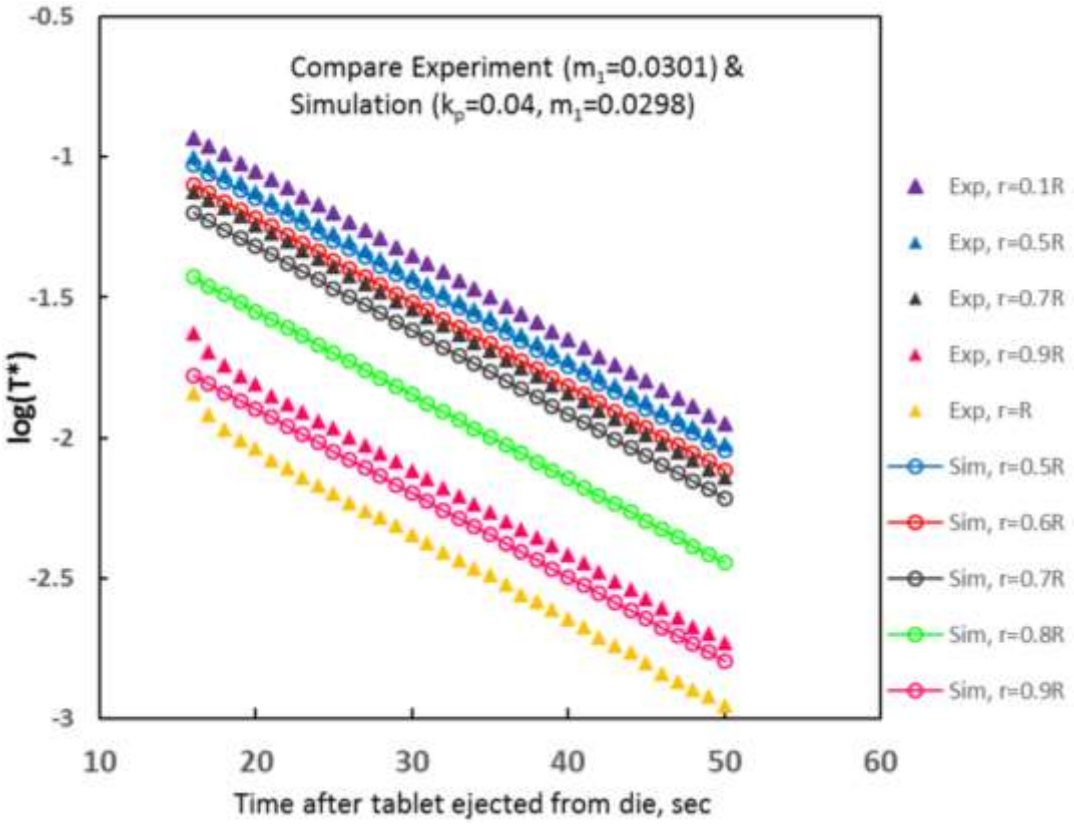

Figure 5.14: Compare infrared experimental result and simulation result with similar m_1

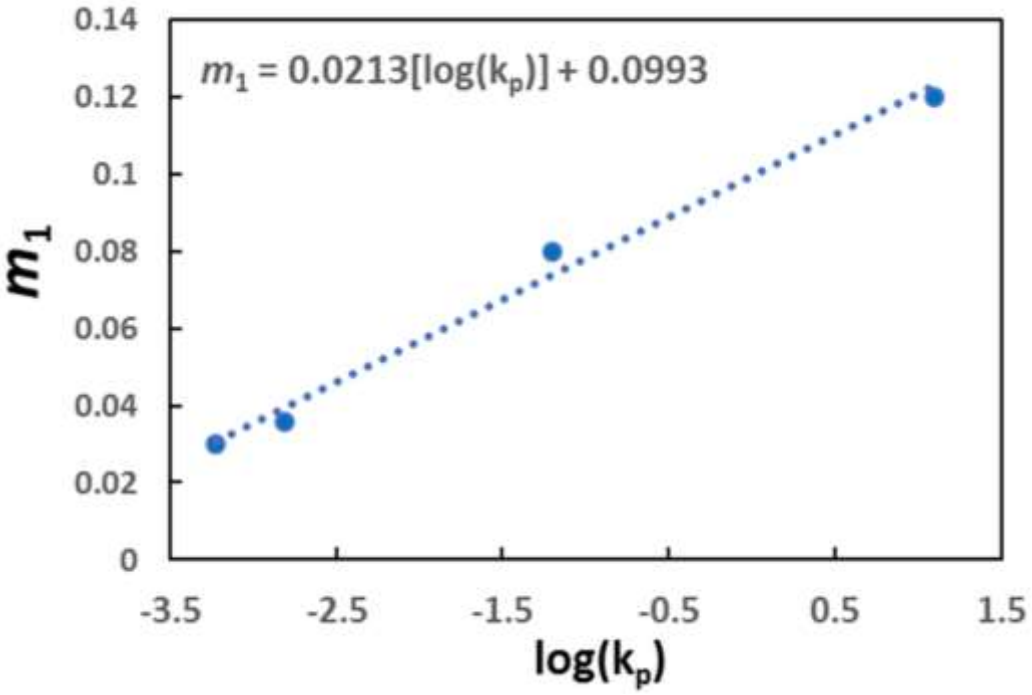

Figure 5.15: Relationship between tablet rate of cooling, m_1 , and particle thermal conductivity, k_p , for conducting computational simulation

5.4 Conclusion

We explore the possibility of using the computational tools based on discrete particle-mechanics modeling to describe the formation of networks during the consolidation process of pharmaceutical tablet compaction. These heterogeneous networks are subsequently used to simulate the heat transfer process after tablet's ejection on tablet press. We demonstrate the computational modeling of heat transfer of tablet compaction match well with experimental results measured by a non-destructive, non-contact and non-invasive infrared thermal imaging system in terms of the tablet's rate of cooling. This infrared thermal imaging system can be a good candidate to act as an in-line PAT tool for oral solid dosage pharmaceutical manufacturing.

The advantage of using discrete particle-mechanics simulation for pharmaceutical tablet compaction process is that this tool enables us in tracking each particle's temperature at any location from center to edge of tablet at each time step during tablet compaction and ultimately, we can simulate the macroscopic mechanical and thermal properties of the whole tablet.

Utilization of computational modeling with the aspect of heat transfer in particulate systems during pharmaceutical powder consolidation process give us the privileges to understand and investigate the compaction process in detail, such as the evolution of microstructure, the interactions between individual particles and the heterogeneity in the bulk which is essential for the advancement of pharmaceutical research and development.

Chapter 6

Conclusions and Future Work

6.1 Conclusions

6.1.1 Infrared Thermography as a Non-destructive and Non-contact PAT Technique

While utilizing infrared (IR) thermal camera in studying the transient temperature of pharmaceutical tablet compaction process, we discover the immense potential of using infrared thermography as a non-destructive, non-contact, and non-invasive PAT technique for monitoring the tablet production with pharmaceutical powder subjected to different process shear conditions. IR measurement of tablet's rate of cooling, m_1, at *regular regime* was found to be sensitive to the relative density and the level of process shear.

With the success of using infrared (IR) measurement system on monitoring tablet's detail thermal signature during compaction process, we set a milestone in introducing this technique as a potential candidate of in-line PAT tool for future study in pharmaceutical research and development. Formulation scientist can take the advantages of non-destructive/non-contact/non-invasive nature of infrared thermography to conduct numerous studies without destroying the sample or disturbing the manufacturing process.

The detail tablet temperature profile collected by IR after tablet's ejection from tablet press provides a unique insight of transient temperature changes. With IR measurement, we present a correlation between tablet's rate of cooling at *regular regime* and tablet's tensile strength. A model toward predicting tensile strength is developed that only needs the rate of cooling of tablet at zero porosity, $m_{1,0}$, from the infrared thermal imaging to account for tablet mechanical property variations as we described in Equation 7.

Advantages of using the infrared thermography is that this technique is easy to use and provides a unique thermal signature, $m_{1,0}$, of powder blend's total process shear during formulation process and it is also a suitable candidate to be placed on/at-line as a non-destructive and non-contact PAT tool with instantaneous real-time view of tablet temperature.

6.1.2 Computational Modeling

The computational simulation of heat transfer process of tablet compaction with discrete particle-mechanics approach in this study in conjunction with infrared experimental result is found to be capable of capturing details of particle-level temperature profiles which have not been previously reported.

We demonstrate the computational modeling of pharmaceutical tablet transient temperature during tablet compaction match well with experimental results from infrared measurement.

As Yohannes et al. [116] indicates that discrete particle simulations provide complete information of inter-particle contact, and the evolution of bond formation and breakage can be tracked; similarly in our study of utilizing discrete particle-mechanics simulations for modeling heat transfer process during tablet compaction also provides detail information of tablet transient temperature distribution both in particle-to-particle level and macroscopic level with respect to the progression of time step and the evolution of temperature of each particle can be tracked by each time step.

Coupling infrared thermal imaging result and discrete particle-mechanics simulations of temperature behavior on excipients and powder blends during tablet compaction can provide insight for oral solid dosage pharmaceutical formulation research and development.

Formulation scientist can utilize infrared thermal imaging as a PAT tool for a quick screen with instantaneous real-time view of tablet temperature during early stage of formulation development in selecting suitable ratio of excipients and API blend. A data base of tablet temperature behavior during tablet compaction with discrete particle-mechanics simulations of excipients/APIs can be built to serve as a reference for formulation design in achieving/fulfilling the QbD initiative by FDA for pharmaceutical manufacturing process optimization.

6.2 Future Work

Infrared Thermal Imaging

Infrared thermal imaging has a great potential as a PAT tool in monitoring temperature history of pharmaceutical manufacturing process such as unit operation during powder blend roller compaction or during tablet compression. Infrared thermal imaging can be considered in the future to study the interior temperature distribution and surface roughness of the compacted granular materials. The infrared thermal signature information can also a provide guidance of temperature operating ranges when processing temperature sensitive formulations.

Discrete Particle-Mechanics Simulations

Discrete particle-mechanics simulation sheds light on fundamental issues of heat conduction in particles during tablet compaction. By modeling individual particles within the bulk material, bed heterogeneities are directly included, and temperature distributions are obtained at particle level.

With the advantages of matching well with infrared experimental results, discrete particle-mechanics simulations on tablet temperature will enable pharmaceutical formulation scientists to use this computational tool in the future for complex formulation design in pharmaceutical research and development.

Appendix A

The small-strain elasticity of granular media are determined from contact mechanics considerations [121]. These relations define the deformation of locally spherical, elastic particles that are subject to a compression load. Slight deformation of conforming surfaces results in a flat circle of contact area whose dimensions are formulated through Hertz theory [127].

Collinear contact force for elastic contact of two smooth spherical particles *m* and *n* is defined through Young's moduli, E_m and E_n; Poisson's ratio, $\nu_m$and ν_n; particle radii, R_m and R_n; and overlap γ_{mn} that occurs along the contact line.

$$F_{mn} = \frac{4}{3} E_{mn} (R_{mn})^{\frac{1}{2}} (\gamma_{mn})^{\frac{3}{2}} \qquad \text{Eq. A.1}$$

where

$$E_{mn} = [\frac{1- {\nu_m}^2}{E_m} + \frac{1- {\nu_n}^2}{E_n}]^{-1} \qquad \text{Eq. A.2}$$

$$R_{mn} = [\frac{1}{R_m} + \frac{1}{R_n}]^{-1} \qquad \text{Eq. A.3}$$

$$\gamma_{mn} = R_m + R_n - \|X_m - X_n\| \qquad \text{Eq. A.4}$$

Reference

1. Muzzio, F.J., T. Shinbrot, and B.J. Glasser, *Powder technology in the pharmaceutical industry: the need to catch up fast.* Powder Technology, 2002. **124**(1-2): p. 1-7.
2. Yu, L.X., et al., *Understanding Pharmaceutical Quality by Design.* Aaps Journal, 2014. **16**(4): p. 771-783.
3. Zavaliangos, A., et al., *Temperature evolution during compaction of pharmaceutical powders.* J Pharm Sci, 2008. **97**(8): p. 3291-304.
4. Hoag, S.W. and E.G. Rippie, *Thermodynamic analysis of energy dissipation by pharmaceutical tablets during stress unloading.* J Pharm Sci, 1994. **83**(6): p. 903-8.
5. Michrafy, A., et al., *The effects of ambient temperature on the compaction of pharmaceutical powders.* Proceedings of the Institution of Mechanical Engineers Part E-Journal of Process Mechanical Engineering, 2006. **220**(E1): p. 1-6.
6. Travers, D.N. and M.P. Merriman, *Temperature changes occurring during the compression and recompression of solids.* J Pharm Pharmacol, 1970: p. Suppl:11S+.
7. Wurster, D.E. and J.R. Creekmore, *MEASUREMENT OF THE THERMAL-ENERGY EVOLVED UPON TABLET COMPRESSION.* Drug Development and Industrial Pharmacy, 1986. **12**(10): p. 1511-1528.
8. Wurster, D.E., C.E. Rowlings, and J.R. Creekmore, *CALORIMETRIC ANALYSIS OF POWDER COMPRESSION .1. DESIGN AND DEVELOPMENT OF A COMPRESSION CALORIMETER.* International Journal of Pharmaceutics, 1995. **116**(2): p. 179-189.
9. Rowlings, C.E., D.E. Wurster, and P.J. Ramsey, *CALORIMETRIC ANALYSIS OF POWDER COMPRESSION .2. THE RELATIONSHIP BETWEEN ENERGY TERMS MEASURED WITH A COMPRESSION CALORIMETER AND TABLETING BEHAVIOR.* International Journal of Pharmaceutics, 1995. **116**(2): p. 191-200.
10. Bechard, S.R. and G.R. Down, *Infrared imaging of pharmaceutical materials undergoing compaction.* Pharm Res, 1992. **9**(4): p. 521-8.
11. Ketolainen, J., J. Ilkka, and P. Paronen, *TEMPERATURE-CHANGES DURING TABLETTING MEASURED USING INFRARED THERMOVIEWER.* International Journal of Pharmaceutics, 1993. **92**(1-3): p. 157-166.
12. Krok, A., et al., *An experimental investigation of temperature rise during compaction of pharmaceutical powders.* International Journal of Pharmaceutics, 2016. **513**(1-2): p. 97-108.
13. Klinzing, G.R., et al., *Temperature and density evolution during compaction of a capsule shaped tablet.* Computers & Chemical Engineering, 2010. **34**(7): p. 1082-1091.
14. Krok, A., et al., *Finite element analysis of thermomechanical behaviour of powders during tabletting.* Chemical Engineering Research & Design, 2016. **110**: p. 141-151.

15. Roueche, E., et al., *Influence of temperature on the compaction of an organic powder and the mechanical strength of tablets.* Powder Technology, 2006. **162**(2): p. 138-144.
16. Cespi, M., et al., *Effect of temperature increase during the tableting of pharmaceutical materials.* International Journal of Pharmaceutics, 2013. **448**(1): p. 320-326.
17. Pingali, K.C. and R. Mendez, *Nanosmearing due to process shear - Influence on powder and tablet properties.* Advanced Powder Technology, 2014. **25**(3): p. 952-959.
18. Pingali, K.C. and R. Mendez, *Physicochemical behavior of pharmaceutical particles and distribution of additives in tablets due to process shear and lubricant composition.* Powder Technology, 2014. **268**: p. 1-8.
19. Zhang, G.G.Z., et al., *Phase transformation considerations during process development and manufacture of solid oral dosage forms.* Advanced Drug Delivery Reviews, 2004. **56**(3): p. 371-390.
20. Usamentiaga, R., et al., *Infrared Thermography for Temperature Measurement and Non-Destructive Testing.* Sensors, 2014. **14**(7): p. 12305-12348.
21. Bauer, J., et al., *Non-contact thermal imaging as potential tool for personalized diagnosis and prevention of cellulite.* Journal of Thermal Analysis and Calorimetry, 2018. **133**(1): p. 571-578.
22. De Salis, A.F., R. Saatchi, and P. Dimitri, *Evaluation of high resolution thermal imaging to determine the effect of vertebral fractures on associated skin surface temperature in children with osteogenesis imperfecta.* Medical & Biological Engineering & Computing, 2018. **56**(9): p. 1633-1643.
23. Gatt, A., et al., *The identification of higher forefoot temperatures associated with peripheral arterial disease in type 2 diabetes mellitus as detected by thermography.* Primary Care Diabetes, 2018. **12**(4): p. 312-318.
24. Holm, J.K., et al., *Prognostic value of infrared thermography in an emergency department.* European Journal of Emergency Medicine, 2018. **25**(3): p. 204-208.
25. Lakshmi, P.S., K.M. Shashi, and E.T. Joy, *A REVIEW ON THERMOGRAPHY IN DENTISTRY.* Journal of Evolution of Medical and Dental Sciences-Jemds, 2018. **7**(10): p. 1290-1293.
26. Kacmaz, S., et al., *The use of infrared thermal imaging in the diagnosis of deep vein thrombosis.* Infrared Physics & Technology, 2017. **86**: p. 120-129.
27. Fernandez-Cuevas, I., et al., *Infrared Thermography for the Detection of Injury in Sports Medicine*, in *Application of Infrared Thermography in Sports Science*, J.I.P. Quesada, Editor. 2017. p. 81-109.
28. Jones, B.F., *A reappraisal of the use of infrared thermal image analysis in medicine.* Ieee Transactions on Medical Imaging, 1998. **17**(6): p. 1019-1027.
29. Fukahori, F.L.P., et al., *Method for auxiliary use of thermography in diagnosing inflammation in the coxofemoral joint in dogs.* Semina-Ciencias Agrarias, 2018. **39**(4): p. 1565-1574.
30. Soroko, M. and K. Howell, *Infrared Thermography: Current Applications in Equine Medicine.* Journal of Equine Veterinary Science, 2018. **60**: p. 90-+.

31. Soroko, M., et al., *Application of thermography in racehorse performance*, in *13th Quantitative Infrared Thermography Conference*. 2016. p. 765-769.
32. Rekant, S.I., et al., *Veterinary applications of infrared thermography.* American Journal of Veterinary Research, 2016. **77**(1): p. 98-107.
33. Redaelli, V., et al., *Potential application of thermography (IRT) in animal production and for animal welfare. A case report of working dogs.* Annali Dell Istituto Superiore Di Sanita, 2014. **50**(2): p. 147-152.
34. Kunc, P. and I. Knizkova, *The Use of Infrared Thermography in Livestock Production and Veterinary Field*. Infrared Thermography: Recent Advances and Future Trends, ed. C. Meola. 2012. 85-101.
35. Lozano III, A.H., F., *Infrared imaging for breast cancer detection: An objective review of foundational studies and its proper role in breast cancer screening,.* Infrared Physics & Technology,, 2019. **97**: p. 244-257.
36. Kennedy, D.A., T. Lee, and D. Seely, *A Comparative Review of Thermography as a Breast Cancer Screening Technique.* Integrative Cancer Therapies, 2009. **8**(1): p. 9-16.
37. Gonzalez-Hernandez, J.L., et al., *Technology, application and potential of dynamic breast thermography for the detection of breast cancer.* International Journal of Heat and Mass Transfer, 2019. **131**: p. 558-573.
38. Sarigoz, T., et al., *Role of digital infrared thermal imaging in the diagnosis of breast mass: A pilot study Diagnosis of breast mass by thermography.* Infrared Physics & Technology, 2018. **91**: p. 214-219.
39. Kontos, M., R. Wilson, and I. Fentiman, *Digital infrared thermal imaging (DITI) of breast lesions: sensitivity and specificity of detection of primary breast cancers.* Clinical Radiology, 2011. **66**(6): p. 536-539.
40. Arora, N., et al., *Effectiveness of a noninvasive digital infrared thermal imaging system in the detection of breast cancer.* American Journal of Surgery, 2008. **196**(4): p. 523-526.
41. Ng, E.Y.K., *A review of thermography as promising non-invasive detection modality for breast tumor.* International Journal of Thermal Sciences, 2009. **48**(5): p. 849-859.
42. Manginas, A., et al., *Right Ventricular Endocardial Thermography in Transplanted and Coronary Artery Disease Patients: First Human Application.* Journal of Invasive Cardiology, 2010. **22**(9): p. 400-404.
43. Nguyen, A.V., et al., *Comparison of 3 Infrared Thermal Detection Systems and Self-Report for Mass Fever Screening.* Emerging Infectious Diseases, 2010. **16**(11): p. 1710-1717.
44. Vargas, J.V.C., et al., *Normalized methodology for medical infrared imaging.* Infrared Physics & Technology, 2009. **52**(1): p. 42-47.
45. Fikackova, H. and E. Ekberg, *Can infrared thermography be a diagnostic tool for arthralgia of the temporomandibular joint?* Oral Surgery Oral Medicine Oral Pathology Oral Radiology and Endodontics, 2004. **98**(6): p. 643-650.
46. Bagavathiappan, S., et al., *Infrared thermography for condition monitoring - A review.* Infrared Physics & Technology, 2013. **60**: p. 35-55.

47. Jaffery, Z.A. and A.K. Dubey, *Design of early fault detection technique for electrical assets using infrared thermograms.* International Journal of Electrical Power & Energy Systems, 2014. **63**: p. 753-759.
48. Buerhop, C., et al., *Verifying defective PV-modules by IR-imaging and controlling with module optimizers.* Progress in Photovoltaics, 2018. **26**(8): p. 622-630.
49. La Rosa, G. and A. Risitano, *Thermographic methodology for rapid determination of the fatigue limit of materials and mechanical components.* International Journal of Fatigue, 2000. **22**(1): p. 65-73.
50. Luong, M.P., *Fatigue limit evaluation of metals using an infrared thermographic technique.* Mechanics of Materials, 1998. **28**(1-4): p. 155-163.
51. Lerma, C., et al., *Quantitative Analysis Procedure for Building Materials in Historic Buildings by Applying Infrared Thermography.* Russian Journal of Nondestructive Testing, 2018. **54**(8): p. 601-609.
52. Albatici, R., A.M. Tonelli, and M. Chiogna, *A comprehensive experimental approach for the validation of quantitative infrared thermography in the evaluation of building thermal transmittance.* Applied Energy, 2015. **141**: p. 218-228.
53. Grinzato, E., V. Vavilov, and T. Kauppinen, *Quantitative infrared thermography in buildings.* Energy and Buildings, 1998. **29**(1): p. 1-9.
54. Entrop, A.G. and A. Vasenev, *Infrared drones in the construction industry: designing a protocol for building thermography procedures*, in *11th Nordic Symposium on Building Physics*, S. Geving and B. Time, Editors. 2017, Elsevier Science Bv: Amsterdam. p. 63-68.
55. Fokaides, P.A. and S.A. Kalogirou, *Application of infrared thermography for the determination of the overall heat transfer coefficient (U-Value) in building envelopes.* Applied Energy, 2011. **88**(12): p. 4358-4365.
56. Ohlsson, K.E.A. and T. Olofsson, *Quantitative infrared thermography imaging of the density of heat flow rate through a building element surface.* Applied Energy, 2014. **134**: p. 499-505.
57. Lucchi, E., *Applications of the infrared thermography in the energy audit of buildings: A review.* Renewable & Sustainable Energy Reviews, 2018. **82**: p. 3077-3090.
58. Dua, G. and R. Mulaveesala, *Thermal wave imaging for non-destructive testing and evaluation of reinforced concrete structures.* Insight, 2018. **60**(5): p. 252-256.
59. Pastor, M.L., et al., *Applying infrared thermography to study the heating of 2024-T3 aluminium specimens under fatigue loading.* Infrared Physics & Technology, 2008. **51**(6): p. 505-515.
60. Badulescu, C., et al., *Applying the grid method and infrared thermography to investigate plastic deformation in aluminium multicrystal.* Mechanics of Materials, 2011. **43**(1): p. 36-53.
61. Kylili, A., et al., *Infrared thermography (IRT) applications for building diagnostics: A review.* Applied Energy, 2014. **134**: p. 531-549.

62. Youcef, M., et al., *A non destructive method for diagnostic of insulated building walls using infrared thermography*, in *Thermosense Xxix*, K.M. Knettel, V.P. Vavilov, and J.J. Miles, Editors. 2007.
63. Balaras, C.A. and A.A. Argiriou, *Infrared thermography for building diagnostics.* Energy and Buildings, 2002. **34**(2): p. 171-183.
64. O'Grady, M., A.A. Lechowska, and A.M. Harte, *Application of infrared thermography technique to the thermal assessment of multiple thermal bridges and windows.* Energy and Buildings, 2018. **168**: p. 347-362.
65. Grinzato, E., P.G. Bison, and S. Marinetti, *Monitoring of ancient buildings by the thermal method.* Journal of Cultural Heritage, 2002. **3**(1): p. 21-29.
66. Chulkov, A.O., et al., *Quantitative evaluation of water content in composite honeycomb structures by using one-sided IR thermography: is there any promise?*, in *Thermosense: Thermal Infrared Applications Xxxix*, P. Bison and D. Burleigh, Editors. 2017.
67. Vavilov, V., et al., *Detecting water ingress in aviation honeycomb panels: Qualitative and quantitative aspects.* Polymer Testing, 2016. **54**: p. 270-280.
68. Vavilov, V. and D. Nesteruk, *Evaluating water content in aviation honeycomb panels by transient IR thermography*, in *Thermosense XXVII*, G.R. Peacock, D.D. Burleigh, and J.J. Miles, Editors. 2005. p. 411-417.
69. Vavilov, V., et al., *Detecting water in aviation honeycomb structures by using transient IR thermographic NDT*, in *Thermosense Xxv*, K.E. Cramer and X.P. Maldague, Editors. 2003. p. 345-355.
70. Garcia-Tejero, I.F., et al., *Infrared thermography to select commercial varieties of maize in relation to drought adaptation.* Quantitative Infrared Thermography Journal, 2017. **14**(1): p. 54-67.
71. Kovar, M. and I. Cerny, *EVALUATION OF WATER REGIME IN SUGAR BEET PLANTS BY INFRARED THERMOGRAPHY.* Listy Cukrovarnicke a Reparske, 2016. **132**(2): p. 54-59.
72. Fan, J.X. and J.X. Huang, *Some Design Considerations for High-Performance Infrared Imaging Seeker*, in *Electro-Optical and Infrared Systems: Technology and Applications Xii; and Quantum Information Science and Technology*, D.A. Huckridge, et al., Editors. 2015, Spie-Int Soc Optical Engineering: Bellingham.
73. Maini, A.K. and V. Agrawal, *Test system for comprehensive evaluation of infrared-guided missiles.* Iet Optoelectronics, 2012. **6**(5): p. 255-262.
74. Kalirai, J., *Scientific discovery with the James Webb Space Telescope.* Contemporary Physics, 2018. **59**(3): p. 251-290.
75. Wiecek, B. and Ieee, *Review on thermal image processing for passive and active thermography*, in *2005 27th Annual International Conference of the IEEE Engineering in Medicine and Biology Society, Vols 1-7*. 2005. p. 686-689.
76. Doshvarpassand, S., C.Z. Wu, and X.Y. Wang, *An overview of corrosion defect characterization using active infrared thermography.* Infrared Physics & Technology, 2019. **96**: p. 366-389.
77. Hung, Y.Y., et al., *Review and comparison of shearography and active thermography for nondestructive evaluation.* Materials Science & Engineering R-Reports, 2009. **64**(5-6): p. 73-112.

78. Rogalski, A., *Progress in focal plane array technologies.* Progress in Quantum Electronics, 2012. **36**(2-3): p. 342-473.
79. Modest, M.F., *Radiative Heat Transfer.* Elsevier Inc.,, 2013.
80. Gade, R. and T.B. Moeslund, *Thermal cameras and applications: a survey.* Machine Vision and Applications, 2014. **25**(1): p. 245-262.
81. Omar, C.S., et al., *Roller compaction: Effect of morphology and amorphous content of lactose powder on product quality.* International Journal of Pharmaceutics, 2015. **496**(1): p. 63-74.
82. Emteborg, H., et al., *Infrared Thermography for Monitoring of Freeze-Drying Processes: Instrumental Developments and Preliminary Results.* Journal of Pharmaceutical Sciences, 2014. **103**(7): p. 2088-2097.
83. Goncalves, B.J., et al., *Infrared (IR) thermography applied in the freeze-drying of gelatin model solutions added with ethanol and carrier agents.* Journal of Food Engineering, 2018. **221**: p. 77-87.
84. Wiedey, R. and P. Kleinebudde, *Infrared thermography - A new approach for in-line density measurement of ribbons produced from roll compaction.* Powder Technology, 2018. **337**: p. 17-24.
85. Wiedey, R. and P. Kleinebudde, *Potentials and limitations of thermography as an in-line tool for determining ribbon solid fraction.* Powder Technology, 2019. **341**: p. 2-10.
86. Llusa, M., et al., *Measuring the hydrophobicity of lubricated blends of pharmaceutical excipients.* Powder Technology, 2010. **198**(1): p. 101-107.
87. Llusa, M., Muzzio, F, *The Effect of Shear Mixing on the Blending of Cohesive Lubricants and Drugs.* Pharmaceutical Technology, 2005(7).
88. Wang, Y., *USING MULTIVARIATE ANALYSIS FOR PHARMACEUTICAL DRUG PRODUCT DEVELOPMENT.* Rutgers University, PhD Thesis, 2016.
89. Hernandez, E., et al., *Prediction of dissolution profiles by non-destructive near infrared spectroscopy in tablets subjected to different levels of strain.* Journal of Pharmaceutical and Biomedical Analysis, 2016. **117**: p. 568-576.
90. Mullarney, M.P., et al., *Applying dry powder coatings to pharmaceutical powders using a comil for improving powder flow and bulk density.* Powder Technology, 2011. **212**(3): p. 397-402.
91. Razavi, S.M., et al., *Toward predicting tensile strength of pharmaceutical tablets by ultrasound measurement in continuous manufacturing.* International Journal of Pharmaceutics, 2016. **507**(1-2): p. 83-89.
92. Mehrotra, A., et al., *Influence of shear intensity and total shear on properties of blends and tablets of lactose and cellulose lubricated with magnesium stearate.* International Journal of Pharmaceutics, 2007. **336**(2): p. 284-291.
93. Pingali, K.C. and R. Mendez, *Assessing distribution of nanosmears due to mutual interaction of additives in high shear mixing of pharmaceutical blends.* Chemical Engineering and Processing, 2014. **85**: p. 248-255.
94. Alam, M.A., et al., *In-line monitoring and optimization of powder flow in a simulated continuous process using transmission near infrared spectroscopy.* International Journal of Pharmaceutics, 2017. **526**(1-2): p. 199-208.

95. Igne, B., et al., *Near-Infrared Spatially Resolved Spectroscopy for Tablet Quality Determination.* Journal of Pharmaceutical Sciences, 2015. **104**(12): p. 4074-4081.
96. Peeters, E., et al., *Assessment and prediction of tablet properties using transmission and backscattering Raman spectroscopy and transmission NIR spectroscopy.* Asian Journal of Pharmaceutical Sciences, 2016. **11**(4): p. 547-558.
97. Corredor, C.C., et al., *Development and Robustness Verification of an At-Line Transmission Raman Method for Pharmaceutical Tablets Using Quality by Design (QbD) Principles.* Journal of Pharmaceutical Innovation, 2018. **13**(4): p. 287-300.
98. Nagy, B., et al., *Raman Spectroscopy for Process Analytical Technologies of Pharmaceutical Secondary Manufacturing.* Aaps Pharmscitech, 2019. **20**(1): p. 16.
99. Dohi, M., et al., *Application of terahertz pulse imaging as PAT tool for non-destructive evaluation of film-coated tablets under different manufacturing conditions.* Journal of Pharmaceutical and Biomedical Analysis, 2016. **119**: p. 104-113.
100. May, R.K., et al., *Hardness and density distributions of pharmaceutical tablets measured by terahertz pulsed imaging.* Journal of Pharmaceutical Sciences, 2013. **102**(7): p. 2179-2186.
101. Akseli, I., et al., *A Quantitative Correlation of the Effect of Density Distributions in Roller-Compacted Ribbons on the Mechanical Properties of Tablets Using Ultrasonics and X-ray Tomography.* Aaps Pharmscitech, 2011. **12**(3): p. 834-853.
102. Akseli, I., D.C. Becker, and C. Cetinkaya, *Ultrasonic determination of Young's moduli of the coat and core materials of a drug tablet.* International Journal of Pharmaceutics, 2009. **370**(1-2): p. 17-25.
103. Sokolovskii, R.I. and M.V. Shablygin, *Application of the Quasi-Regular Cooling Regime Method to Experimental Determination of the Thermophysical Parameters of Textile Materials.* Fibre Chemistry, 2015. **47**(2): p. 108-116.
104. Luikov, A.V., *Analytical heat transfer theory*. 1968: Academic Press.
105. Isachenko, V.P., V.A. Osipova, and A.S. Sukomel, Heat Transfer, Chapter 3.9 Regular Cooling (Heating) of Bodies, Mir Publisher, 1980: p. 131-139.
106. Fell, J.T. and J.M. Newton, *Determination of tablet strength by the diametral-compression test.* J Pharm Sci, 1970. **59**(5): p. 688-91.
107. Pawar, P., et al., *The effect of mechanical strain on properties of lubricated tablets compacted at different pressures.* Powder Technology, 2016. **301**: p. 657-664.
108. Kuentz, M. and H. Leuenberger, *A new theoretical approach to tablet strength of a binary mixture consisting of a well and a poorly compactable substance.* Eur J Pharm Biopharm, 2000. **49**(2): p. 151-9.
109. Ryshkewitch, E., *Compression strength of porous sintered alumia and zirconia.* Journal of the American Ceramic Society, 1953. **36**.
110. Tye, C.K., C.C. Sun, and G.E. Amidon, *Evaluation of the effects of tableting speed on the relationships between compaction pressure, tablet tensile strength, and*

tablet solid fraction. Journal of Pharmaceutical Sciences, 2005. **94**(3): p. 465-472.
111. Razavi, S.M., M. Gonzalez, and A.M. Cuitino, *General and mechanistic optimal relationships for tensile strength of doubly convex tablets under diametrical compression.* International Journal of Pharmaceutics, 2015. **484**(1-2): p. 29-37.
112. MTALAB (2016) (R2016b). The Math Works Inc., N., Massachusetts.
113. Lee, H.P., Y. Gulak, and A.M. Cuitino, *Transient Temperature Monitoring of Pharmaceutical Tablets During Compaction Using Infrared Thermography.* Aaps Pharmscitech, 2018. **19**(5): p. 2426-2433.
114. Krok, A., et al., *Thermal properties of compacted pharmaceutical excipients.* International Journal of Pharmaceutics, 2017. **534**(1-2): p. 119-127.
115. Kucuk, G., M. Gonzalez, and A.M. Cuitino, *2D PARTICLE MECHANICS SIMULATIONS ON EVOLUTION AND INTERACTIONS OF HEAT CHAINS AND FORCE NETWORKS UNDER STEADY-STATE CONDITIONS.* Computational Thermal Sciences, 2015. **7**(5-6): p. 515-526.
116. Yohannes, B., et al., *Evolution of the microstructure during the process of consolidation and bonding in soft granular solids.* International Journal of Pharmaceutics, 2016. **503**(1-2): p. 68-77.
117. Garner, S., J. Strong, and A. Zavaliangos, *Study of the die compaction of powders to high relative densities using the discrete element method.* Powder Technology, 2018. **330**: p. 357-370.
118. Vargas, W.L. and J.J. McCarthy, *Heat conduction in granular materials.* Aiche Journal, 2001. **47**(5): p. 1052-1059.
119. Vargas, W.L. and J.J. McCarthy, *Thermal expansion effects and heat conduction in granular materials.* Physical Review E, 2007. **76**(4).
120. Cundall, P.A.S., O, *A discrete numerical model for granular assemblies.* Geotechnique, 1979. **29(1)**: p. 47–65.
121. Johnson, K.L., *Contact mechanics.* Cambridge university press, 1987.
122. Mindlin, R.D., *Compliance of Elastic Bodies in Contact.* J. Appl. Mech., 1994. **16**: p. 333.
123. Thornton, C., and Randall, C.W., *Applications of Theoretical Contact Mechanics to Solid Particle System Simulation* Micromechanics of Granular Material, M. Satake and J.T. Jenkins, eds., Elsevier, Amsterdam, 1988: p. 133.
124. Sridhar, M.R. and M.M. Yovanovich, *REVIEW OF ELASTIC AND PLASTIC CONTACT CONDUCTANCE MODELS - COMPARISON WITH EXPERIMENT.* Journal of Thermophysics and Heat Transfer, 1994. **8**(4): p. 633-640.
125. Lambert, M.A. and L.S. Fletcher, *Review of models for thermal contact conductance of metals.* Journal of Thermophysics and Heat Transfer, 1997. **11**(2): p. 129-140.
126. Fletcher, L.S., *RECENT DEVELOPMENTS IN CONTACT CONDUCTANCE HEAT-TRANSFER.* Journal of Heat Transfer-Transactions of the Asme, 1988. **110**(4B): p. 1059-1070.
127. Landau, L.a.L., EM *Theory of Elasticity.* Pergamon Press, 1959.

128. Batchelor, G.O.B., RW, *Thermal or electrical conduction through a granular material.* Proceedings of the Royal Society of London. A. Mathematical and Physical Sciences, 1977. **355(1682)**: p. 313–333.
129. Yohannes, B., et al., *The role of fine particles on compaction and tensile strength of pharmaceutical powders.* Powder Technology, 2015. **274**: p. 372-378.
130. Koynov, A., I. Akseli, and A.M. Cuitino, *Modeling and simulation of compact strength due to particle bonding using a hybrid discrete-continuum approach.* International Journal of Pharmaceutics, 2011. **418**(2): p. 273-285.
131. Bratberg, I., F. Radjai, and A. Hansen, *Dynamic rearrangements and packing regimes in randomly deposited two-dimensional granular beds.* Physical Review E, 2002. **66**(3).
132. Mueller, G.E., *Numerical simulation of packed beds with monosized spheres in cylindrical containers.* Powder Technology, 1997. **92**(2): p. 179-183.